
Electronic Thesis and Dissertation Repository

4-18-2022 10:15 AM

A Novel Ultrasound Elastography Technique for Evaluating Tumor Response to Neoadjuvant Chemotherapy in Patients with Locally Advanced Breast Cancer

Niusha Kheirkhah, *The University of Western Ontario*

Supervisor: Samani, Abbas, *The University of Western Ontario*

Joint Supervisor: Sadeghi-Naini, Ali, *York University, Toronto, ON, Canada*

A thesis submitted in partial fulfillment of the requirements for the Doctor of Philosophy degree in Biomedical Engineering

© Niusha Kheirkhah 2022

Follow this and additional works at: <https://ir.lib.uwo.ca/etd>

 Part of the Biomechanics and Biotransport Commons

Recommended Citation

Kheirkhah, Niusha, "A Novel Ultrasound Elastography Technique for Evaluating Tumor Response to Neoadjuvant Chemotherapy in Patients with Locally Advanced Breast Cancer" (2022). *Electronic Thesis and Dissertation Repository*. 8541.

<https://ir.lib.uwo.ca/etd/8541>

This Dissertation/Thesis is brought to you for free and open access by Scholarship@Western. It has been accepted for inclusion in Electronic Thesis and Dissertation Repository by an authorized administrator of Scholarship@Western. For more information, please contact wlsadmin@uwo.ca.

Abstract

Breast cancer is the second most diagnosed cancer in women, estimated to affect 1 in 8 women during their lifetime. About 10% to 20% of new breast cancer cases are diagnosed with locally advanced breast cancer (LABC). LABC tumors are usually larger than 5 cm and/or attached to the skin or chest wall. It has been reported that when such cases are treated with surgery alone, metastasis and mortality rates are high, especially where skin involvement or attachment to the chest wall is extensive. As such, efficient treatment for this kind of breast cancer includes neoadjuvant chemotherapy (NAC) to shrink the tumor and detach it from the chest wall followed by surgery. Several studies have shown that there is a strong correlation between response to NAC and improved treatment outcomes, including survival rate. Unfortunately, 30% to 40% of patients do not respond to chemotherapy, hence losing critical treatment time and resources. Predicting a patient's response at the early stages of treatment can help physicians make informed decisions about whether to continue the treatment or use an alternative treatment if a poor response is predicted. Such early and accurate response prediction can shorten the wasted time and reduce resources dedicated to patients while they endure significant side effects. Therefore, it is important to identify this group of non-responder patients as early as possible so that they can be prescribed alternative treatments. Current methods for evaluating LABC response to NAC are based on changes in tumor dimensions using physical examinations or standard anatomical imaging. Such changes may take several months to be detectable. Studies have shown that there is a correlation between LABC response to NAC and tumor softening. In other words, in contrast to responder patients where tumor stiffness generally decreases in response to NAC, in non-responder patients the stiffness of the tumor increases or does not change significantly. As such, a reliable and widely available breast elastography technique can have a major impact on the effective treatment of LABC patients. In this study, we first develop a tissue-mechanics-based method for improving the accuracy of ultrasound elastography. This method consists of 3 steps that are applied to the displacement fields generated from conventional motion-tracking methods. These three steps include: smoothing the displacement fields using Laplacian filtering, enforcing tissue incompressibility equation to refine the displacement fields, and finally enforcing tissue compatibility equation to refine the strain fields. The method was promising through validation using *in silico*,

phantom, and *in vivo* studies. A huge improvement of this method compared to other motion-tracking methods is its ability in generating lateral displacement with high accuracy. This becomes especially important when the displacement and strain fields are used as inputs to an inverse-problem framework for calculating the stiffness characteristics of tissue, for example, Young's modulus. We then use this enhanced ultrasound elastography technique to assess the response of LABC patients to NAC based on monitoring the stiffness of their tumors throughout the chemotherapy course. Our results show that this method is effective in predicting patients' responses accurately as early as 1 week after NAC initiation.

Keywords

Biomechanics, Breast Cancer, Chemotherapy, Diagnosis, Early Detection, Elastography, Finite Element Modeling, Full Inversion, Iterative Method, Locally Advanced Breast Cancer, Motion-tracking Method, Neoadjuvant Chemotherapy, Optimization, Regularization, Tumor Response Evaluation, Ultrasound Imaging, Ultrasound Elastography

Summary for Lay Audience

Breast cancer is the most diagnosed type of cancer and the second leading cause of cancer-related deaths in women. In 2020, it was estimated that more than 27,000 new invasive breast cancer cases to be diagnosed in women while 5100 women were predicted to die from this disease in Canada. Breast cancer tumor development is associated with considerable interaction with stromal cells, extracellular matrix, and connective tissue. As such, breast cancer is associated with significant changes in tissue biomechanical properties.

Out of patients struck with breast cancer, 10% to 20% are diagnosed with locally advanced breast cancer (LABC). Current treatments for LABC include neoadjuvant chemotherapy (NAC), followed by mastectomy or lumpectomy. The NAC is administrated to shrink the tumor and detach it from the chest wall so that it becomes operable. While the response to chemotherapy has demonstrated a strong correlation with overall treatment outcomes and patients' survival, unfortunately, 30% to 40% of patients do not respond to chemotherapy. Therefore, it is important to identify this group of non-responder patients as early as possible so that they can be prescribed alternative treatments. The current methods for evaluating LABC response to NAC is based on changes in tumor dimensions using physical examinations or standard anatomical imaging. However, changes in tumor size after NAC may take several months to be detectable, and in some cases, they do not become apparent despite a positive histological outcome. Studies have shown that, generally, there is a correlation between LABC response to NAC and tumor softening. In other words, in contrast to responder patients where tumor stiffness generally decreases in response to NAC, in non-responder patients the stiffness of tumor increases or does not change significantly.

Ultrasound (US) Elastography is a non-invasive imaging modality developed for tissue stiffness mapping. This imaging modality can potentially be used as a clinically viable diagnostic tool to detect and characterize mechanical properties of breast cancer tumors including stiffness changes over time. The primary purpose of our long-term study is to develop novel methods for US elastography to improve its accuracy and reliability in the clinical setting. Once developed, we applied the methods using clinical data acquired through an observational study on LABC patients who underwent NAC. Results obtained from this study are used to assess the efficacy of our enhanced US elastography technique in evaluating

LABC patient response soon after the start of NAC. According to these results, our method is successful in assessing this response as soon as 1 week after the start of NAC.

Co-Authorship Statement

This thesis has been written by Niusha Kheirkhah under the supervision of Dr. Abbas Samani and Dr. Ali Sadeghi-Naini. Parts of the material presented in this thesis have been submitted for publication in peer-reviewed journals as listed below. The research presented in each publication has been conceived, designed, and overseen by the Ph.D. supervisors, performed by the principal author and supported by or in collaboration with the other authors who are the research collaborators, members of the advisory committee, or members of the collaborative research team.

The material presented in Chapter 2 has been presented in a submitted journal paper as follows:
N. Kheirkhah, S. Dempsey, A. Sadeghi-Naini, A. Samani, “A Novel Tissue Mechanics-based Method for Improved Ultrasound Motion Tracking in Ultrasound Elastography”, Under Revision, Medical Physics, 2022.

The material presented in Chapter 3 has been presented in a submitted journal paper as follows:
N. Kheirkhah, A. Kornecki, G. J. Czarnota, A. Samani, A. Sadeghi-Naini, “Enhanced Full-Inversion-Based Ultrasound Elastography for Evaluating Tumor Response to Neoadjuvant Chemotherapy in Patients with Locally Advanced Breast Cancer”, Under Review, Physica Medica, 2022.

Dedication

*I dedicate this thesis to my loving parents and brother
for their endless love, support, and encouragement. I hope
this achievement will fulfill the dream they envisioned for me.*

Acknowledgments

A debt of gratitude is owed to my supervisors Dr. Abbas Samani and Dr. Ali Sadeghi-Naini. The completion of this study could not have been possible without their support and expertise.

I would also like to thank Dr. Anat Kornecki, Dr. Aaron Fenster, and Dr. Jeffrey Carson for their support throughout this research.

The funding of this work was provided by the Western University, Natural Sciences and Engineering Research Council of Canada (NSERC), and the Terry Fox Foundation.

Table of Contents

Abstract	ii
Summary for Lay Audience.....	iv
Co-Authorship Statement.....	vi
Dedication	vii
Acknowledgments.....	viii
Table of Contents	ix
List of Tables	xii
List of Figures	xiii
List of Acronyms and Abbreviations.....	xv
Chapter 1	1
1 Introduction	1
1.1 Background and Motivation	1
1.1.1 Breast Cancer	1
1.1.2 Breast Cancer Screening, Detection, and Diagnosis.....	3
1.1.3 Breast Cancer Treatment.....	7
1.2 Theory	8
1.2.1 Elastography	9
1.2.2 Mechanics Principles	14
1.3 Literature Review.....	16
1.3.1 Dynamic Contrast Enhanced (DCE) MRI	16
1.3.2 Positron Emission Tomography (PET).....	18
1.3.3 Quantitative Ultrasound (QUS)	19
1.3.4 Breast Ultrasound Elastography	20
1.4 Objectives	21

1.5 Thesis Outline	22
1.5.1 Chapter 2	22
1.5.2 Chapter 3	22
1.5.3 Chapter 4	23
References	23
Chapter 2	35
2 A Novel Tissue Mechanics-based Method for Improving Tissue Displacement and Strain Estimation in Breast Ultrasound Elastography	35
2.1 Introduction	35
2.2 Materials and Methods	39
2.2.1 Overview of Strain Refinement Algorithm (STREAL)	39
2.2.2 Method Validation	46
2.3 Results	50
2.3.1 <i>In silico</i> Breast Phantom Study	50
2.3.2 Tissue Mimicking Breast Phantom Study	53
2.3.3 Clinical Breast Ultrasound Elastography Case	57
2.4 Discussion	60
References	62
Chapter 3	69
3 Enhanced Full-Inversion-Based Ultrasound Elastography for Evaluating Tumor Response to Neoadjuvant Chemotherapy in Patients with Locally Advanced Breast Cancer	69
3.1 Introduction	69
3.2 Materials and Methods	72
3.2.1 Study Protocol and Data Acquisition	72
3.2.2 Enhanced Strain Imaging	75
3.2.3 Full Inversion-Based Elastic Modulus Reconstruction	75

3.2.4	Data Analysis	77
3.3	Results.....	78
3.4	Discussion and Conclusion	85
	References	87
Chapter 4		95
4	Conclusions and Future Work.....	95
4.1	Conclusions.....	95
4.1.1	Chapter 2: A Novel Tissue Mechanics-based Method for Improving Tissue Displacement and Strain Estimation in Breast Ultrasound Elastography.	95
4.1.2	Chapter 3: Enhanced Full-Inversion-Based Ultrasound Elastography for Evaluating Tumor Response to Neoadjuvant Chemotherapy in Patients with Locally Advanced Breast Cancer	96
4.2	Future Directions	97
4.3	Closing Remarks	98
Curriculum Vitae		100

List of Tables

Table 1-1: BI-RADS categories description [17], [18].....	4
Table 2-1: Different weight sets used for enforcing tissue incompressibility	45
Table 2-2: NMI values of displacement and strain fields generated using the algorithm steps with corresponding “true” fields in the <i>in silico</i> phantom study	53
Table 2-3: Similarity between displacement and strain fields generated by the <i>in silico</i> simulation and counterpart fields computed by the GLUE, SOUL, and STREAL methods..	55
Table 2-4: Calculated SNR and CNR metrics for axial and lateral strain images of the 4 phantoms	59
Table 3-1: Participating patients’ characteristics	74
Table 3-2: Results of statistical analysis obtained for different elastography parameters acquired from the responding and non-responding patient cohorts at different times after the NAC initiation. *, †, and ‡ demonstrate statistically significant (p-value < 0.05), highly significant, (p-value < 0.01), and extremely significant (p-value < 0.001), respectively.....	84

List of Figures

Figure 1-1. A schematic of a semi-infinite medium under a point load	15
Figure 2-1. Strain Refinement Algorithm (STREAL) flowchart.....	39
Figure 2-2. The L-curve plot and its knee point which corresponds to an optimal λ value.	41
Figure 2-3: Boussinesq's model - a schematic of a semi-infinite medium under a point load	43
Figure 2-4: (a) Part of the breast surface under a rectangular contact pressure of the US probe and image's rectangular FOV where at each point of this FOV, the stress values are calculated by integration of Equations (2-7), (2-8) and (2-9) over the probe's contact surface. (b) Part of the breast FE model cut at the spherical tumor region with a rigid US probe pushing against the breast. The rectangular surface mimics the US FOV. As shown in the figure, x, y, and z directions are corresponding to lateral, out-of-plane, and axial, respectively.	48
Figure 2-5: Original displacement fields generated from the <i>in silico</i> breast model, their noisy counterparts, and refined displacement fields after steps 1 and 2 of STREAL	51
Figure 2-6: Incompressibility equation calculated using the simulated displacement data based on (a) plane strain assumption and (b) semi-infinite medium model. The latter is closer to uniformly black image (zero field) that represents an ideal incompressible tissue.	52
Figure 2-7: Evaluation of the weight sets used for enforcing tissue incompressibility in the <i>in silico</i> phantom study; c) the NMI similarity measure between true and refined displacements, d) percentage of compatible FE elements.	52
Figure 2-8: True and refined strain fields at different stages of applying STREAL	53
Figure 2-9: Axial (I) and lateral (II) displacement fields obtained from GLUE, SOUL, and the proposed STREAL methods for phantom cases A-D. Note that these results were obtained after performing the first two steps of the STREAL algorithm since the third step only applies to strain fields.	56

Figure 2-10: Axial (I) and lateral (II) strain images obtained from GLUE, SOUL, and the proposed STREAL method for phantom cases A-D. Note that the figures show the real values of axial and lateral strains, and the positive values represent compression. Due to inconsistency between the lateral strain values of different methods, different color bars are adjusted for each method to have the best visualization.....	57
Figure 2-11: B-mode images of clinical case where the red outline shows the tumor area..	58
Figure 2-12: Axial and lateral strain images of the clinical case generated using GLUE, SOUL, and STREAL techniques. The red outline shows the tumor area based on the B-mode image.	58
Figure 3-1: B-mode (A), axial strain (B), lateral strain (C) and relative Young's modulus images obtained based on the axial strain (D) and based on axial and lateral strains (E) obtained for a representative responder before and at different times after the NAC initiation. The axial and lateral strain images were generated using the STREAL technique.....	79
Figure 3-2: B-mode (A), axial strain (B), lateral strain (C) and relative Young's modulus images obtained based on the axial strain (D) and based on axial and lateral strains (E) obtained for a representative non-responder before and at different times after the start of NAC. The axial and lateral strain images were generated using the STREAL technique.	80
Figure 3-3: Histopathology images of surgical specimens obtained from representative responding and non-responding patients.	81
Figure 3-4: Relative changes in tumor stiffness compared to baseline after the start of NAC for responding and non-responding patient cohorts, estimated based on axial strain ratio (A), lateral strain ratio (B), E ratio obtained from the axial-strain-based relative Young's modulus image (C), E ratio obtained from the axial/lateral-strain-based relative Young's modulus image (D).	82
Figure 3-5: Relative changes in tumor size compared to baseline after the NAC initiation for responding and non-responding patient cohorts.	82

List of Acronyms and Abbreviations

AAC	Average Acoustic Concentration
ACE	Attenuation Coefficient Estimation
ANOVA	Analysis of Variance
ASD	Average Scatterer Diameter
AUC	Area Under the Curve
BI-RADS	Breast Imaging Reporting and Data System
B-mode	Brightness mode
BRCA	Breast Cancer (gene)
CA	Contrast Agent
CIRS	Computerized Imaging Reference Systems
CNB	Core Needle Biopsy
CNR	Contrast-to-Noise Ratio
CT	Computed Tomography
DCE	Dynamic-Contrast Enhanced
DCIS	Ductal Carcinoma In Situ
DOSI	Diffuse Optical Spectroscopic Imaging
DP	Dynamic Programming
ECM	Extracellular Matrix
ER	Estrogen Receptor
FEM	Finite Element Modeling (Method)
FDG	Fluorodeoxyglucose
FLT	Fluor thymidine
FNAB	Fine Needle Aspiration Biopsy
FOV	Field of View
GLUE	Global Ultrasound Elastography
IAUC	Initial Area Under the time-signal Curve
IDC	Invasive Ductal Carcinoma
ILC	Invasive Lobular Carcinoma
LABC	Locally Advanced Breast Cancer
LCIS	Lobular Carcinoma In Situ
MBF	Midband Fit
MRI	Magnetic Resonance Imaging
NAC	Neoadjuvant Chemotherapy
NMI	Normalized Mutual Information
OBSP	Ontario Breast Screening Program
OF	Optical Flow
PET	Positron Emission Tomography
PR	Progesterone Receptor
QUS	Quantitative Ultrasound
RCB	Residual Cancer Burden
RECIST	Response Evaluation Criterion in Solid Tumors
RF	Radio Frequency

ROC	Receiver Operating Characteristics
RSI	Relative Signal Intensity
RT-SWE	Real-time Shear-wave Elastography
SAS	Spacing Among Scatterers
SE	Strain Elastography
SI	Spectral Intercept
SNR	Signal-to-Noise Ratio
SOUL	Second-order Ultrasound Elastography
SS	Spectral Slope
STREAL	Strain Refinement Algorithm
SWE	Shear-wave Elastography
TDE	Time-delay Estimation
US	Ultrasound
USE	Ultrasound Elastography
WHO	World Health Organization

Chapter 1

1 Introduction

1.1 Background and Motivation

1.1.1 Breast Cancer

The most common cancer diagnosed in Canadian women is breast cancer (excluding non-melanoma skin cancers) [1]. This type of cancer has the second-highest mortality rate among cancer-affected women, after lung and bronchus [2]. While it can also occur in men, its incidence rate in the male sex is low [1]. 27,700 Canadian women were estimated to be diagnosed with breast cancer in 2021, representing 25% of all women's cancer cases. Furthermore, in the same year, it was estimated that breast cancer would claim the lives of 5,400 Canadian women, 13% of all cancer deaths among women [1]. The daily estimation of new breast cancer cases and deaths from breast cancer are 76 and 15 Canadian women, respectively. Additionally, Canadian men were estimated to develop breast cancer at a rate of 260 per year with 55 of them dying from the disease in 2021 [1].

The female breast contains three different types of tissue: fibrous (or connective) tissue, glandular tissue, and fatty tissue [3]. The proportion of each of these tissue types differs from person to person. If a person has dense breasts, it implies that she has more fibrous and glandular tissue and less fatty tissue. The fibroglandular tissue in the breast includes 15 to 20 lobes, each including several lobules, where milk is made. Lobules are connected to the ducts that lead out to the nipple.

Breast cancers are mostly originated from the cells that make up the lobules and terminal ducts. This happens when the cells proliferate and divide uncontrollably, resulting in a mass of tissue known as a tumor. Cancerous cells can be either *in situ* or invasive based on whether they penetrate through the basement membrane. Lobular carcinoma *in situ* (LCIS), a type of cancer that only develops in the female breast, originates from the terminal duct lobular units, whereas, in ductal carcinoma *in situ* (DCIS) the cancerous cells start developing inside a milk duct in the breast [4]. In both of these cancer types, the cancer cells are confined to the area where they initially formed. On the other hand, in invasive

ductal and lobular carcinoma (IDC and ILC), the cancerous cells can spread into the breast tissue and nearby lymph nodes and beyond. Invasive breast cancers can have different features and develop in different ways. While less common than other forms of breast cancer, these cancers can be more serious.

Receptors are a special class of proteins that are attached to specific substances in the blood. All normal breast cells, as well as some breast cancer cells, have estrogen and progesterone receptors which are needed for the cells to grow. One type of categorizing breast cancer is based on the protein receptors that the breast cancer cells have. They may have estrogen receptors (ER-positive or ER+), progesterone receptors (PR-positive or PR+), human epidermal growth factor receptor (HER2-positive or HER2+), or a combination of them. HER2 protein has a great role in growing cancer cells. If the breast cancer cells have any of the above-mentioned receptors, hormone therapy can be prescribed. Inflammatory breast cancer is another aggressive type of invasive breast cancer where cancer cells block the lymph vessels in the skin, making the breast appear red and swollen. This rare condition accounts for only 1% to 5% of all breast cancer cases.

When a breast cancer has advanced locally but has not yet spread beyond the breast and local lymph nodes, it is called locally advanced breast cancer (LABC). LABC is characterized by large breast tumors (i.e., more than 5 centimeters in diameter), cancers that include the skin of the breast or the underlying muscles of the chest, or any size of tumor with multiple local lymph nodes involvement. Inflammatory breast cancer is also considered as LABC [5]. LABC does not include breast cancers that have distant metastatic spread [6]. Overall, this type of cancer includes a heterogeneous group of tumors with different characteristics and behaviors. This makes the management and treatment of LABC very challenging. Despite surgeons' best efforts to remove locoregional dissemination of the tumor, a high rate of locoregional and systemic failure has been seen [7], [8]. Therefore, other different treatment strategies have been used for LABC over the past several decades. The results of these treatments showed that multi-modality treatment approaches (surgery, chemotherapy, radiotherapy, hormonal and targeted therapy) can increase 5-year survival rate [9]–[11]. This type of cancer constitutes 10% to 20% of all diagnosed breast cancer cases [12].

1.1.2 Breast Cancer Screening, Detection, and Diagnosis

Early detection of breast cancer offers more treatment options and a higher chance of survival. Breast cancer patients who are diagnosed early have a survival rate higher than 97 percent in the first five years following diagnosis [13], [14]. Therefore, detecting breast abnormalities as early as possible is crucial for improvement of treatment outcome and increasing survival rate.

Breast cancer screening is usually done via physical examinations and screening mammography. In case of dense breasts, ultrasound (US) or magnetic resonance imaging (MRI) may be used for screening. Breast cancer screening is suggested to be done on people who are at risk of getting cancer but have no symptoms. Ontario Breast Screening Program (OBSP) recommends that most women in age 50 to 74 be screened every 2 years with mammography. For women in age 30 to 69, those who are known to have gene mutation, are a first-degree relative of someone with a gene mutation, have a personal or family history of breast or ovarian cancer, have had radiation therapy to the chest before age 30 and at least 8 years ago are also recommended to be referred to the high risk OBSP for further screening. Signs and symptoms of breast cancer include but are not limited to discovering a lump in the breast, swelling or asymmetry of the breast, changes in the nipple, erythema or ulceration in the skin, and axillary mass [15]. Up to 50% of women with breast complaints, however, do not present with any physical signs of breast pathology [16]. In case a suspicious lump is observed in screening, other imaging modalities may be used to characterize it for detecting breast cancer . The most common modalities used for breast cancer detection are diagnostic mammography if the breast is not too dense, US, and MRI. Although these modalities can potentially indicate whether a lesion is highly suspicious for malignancy, the gold standard approach to diagnose a malignant tumor is biopsy. Biopsy is also done to characterize the breast cancer in terms of grade, molecular features/subtypes, etc. for treatment planning. The result of all these diagnostic methods is described using a standard approach known as BI-RADS (Breast Imaging Reporting and Data System), which divides the results into six categories that are summarized in Table 1-1 [17], [18].

Table 1-1: BI-RADS categories description [17], [18]

BI-RADS Category	Assessment	Management/recommendation
0	Incomplete evaluation	Further imaging required
1	Negative examination	
2	Benign	
3	Probably benign (non-palpable and circumscribed mass on a baseline mammogram)	Short-interval follow-up
4	Suspicious abnormality: 4A: low probability of malignancy (2%-10%) 4B: intermediate probability of malignancy (10% to 50%) 4C: high probability of malignancy (50% to 95%)	Biopsy
5	High probability of malignancy (>95%)	Biopsy
6	Pathology proven malignancy	Treatment ongoing

1.1.2.1 Physical and Clinical Breast Exam

Breast examination includes inspection, palpation, and lymph node exam. During inspection, shape, size, and symmetry characteristics of the breasts are recorded. The

clinician also records any evidence of edema, erythema or ulceration of skin or the nipple. The breast is then carefully and gently palpated. During palpation, the type of the tumor (malignant or benign) can sometimes be determined based on some features of the identified lesions. For example, most of benign lesions have very regular borders, whereas cancerous lesions tend to be irregular in shape [19]. Also, a very stiff lesion is most likely malignant, while benign lesions show more deformability and rubbery behavior [20]–[23]. Although these characteristics can better be identified through more advanced detection methods such as mammography or ultrasound, they can be beneficial for early detection or self-examination.

1.1.2.2 Mammography

Mammography involves acquiring X-ray images of the breast with low radiation doses. This imaging modality can potentially detect both cancerous (malignant) and non-cancerous (benign) tumors in the breast. Mammograms, which are images obtained using this modality, can be helpful in finding small lumps in the breast that cannot be sensed by hand during physical examination. However, they are known to be insufficient for early diagnosis of breast cancer in women who have a higher risk of cancer in their family or have a Breast Cancer (BRCA) gene mutation. Breast cancer can be detected at an early stage by annual screening mammography, which monitors changes in the breast over time [14]. Subsequently, diagnostic mammography is used as a complementary modality for more accurate diagnosis. While effective for screening, mammogram interpretation is one of the most technically challenging areas of radiology, especially in dense breasts. This stems from that the X-ray attenuation coefficient of breast cancers and fibroglandular tissues are similar. For this reason, clinicians look for regions with microcalcification and shape irregularity that are usually signs of malignancy [24]. This makes it complex for the radiologist to identify the cancerous areas. It has been observed that women with dense breasts are more likely to develop breast cancer [25]–[27] while about half of breast cancers in women with dense breasts are missed by mammograms [28], [29]. Therefore, it is important for women with dense breasts to be screened by supplemental imaging techniques such as ultrasound or MRI which are better at distinguishing fibroglandular tissue and cancerous tissue.

1.1.2.3 Breast Ultrasound

Ultrasound imaging of the breast was first described in 1951 [30]. For the diagnosis and management of breast abnormalities, ultrasound can be a useful adjuvant to mammography [31]. A brightness mode (B-mode) ultrasound image is a cross-sectional image that depicts the body's tissues and organ borders. It is made up of echoes created by ultrasonic waves reflecting at tissue boundaries and scattering from other small structures within tissues. The term B-mode refers to the relationship between the brightness of the image at each place and the strength or amplitude of the echo. B-mode images can provide information on the shape and internal structure of lesions from various planes with great resolution in both fatty and dense breasts. Furthermore, other novel technologies associated with ultrasound has distinguished it from other imaging techniques. These technologies include ultrasound elastography, contrast-enhanced ultrasound, three-dimensional ultrasound, and automatic breast ultrasound. Among these technologies, ultrasound elastography is the focus of this thesis and will be further discussed in Section 1.2.2 of this chapter.

1.1.2.4 Breast Magnetic Resonance Imaging (MRI)

MRI scans the distribution and magnetic properties of hydrogen atoms within human tissue by using repetitive radiofrequency pulses in conjunction with precise spatial modulation of a high magnetic field. With sensitivity ranging between 81% and 100% and specificity of around 97%, it is known to have the highest accuracy for breast cancer detection compared to other imaging modalities [32], [33]. Although ultrasound does not have any supplemental value and information when MRI is used, it still outperforms MRI in being cost-effectiveness and accessible, especially for women at lower risk.

1.1.2.5 Biopsy

If an area is identified as suspicious, a breast biopsy may be recommended. This is when the assessment of breast cancer is assigned to BI-RADS 4 or 5. During breast biopsy, a sample of breast tissue is removed for histopathology to confirm a malignancy and determine the receptor status, molecular features, grade, and extent of the cancer. Specifically, sentinel node biopsy can be used to see if cancer has progressed beyond the

primary tumor location and into the lymphatic system. Fine-needle aspiration biopsy (FNAB), which involved aspirating a small amount of tissue with a very thin needle, is frequently used to confirm the diagnosis before a treatment is planned. Core needle biopsy (CNB) is another type of biopsy which uses a larger needle for sampling the suspicious areas. To accurately localize the suspicious area, the radiologist often utilizes other imaging techniques such as ultrasound, MRI, or positron emission tomography (PET) as a guidance for biopsy [34]–[38]. In some rare cases a surgical biopsy is required in which the breast mass is surgically removed [39]. Although both FNAB and CNB have shown high sensitivity (87% and 74%, respectively) and specificity (98% and 96%, respectively) in cancer diagnosis [40], it is an invasive method and carries potential risks and side effects. Nevertheless, it is the gold standard method to confirm that a lesion is malignant and is required for treatment planning.

1.1.3 Breast Cancer Treatment

The treatment of breast cancer mostly depends on the subtype and stage of the cancer [41]. It also depends on age, general health, menopausal status, and genetic factors. TNM staging system is used for most types of cancer. This system uses letters and numbers to describe the tumor (T), lymph nodes (N), and whether or not the cancer has spread or metastasized (M) [42]. Additionally, for some cancer types, other factors such as grade, biomarker, and tumor genetics can be included in the staging of the cancer. Generally, for most of the cancers, severity is characterized through a number (stage 0 to IV), with 0 being cancer *in situ*, and IV being advanced or metastatic cancer.

Stage of the breast cancer as well as the tumor's type are important for planning out its treatment and management. Surgery, radiation therapy, chemotherapy, hormonal therapy, targeted therapy, and immunotherapy are among treatment options for breast cancer. For example, for early-stage invasive breast cancer or DCIS, surgery is recommended to remove the tumor before it grows further, while for LABC which is characterized by larger tumors, chemotherapy, radiotherapy, or hormonal therapy is recommended before the surgery. This is called neoadjuvant therapy. This method of treatment makes the surgery feasible because the tumor shrinks as a result of preoperative therapy. Another advantage

of neoadjuvant therapy is potentially paving the way to a less invasive of lumpectomy instead of mastectomy. Furthermore, in case there is any microscopic distant disease, it will be treated early on, hence potentially preventing cancer recurrence.

The effectiveness of therapy on cancer cells is measured in terms of “response”. There were various efforts in defining standardized response assessment criteria. World Health Organization (WHO) criteria was the first large scale published criteria [43]. This criterion described how to measure the lesion in detail. The size of the lesion was calculated as two-dimensional measure with multiplication of longest diameter by its perpendicular one [43]. Response Evaluation Criteria in Solid Tumors (RECIST) was later introduced [44]. In this criterion, the response rate was measured using unidimensional measurement of the tumor as opposed to the bidimensional measurement in WHO criteria [44]. In addition, one of the most important indicators of response is tumor histopathological change (based on residual tumor cellularity) after neoadjuvant chemotherapy (NAC) [45], [46]. In some cases, tumor shrinkage is not evident on standard imaging despite a histopathological response. Hence, some studies [47], [48] have applied a modified response grading system that is based on RECIST [44] and histopathological criteria [45]. It has been shown that there is a significant correlation between the patient’s response to NAC and treatment outcome, which leads to improved survival rate [49]–[52]. However, less than 30% of patients show complete response to standard chemotherapy while about 30% to 40% of the patients are complete non-responders [53]–[58]. Techniques used for breast cancer diagnosis can potentially be used to monitor and assess the patient’s response with variable degrees of effectiveness. Predicting patients’ response accurately and as early as possible after NAC initiation may allow clinicians to make treatment adjustments. More details about different techniques in this context will be provided in Section 1.2.1 of this chapter and Chapter 3.

1.2 Theory

This thesis is founded on several background topics. In this section, an overview of these topics is provided.

1.2.1 Elastography

Elastography is a novel non-invasive imaging technique that involves generating images of tissue mechanical properties (elastograms). This technique involves measurement of tissue deformation using specialized imaging modalities while an external mechanical force is applied to the tissue. While other imaging modalities such as MRI have been used for measuring tissue deformation, ultrasound elastography (USE) has emerged in clinic because of its wide availability and relatively low cost. USE was first introduced and described in the 1990s [59] but has been further developed in recent years. Currently available UE techniques in the clinic can generally be classified into two groups of quasi-static and shear wave imaging. Other elastography techniques such as linear elastography and non-linear elastography (hyper elastography) have been also investigated to obtain more accurate elastograms that can potentially be used in more sensitive diagnostic applications.

To generate elastograms, tissue elasticity needs to be measured. In an entirely elastic material, elasticity can be described by Hooke's law as shown in Equation (1-1) [60]. In this equation, σ and ε are the stress and strain tensors, respectively and C is the Christoffel rank-four tensor consisting of 21 independent elastic constants [61]–[63].

$$\sigma = C\varepsilon \quad (1-1)$$

Depending on the method of deformation, three main types of elastic moduli: Young's modulus (E), shear modulus (G), and bulk modulus (K) can be considered. The magnitude of elastic modulus directly relates to the stiffness. The greater the elastic modulus the lower the material's tendency to deform, hence, the stiffer the material. In the following, different types of elastography methods in which different elastic moduli are measured will be further discussed in detail.

1.2.1.1 Ultrasound Shear Wave Elastography

In Shear Wave Elastography (SWE), a quantitative measurement of tissue stiffness is estimated using the propagation velocity of shear waves inside the tissue. This is done by generating shear waves using high-intensity pulses from the ultrasound transducer and

propagating them into the tissue perpendicular to the ultrasound beam. The shear wave speed (C_s) can then be related to the shear modulus (G) using Equation (1-2) in which ρ is the material's density.

$$C_s = \sqrt{\frac{G}{\rho}} \quad (1-2)$$

Young's modulus (E) can also be measured in this technique using the relationship between E and G which is as follows [64]:

$$E = 2(\nu + 1)G \quad (1-3)$$

In the equation above, ν is the Poisson's ratio which is usually approximated as 0.5 in soft tissues. The reason for this approximation will be discussed in section 1.2.3.1. To summarize, in SWE, an acoustic radiation force is induced into the tissue, leading to a shear wave traveling through the tissue. Ultrasound imaging can then be used to see how fast this wave travels through breast tissue, leading to an estimation for the stiffness of the tissue and creating elasticity images [65].

1.2.1.2 Ultrasound Strain Elastography

In strain imaging, the normal strain as a result of an applied normal stress to the tissue is measured. The measured strain can be imaged and used for assessment of tissue stiffness. The normal stress is applied to the tissue via quasi-static stimulation of the tissue with an ultrasound transducer while the RF data is being acquired. Using two RF data frames corresponding to two compression states, the tissue displacement can be estimated [66]–[69]. The tissue strain image is then calculated by spatially differentiating the displacement fields. Assuming all tissue experiences uniform stress distribution, a region with higher stiffness experiences less strain (deformation) than softer surrounding regions. This information can be used for detecting a hard lesion within the tissue. While strain imaging mostly relies on the derivative of the displacement which is in the same direction as the external load, i.e., axial displacement, the displacement perpendicular to the direction of external load or the lateral displacement field can also be useful in reconstructing more

accurate elastograms for the purpose of linear elastography. More on this type of elastography will be discussed in Section 1.2.1.3.

Several methods exist to estimate axial and lateral displacements using US radiofrequency (RF) data, however, the influence of noise on displacement estimation remains a problem, hence encouraging the development of noise reduction techniques necessary for image reconstruction. Current efforts for noise reduction are based on US signal processing or dedicated offline algorithms. On the US side, [70] and [71] introduced non-axial oscillations/modulations in their respective imaging point spread functions, and [72] where angular compounding is used to improve lateral displacements. Offline, algorithms focus on time delay estimation (TDE) [67], [73]–[80]. TDE methods can be categorized into regularized optimization-based, and window-based approaches. More details on these methods will be discussed in Chapter 2. While the current motion tracking methods can produce reasonably accurate axial displacement maps, the accuracy of their lateral displacements are generally low. The reason is that lateral resolution is usually not as good as axial resolution; because while axial resolution is limited by the ultrasound system and transducer frequency, the limiting factor for lateral resolution is the beam width. At their core, the motion-tracking techniques rely on regularization through imposing tissue continuity and various field smoothness criteria. Utilizing tissue mechanics constraints such as incompressibility, compatibility and tissue 3D deformation models have not been rigorously investigated for formulating more effective regularization to find more accurate 2D displacement fields. In Chapter 2 of this thesis, a tissue mechanics-based algorithm will be introduced that uses an initial estimation of axial and lateral displacements generated from any motion-tracking method before using tissue mechanics principles as constraints to further refine the axial and lateral displacement fields. The initial estimation of displacement field in this work is obtained from a previously developed technique called Global Ultrasound Elastography (GLUE) [74]. Furthermore, the results of this method will be compared to one of the current state-of-the-art motion tracking methods called Second-order Ultrasound Elastography (SOUL) [81]. Below, an overview of each of these techniques will be given.

1.2.1.2.1 Global Ultrasound Elastography (GLUE)

Global Ultrasound Elastography (GLUE) [74] is a regularized optimization-based approach that utilizes two consecutive frames of RF data, one before the deformation of the tissue, and one after that, to calculate the corresponding axial and lateral displacement fields. In this method, the cost function incorporates similarity of echo amplitudes and displacement continuity. In the first step of this method, dynamic programming (DP) is used to calculate an initial integer displacement estimate. After that, DP estimates are refined by minimizing a cost function that incorporates first-order displacement continuity of the whole field. The novelty of this method is that it globally calculates TDE of all the RF data simultaneously. Although, this simultaneous estimation allows a significant improvement in the quality of both axial and lateral displacement, it only uses first-order continuity in the cost function, thus strain continuity is not considered. Furthermore, there is no evidence that the displacements generated using this technique follow tissue mechanics principles reasonably accurately. Therefore, further investigation is needed to develop techniques capable of generating more accurate displacement fields.

1.2.1.2.2 Second-order Ultrasound Elastography (SOUL)

Second-order Ultrasound Elastography (SOUL) [81] is another regularized optimization-based technique that, similar to GLUE, starts with obtaining an initial estimate of displacements using DP. However, the cost function for SOUL incorporates both first-order and second-order regularization terms. With this change in the cost function, the applied constraint represents the mechanics of tissue deformation more accurately. This method can potentially result in more accurate displacement and strain fields, however, the focus of that is the deformation data in the axial direction while estimation of the lateral displacement field still has room for improvements.

1.2.1.3 Linear Elastography

While strain imaging has been shown to be useful for some clinical applications [68], [69], [82], uniform stress distribution is an unrealistic assumption as tissue heterogeneity and irregular loading on the organ's surface lead to a non-uniform stress distribution. Therefore, its accuracy in mapping tissue stiffness is limited. As such, more advanced

techniques have been developed to image more reliable measures of tissue stiffness (e.g., Young's modulus) using the measured displacement field. Several studies have investigated different methods for estimating non-uniform distribution of stress which allow the mechanical properties (stiffness) of the tissue to be measured [83]–[86]. Commonly, this is done via tissue mechanical simulation formulated from well-established physical laws and provide equations that relate the biomechanical properties (shear modulus, Poisson's ratio, anisotropy, viscosity, non-linearity, and poroelasticity) to the measured mechanical response. Having infinitesimal deformations, linear elastic behavior for soft tissues is a valid assumption. In this case, the strain and stress tensor can be related as shown in Equation (1-1). It is difficult to solve these equations on irregular and complex geometries; therefore, numerical methods such as finite-element method (FEM) are used to solve for elastic constants and determine the distribution of stiffness throughout the tissue. As mentioned in the previous section, accurate reconstruction of a tissue's relative Young's modulus (YM) image requires accurate tissue displacement, and strain data in both axial and lateral direction. Therefore, improving the accuracy of these fields can have a significant impact on the quality of the reconstructed elastograms.

1.2.1.4 Non-linear Elastography

The stress-strain relationship in soft tissues can only be assumed as linear within a small range of deformation. For higher range of deformation or strain, soft tissue exhibits intrinsic or geometric non-linearity. Intrinsic non-linearity is related to the physiological components of the tissue while geometric non-linearity is defined as the change in stiffness due to load redistribution corresponding to significant change in geometry [87]. As such, most investigations and available data in the literature is based on applying small deformation (strain less than 10%) to the soft tissue to be able to use the linear assumption for strain imaging and modulus reconstruction. However, tissue non-linear behavior is known to be useful for representing the tissue mechanical properties more accurately [88], [89]. Nonlinear elastography aims at reconstruction of tissue hyperelastic parameters. This can be done using iterative data inversion techniques.

1.2.2 Mechanics Principles

1.2.2.1 Incompressibility Condition

An incompressible material is a material that preserves its volume when it undergoes deformation. Since for a mechanical body, the divergence of the displacement vector relates to the change in the volume, an equivalent condition for a material to be incompressible is that the divergence of the displacement field is zero. This can be written as Equation (1-4) in cartesian coordinates.

$$\nabla \cdot U(x, y, z) = \partial u_x / \partial x + \partial u_y / \partial y + \partial u_z / \partial z = 0 \quad (1-4)$$

For such material, the Poisson's ratio which is a measure of Poisson effect is usually approximated at ~ 0.5 . Poisson effect is the tendency of a material to expand in directions that are perpendicular to its compression direction. Fluids such as water are known to be incompressible, thus, soft tissue which mostly consists of water can be approximated as a nearly-incompressible material.

1.2.2.2 Compatibility Condition

A compatible material is a body that deforms without creating any gaps or overlaps. Consequently, compatibility conditions are mathematical conditions that indicate whether or not a certain deformation will result in a compatible state for the material. Such deformation (or strain) is called a compatible strain tensor field which ascertains that the material stays together after the deformation and the material's displacement field is single-valued and continuous. The 2-D compatibility equation (Equation (1-5)) shows the relationship between the strains in a two-dimensional case for a compatible material.

$$\frac{\partial^2 \varepsilon_{xx}}{\partial y^2} + \frac{\partial^2 \varepsilon_{yy}}{\partial x^2} = 2 \frac{\partial^2 \varepsilon_{xy}}{\partial x \partial y} \quad (1-5)$$

1.2.2.3 Boussinesq Stress Distribution

In 1885, Boussinesq introduced a solution for determining the distribution of the stress in a homogeneous and isotropic solid that can be modeled as semi-infinite medium [90]. A homogeneous solid is the one that consists of only one material, or the mechanical

properties remain the same throughout the solid. The solid is considered to be isotropic if its mechanical properties do not depend on the direction of loading. Finally, a semi-infinite model has a single plane surface and extends to infinity in all directions. The Boussinesq stress equations are calculated as a result of a point load applied to the surface. Stresses in x, y, and z directions can be calculated using Equations (1-6), (1-7), and (1-8). In these equations, (x_0, y_0, z_0) and (x, y, z) are the coordinates of points T and P shown in Figure Figure 1-1, respectively, while r is the Euclidean distance between them.

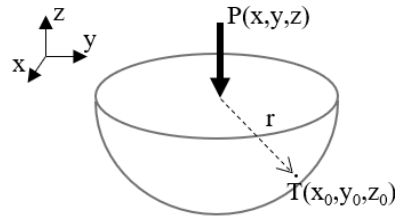


Figure 1-1. A schematic of a semi-infinite medium under a point load

$$\sigma_{xx} = \frac{P}{2\pi} \left\{ \frac{3(z_0 - z)(x_0 - x)^2}{r^5} - (1 - 2\nu) \left[\frac{(x_0 - x)^2 - (y_0 - y)^2}{r(r^2 - (z_0 - z)^2)(r + (z_0 - z))} - \frac{(y_0 - y)^2(z_0 - z)}{r^3(r^2 - (z_0 - z)^2)} \right] \right\} \quad (1-6)$$

$$\sigma_{yy} = \frac{P}{2\pi} \left\{ \frac{3(z_0 - z)(y_0 - y)^2}{r^5} - (1 - 2\nu) \left[\frac{(y_0 - y)^2 - (x_0 - x)^2}{r(r^2 - (z_0 - z)^2)(r + (z_0 - z))} - \frac{(x_0 - x)^2(z_0 - z)}{r^3(r^2 - (z_0 - z)^2)} \right] \right\} \quad (1-7)$$

$$\sigma_{zz} = \frac{3P}{2\pi} \frac{(z_0 - z)^3}{r^5} \quad (1-8)$$

Furthermore, it is noteworthy that in these equations it is assumed that the solid is weightless, unstressed, and obeys Hooke's law. The solution developed by Boussinesq takes advantage of zero displacement, strain, and stress boundary conditions at the boundaries of the semi-infinite medium.

1.3 Literature Review

As mentioned earlier in this chapter, evaluating patient's response is important specially for LABC patients who are prescribed with multi-modality treatments. Current methods for this evaluation involve either conventional (standard) methods such as monitoring tumor size changes, and other novel investigational methods such as functional, metabolic, or molecular changes. Monitoring tumor size changes can be done using physical examination or standard anatomical imaging such as mammography, B-mode ultrasound imaging, or MRI. The major problem with these conventional methods is that such changes may take several months to become detectable. Therefore, they cannot be efficiently used for early detection of patients' response. In contrast, functional and molecular changes occur long before morphological changes. Functional imaging modalities that have been investigated for evaluating patients' response include Dynamic Contrast Enhanced (DCE) MRI, PET imaging, molecular breast imaging, and elastography. In this section, we will review these imaging techniques and their performance in response evaluation.

1.3.1 Dynamic Contrast Enhanced (DCE) MRI

DCE-MRI can be used to assess multiple and quantifiable parameters related to tissue perfusion and microvascular status. It is done by first acquiring images without contrast enhancement, and then acquiring images over time during and after injection of a paramagnetic contrast agent (CA) into the vascular system [91]. Consequently, DCE-MRI examines the vascular environment over various timepoints, and the fluctuating signal can be described using quantitative enhanced kinetic characteristics. Semi-quantitative enhancement kinetic features, such as initial peak enhancement and the presence of delayed phase washout are used to improve specificity for identifying malignancy [92].

In the evaluation of response to NAC, DCE-MRI tends to be more effective than mammography or ultrasound. In a study of 24 patients, DCE-MRI was performed before

and on average 19 days after the first NAC treatment cycle [93]. The parameters used in this study were relative signal intensity (RSI) and area under the curve (AUC) which were calculated from the DCE-curves. RSI was calculated by dividing the mean signal intensity of images after CA injection to the mean signal intensity in the pre-contrast images. AUC was calculated by numerically integrating the signal enhancement curves in each image voxel [93]. This study concluded that DCE-MRI has the potential to predict 5-year survival in patients with LABC with an area under the receiver operating characteristic (ROC) curve (AUC) of 0.77 [93]. Furthermore, changes in tumor vascularization can be assessed after one cycle of NAC [94]. In a study conducted in 2013, 21 patients with LABC underwent high temporal resolution 3T DCE-MRI before and after one cycle of NAC to determine if semi-quantitative analysis of high temporal resolution DCE-MRI can predict the response to NAC in patients with LABC [94]. The assessed parameters for this purpose included lesion size, radiologist's subjective assessment of lesion enhancement, and percentages of voxels within the lesion demonstrating progressive, plateau, or washout kinetics. If the signal intensity of a voxel increases gradually and in a linear way this is called 'progressive'; if it stays around the same value over time, this is commonly called as a 'plateau', and in case the signal fades gradually, it is referred to as a 'washout'. The results were promising and demonstrated that while parameters such as lesion size cannot predict patients' response after one cycle of NAC, change in percentage of voxels demonstrating washout kinetics could discriminate responder and non-responder patients [94].

A more recent paper, studied 38 LABC patients who received NAC for 1-3 months while their ultrasound, mammography and MRI data were compared to histopathology results [95]. Type of response was determined with respect to the "Response Evaluation Criteria in Solid Tumors (RECIST) 1.1" [96]. The correlation between the response type of all three imaging modalities and histopathology response were assessed and compared. It was shown that this correlation was very weak in mammography or ultrasound, whereas with DCE-MR, it was possible to evaluate the treatment response accurately in 84.2% of the patients 1-3 months after NAC [95]. In the same year, another study in the same area was conducted to assess the potential of texture analysis applied to DCE-MRI for predicting clinical and pathological response to NAC in patients with LABC. With a dataset including 58 LABC patients undergoing NAC, they presented promising results in the use of texture

analysis of DCR-MR images for the use of NAC response prediction in LABC patients [97]. Studying 35 patients diagnosed with stage II/III of breast cancer, quantitative, multiregional analysis of DCE-MRI was used to predict pathological response of breast cancer to NAC. The parameter for predicting pathological response was the change in texture features in different subregions of tumor. According to their results, they concluded that the heterogeneity of the tumor subregions on DCE-MRI can predict pathological response to NAC in breast cancer [98]. In another similar study, DCE-MRI was acquired in 14 patients at baseline, after two cycles, and after the end of chemotherapy sessions. Several dynamic contrast parameters such as transfer constant (diffusion of contrast media from the vascular space to the tumor interstitium which is a measure of vascular permeability), rate constant (the period that takes for the contrast agent to diffuse back into the vasculature), the extracellular extravascular space, initial area under the time signal curve (IAUC), apparent diffusion coefficient (ADC), and enhancement curve were generated for the purpose of comparison between responders and non-responders. In this study, IAUC and ADC were found to be useful in distinguishing responders from non-responders after two or three cycles of chemotherapy [99].

It is noteworthy that although it has shown promise for evaluating breast cancer response to NAC, DCE-MRI is relatively expensive, not widely accessible, and involves injection of exogenous contrast agents for each assessment during treatment.

1.3.2 Positron Emission Tomography (PET)

Several studies have shown that nuclear medicine imaging, such as positron emission tomography (PET), can be used to assess tumor response to treatment by detecting early changes in tumor metabolism. ¹⁸F-flurodeoxyglucose (FDG), a glucose analogue, can be a measure of tissue glucose metabolism which is often high in high-grade cancers and low in low-grade tumors. To evaluate its efficacy in response detection, FDG-PET/CT was performed on 40 patients with invasive ductal carcinoma at baseline and after two cycles of NAC [100]. Pathologic response of these patients was evaluated after surgery using Residual Cancer Burden (RCB) index [101]. Their results suggest that FDG-PET/CT can discriminate NAC responder and non-responder patients after two courses of NAC with 68% sensitivity and 75% specificity [100]. An older study with 14 patients has also proved

the usefulness of 3'-[F-18]Fluoro-3'-deoxythymidine (FLT)-PET in monitoring breast cancer response to chemotherapy after two weeks from the first course of chemotherapy where a significantly reduced FLT uptake was observed compared to pretreatment scans [102]. Similar to DCE-MRI, this imaging modality is very costly, has limited accessibility and need the injection of radionuclide contrast agents. This limits the frequency of scanning patients for response evaluation throughout the chemotherapy course.

1.3.3 Quantitative Ultrasound (QUS)

QUS procedures, unlike medical ultrasonography, are used to measure quantitative variables in order to characterize tissue properties rather than to acquire anatomical images from internal organs [103]. QUS assessment of breast tumor response to chemotherapy was conducted in a study involving 58 LABC patients prior to NAC treatment and at weeks 1, 4, and 8 of their treatment, and before surgery. The parameters assessed in this study include midband fit (MBF), spectral slope (SS), spectral intercept (SI), spacing among scatterers (SAS), attenuation coefficient estimate (ACE), average scatterer diameter (ASD), and average acoustic concentration (AAC) of the tumor region. The results indicated that a hybrid QUS biomarker (MBF, SS, and SAS) was able to detect the response of LABC patients to NAC after 4 weeks of therapy with relatively high sensitivity and specificity (around 80%) [104]. An older study from the same group also suggested that QUS can be used for detecting tumors from normal breast tissue and also differentiating tumor grades [105]. Later, this finding was consolidated by a larger dataset (116 patients) in which surrounding tissue and tumor lesions were classified using a combination of Nakagami distribution¹ shape parameter, entropy, and texture parameters with sensitivity of 93% and specificity of 88% [106]. Using a dataset of 100 patients with breast cancer, QUS biomarkers that quantify spatial heterogeneities in size, concentration and spacing of acoustic scatterers were used and showed success in predicting treatment responses of patients [107]. In a recent study, different computational algorithms were tested on QUS and textural analysis data of 100 LABC patients to best determine tumor responses after

¹ A probability distribution related to the gamma distribution.

the start of NAC. Among linear discriminant, k-nearest-neighbor, and a nonlinear support vector machine classifier, the latter performed the best in differentiating responders from non-responders with accuracies of 78%, 90%, and 92% at weeks 1, 4, and 8 after NAC initiation [108]. The same classifier with another dataset of 59 LABC patients showed the highest accuracy of 81% at weeks 1 and 4 with area under curve (AUC) values of 0.87 each in classifying patients based on their response [109]. The underlying principle of these studies is that QUS biomarkers which are related to the linear regression of the tissue power spectrum are directly related to the tissue microstructure, thus, can characterize the abnormalities of different tissues e.g. breast [110]. Moreover, QUS has shown to be effective in detecting and quantifying tumor cell death *in vivo*, in response to various treatments such as photodynamic therapy, radiation therapy, chemotherapy, and anti-vascular therapy [111]–[114]. To conclude, QUS shows highly accurate results, and its hardware system is inexpensive, smaller than that of other similar imaging systems, and do not require the use of ionizing radiation or contrast agent injection.

1.3.4 Breast Ultrasound Elastography

Several studies have shown that there is a significant correlation between chemotherapy response and tumor softening [115], [116]. In other words, given that chemotherapy causes apoptosis and other forms of cell death in tumors, ECM composition is expected to be considerably altered during effective treatment [117]–[121]. Tissue stiffness reduction could be one signature of such changes. A study involving 15 patients with LABC showed that relative tumor stiffness can be a differentiating factor between NAC responders and non-responders after 4 weeks of treatment initiation [115]. The feasibility of strain imaging and real time shear wave elastography (RT-SWE) to evaluate early tumor response to chemotherapy was demonstrated in [122] using an animal model. Although most studies reported tumor softening as a result of chemotherapy, this investigation showed that the stiffness of tumor determined by UE increases in response to chemotherapy at a very early stage i.e., at the day after the last dosing [122]. In another study, mass characteristic frequency, shear wave elastography, and mass size were used for assessing early prediction of tumor response to NAC in a dataset of 62 patients with biopsy-proven invasive breast cancer. The SWE was acquired at three time points: before, mid-course, and after NAC.

An SWE parameter which can be explained as the inverse of the maximum shear wave propagation time in a breast mass showed a significant difference between responders and non-responders in the mid-course of NAC treatment [116]. Ultrasound strain elastography has also shown to be useful with high sensitivity (84%) and specificity (85%) in another study for predicting response to NAC as early as two weeks after the start of treatment [123]. With low cost and readily availability, ultrasound elastography is known to be highly efficient in the clinical setting. Further improving the accuracy of response prediction using this imaging modality, by addressing its issues and enhancement of its underlying algorithms of displacement data estimation and image reconstruction, can potentially make this modality highly competitive compared to other methods in predicting NAC response in LABC patients.

1.4 Objectives

The overarching objective of this study is to develop novel methods for ultrasound elastography to improve its accuracy and reliability in clinical settings. Once developed, the methods were applied to a clinical dataset acquired through an observational study on LABC patients who underwent NAC. Results from this study was used to assess the efficacy of our enhanced ultrasound elastography technique in evaluating LABC patient response soon after the start of NAC.

The focus of our work is on quasi-static ultrasound elastography where the tissue is externally excited by pressing the ultrasound probe against the breast. The first specific aim of research included in this thesis is to develop a novel technique which uses mathematical constraints derived from fundamental tissue mechanics principles to regularize displacement and strain fields obtained using existing methods. The second specific aim focuses on evaluating this development for early determination of LABC patients' response to NAC. In this aim the technique developed in the previous specific aim is used within a full inversion elastography framework to obtain Young's modulus images of a clinical dataset of a group of LABC patients undergoing NAC. The Young's modulus ratio of tumor to the healthy tissue was then calculated to assess the correlation

between change in the tumor Young's modulus throughout the NAC and the final response of the patients.

1.5 Thesis Outline

The thesis objectives defined above has been pursued in the following chapters followed by a final chapter where the thesis summary and future work are discussed. The outline of each chapter is explained below.

1.5.1 Chapter 2

In ultrasound elastography, tissue displacements are mainly measured based on RF data correlation while the physics governing tissue deformation is hardly considered. Previous studies have shown that soft tissue can be modelled as incompressible material. Furthermore, like other continua, soft tissue deforms without developing any gaps/overlaps, hence mathematically constraining the relationship between different components of the displacement field. Furthermore, to account for 3D tissue incompressibility, a novel method was developed and used for estimating out-of-plane strain data based on axial and lateral strain data which can be derived from 2D US RF data. In this chapter, we present a novel technique developed based on the above mentioned principles for refining displacement and strain fields which were previously measured using conventional methods. The technique was validated using an *in silico* breast ultrasound model, four tissue-mimicking phantoms, and clinical breast ultrasound elastography. The results show significant improvement in accuracy, SNR and CNR of both displacement and strain fields.

1.5.2 Chapter 3

In this chapter, first, a technique was developed for the purpose of reconstructing Young's modulus as a measure of tissue stiffness. The technique follows a full-inversion finite element framework to which the enhanced displacements are fed as input data while the boundary conditions of the US FOV was also derived from these displacements. Next, this more accurate full-inversion-based ultrasound elastography was adapted to evaluate its

performance in predicting the response of a group of 25 LABC patients to NAC. The technique was utilized using data acquired before and at weeks 1, 2, and 4 after the start of NAC. The Young's modulus ratio of tumor to the surrounding tissue was calculated at different scans and compared to the baseline for each patient. Patients' response to NAC was determined many months later using standard clinical and histopathological criteria. Results of the enhanced elastography technique proposed in this study demonstrate a high potential for chemotherapy response monitoring in LABC patients.

1.5.3 Chapter 4

The information presented in previous chapters is summarized in this chapter. The dissertation was closed by proposing possible directions for this study in the future.

References

- [1] “Breast cancer statistics | Canadian Cancer Society.” <https://cancer.ca/en/cancer-information/cancer-types/breast/statistics> (accessed Jan. 17, 2022).
- [2] L. Smith *et al.*, “Members of the Canadian Cancer Statistics Advisory Committee Analytic leads,” 2019.
- [3] Y. S. Khan and H. Sajjad, “Anatomy, Thorax, Mammary Gland,” *StatPearls*, Jul. 2021, [Online]. Available: <https://www.ncbi.nlm.nih.gov/books/NBK547666/>.
- [4] J. Makki, “Diversity of Breast Carcinoma: Histological Subtypes and Clinical Relevance,” *Clin. Med. Insights. Pathol.*, vol. 8, no. 1, p. 23, 2015, doi: 10.4137/CPATH.S31563.
- [5] D. J. A. Adamson and A. M. Thompson, “Locally advanced breast cancer,” *Breast Surg.*, pp. 219–229, Jan. 2014, doi: 10.1016/B978-0-7020-4959-0.00013-8.
- [6] O. M. Fayanju, P. B. Garvey, M. S. Karuturi, K. K. Hunt, and I. Bedrosian, “Surgical Procedures for Advanced Local and Regional Malignancies of the Breast,” *Breast Compr. Manag. Benign Malig. Dis.*, p. 778–801.e4, Jan. 2018, doi: 10.1016/B978-0-323-35955-9.00059-3.
- [7] P. K. Garg and G. Prakash, “Current definition of locally advanced breast cancer,” *Curr. Oncol.*, vol. 22, no. 5, p. e409, Oct. 2015, doi: 10.3747/CO.22.2697.
- [8] D. Simos, M. Clemons, O. M. Ginsburg, and C. Jacobs, “Definition and consequences of locally advanced breast cancer,” *Curr. Opin. Support. Palliat. Care*, vol. 8, no. 1, pp. 33–38, 2014, doi: 10.1097/SPC.0000000000000020.

- [9] M. C. Lee and L. A. Newman, "Management of patients with locally advanced breast cancer," *Surg. Clin. North Am.*, vol. 87, no. 2, pp. 379–398, Apr. 2007, doi: 10.1016/J.SUC.2007.01.012.
- [10] P. Valagussa *et al.*, "T3b-T4 breast cancer: factors affecting results in combined modality treatments," *Clin. Exp. Metastasis*, vol. 1, no. 2, pp. 191–202, Apr. 1983, doi: 10.1007/BF00121498.
- [11] W. G. Cance *et al.*, "Long-term outcome of neoadjuvant therapy for locally advanced breast carcinoma: effective clinical downstaging allows breast preservation and predicts outstanding local control and survival," *Ann. Surg.*, vol. 236, no. 3, pp. 295–303, Sep. 2002, doi: 10.1097/01.SLA.0000027526.67560.64.
- [12] B. Fowble, A. Bevan, M. Alvarado, and M. Melisko, "Cancer of the Breast," in *Leibel and Phillips Textbook of Radiation Oncology*, Elsevier, 2010, pp. 1215–1323.
- [13] A. Migowski, "[Early detection of breast cancer and the interpretation of results of survival studies]," *Cien. Saude Colet.*, vol. 20, no. 4, pp. 1309–1310, 2015, doi: 10.1590/1413-81232015204.17772014.
- [14] L. Wang, "Early Diagnosis of Breast Cancer," *Sensors (Basel)*., vol. 17, no. 7, Jul. 2017, doi: 10.3390/S17071572.
- [15] M. M. Koo, C. von Wagner, G. A. Abel, S. McPhail, G. P. Rubin, and G. Lyratzopoulos, "Typical and atypical presenting symptoms of breast cancer and their associations with diagnostic intervals: Evidence from a national audit of cancer diagnosis," *Cancer Epidemiol.*, vol. 48, p. 140, Jun. 2017, doi: 10.1016/J.CANEP.2017.04.010.
- [16] D. S. Smink, "Schwartz's Principles of Surgery, 10th Edition," *Ann. Surg.*, vol. 261, no. 5, p. 1026, May 2015, doi: 10.1097/SLA.0000000000001107.
- [17] W. A. Berg, C. Campassi, P. Langenberg, and M. J. Sexton, "Breast Imaging Reporting and Data System," *Am. J. Roentgenol.*, vol. 174, no. 6, pp. 1769–1777, Aug. 2021, doi: 10.2214/ajr.174.6.1741769.
- [18] D. A. Spak, J. S. Plaxco, L. Santiago, M. J. Dryden, and B. E. Dogan, "BI-RADS ® fifth edition: A summary of changes," *Diagn. Interv. Imaging*, vol. 98, no. 3, pp. 179–190, Mar. 2017, doi: 10.1016/J.DIII.2017.01.001.
- [19] L. I. Everson, "Mammographic Interpretation: A Practical Approach," <https://doi.org/10.1148/radiology.185.3.864>, vol. 185, no. 3, pp. 864–864, Dec. 1992, doi: 10.1148/RADIOLOGY.185.3.864.
- [20] J. Fenner, A. C. Stacer, F. Winterroth, T. D. Johnson, K. E. Luker, and G. D. Luker, "Macroscopic Stiffness of Breast Tumors Predicts Metastasis," *Sci. Reports 2014* 41, vol. 4, no. 1, pp. 1–8, Jul. 2014, doi: 10.1038/srep05512.

- [21] I. Acerbi *et al.*, “Human breast cancer invasion and aggression correlates with ECM stiffening and immune cell infiltration,” *Integr. Biol. (United Kingdom)*, vol. 7, no. 10, pp. 1120–1134, Oct. 2015, doi: 10.1039/c5ib00040h.
- [22] J. H. Youk, E. J. Son, H. M. Gweon, H. Kim, Y. J. Park, and J. A. Kim, “Comparison of strain and shear wave elastography for the differentiation of benign from malignant breast lesions, combined with B-mode ultrasonography: qualitative and quantitative assessments,” *Ultrasound Med. Biol.*, vol. 40, no. 10, pp. 2336–2344, 2014, doi: 10.1016/J.ULTRASMEDBIO.2014.05.020.
- [23] J. Yoo *et al.*, “Tumor stiffness measured by shear wave elastography correlates with tumor hypoxia as well as histologic biomarkers in breast cancer,” *Cancer Imaging*, vol. 20, no. 1, pp. 1–10, Dec. 2020, doi: 10.1186/S40644-020-00362-7/TABLES/4.
- [24] D. M. Ikeda and K. K. Miyake, “Breast imaging,” p. 465, Accessed: Jan. 28, 2022. [Online]. Available: https://books.google.com/books/about/Breast_Imaging_The_Requisites_E_Book.html?id=DhgZDQAAQBAJ.
- [25] C. I. Lee, L. E. Chen, and J. G. Elmore, “Risk-Based Breast Cancer Screening: Implications of Breast Density,” *Med. Clin. North Am.*, vol. 101, no. 4, p. 725, Jul. 2017, doi: 10.1016/J.MCNA.2017.03.005.
- [26] K. Kerlikowske, D. L. Miglioretti, and C. M. Vachon, “Discussions of Dense Breasts, Breast Cancer Risk, and Screening Choices in 2019,” *JAMA*, vol. 322, no. 1, p. 69, Jul. 2019, doi: 10.1001/JAMA.2019.6247.
- [27] S. M. Advani *et al.*, “Association of Breast Density With Breast Cancer Risk Among Women Aged 65 Years or Older by Age Group and Body Mass Index,” *JAMA Netw. Open*, vol. 4, no. 8, pp. e2122810–e2122810, Aug. 2021, doi: 10.1001/JAMANETWORKOPEN.2021.22810.
- [28] T. M. Kolb, J. Lichy, and J. H. Newhouse, “Comparison of the performance of screening mammography, physical examination, and breast US and evaluation of factors that influence them: An analysis of 27,825 patient evaluations,” *Radiology*, vol. 225, no. 1, pp. 165–175, Oct. 2002, doi: 10.1148/RADIOL.2251011667.
- [29] W. A. Berg *et al.*, “Detection of Breast Cancer With Addition of Annual Screening Ultrasound or a Single Screening MRI to Mammography in Women With Elevated Breast Cancer Risk,” *JAMA*, vol. 307, no. 13, pp. 1394–1404, Apr. 2012, doi: 10.1001/JAMA.2012.388.
- [30] J. J. Wild and D. Neal, “USE OF HIGH-FREQUENCY ULTRASONIC WAVES FOR DETECTING CHANGES OF TEXTURE IN LIVING TISSUES,” *Lancet*, vol. 257, no. 6656, pp. 655–657, Mar. 1951, doi: 10.1016/S0140-6736(51)92403-8.
- [31] A. Evans *et al.*, “Breast ultrasound: recommendations for information to women and referring physicians by the European Society of Breast Imaging,” *Insights Imaging*,

- vol. 9, no. 4, p. 449, Aug. 2018, doi: 10.1007/S13244-018-0636-Z.
- [32] R. M. Mann, N. Cho, and L. Moy, “Breast MRI: State of the Art,” *Radiology*, vol. 292, no. 3, pp. 520–536, 2019, doi: 10.1148/RADIOL.2019182947.
- [33] R. M. Mann, C. K. Kuhl, and L. Moy, “Contrast-enhanced MRI for breast cancer screening,” *J. Magn. Reson. Imaging*, vol. 50, no. 2, pp. 377–390, Aug. 2019, doi: 10.1002/JMRI.26654.
- [34] A. A. Bhatt, D. H. Whaley, and C. U. Lee, “Ultrasound-Guided Breast Biopsies: Basic and New Techniques,” *J. Ultrasound Med.*, vol. 40, no. 7, pp. 1427–1443, Jul. 2021, doi: 10.1002/JUM.15517.
- [35] V. S. Klimberg and A. Rivere, “Ultrasound image-guided core biopsy of the breast,” *Chinese Clin. Oncol.*, vol. 5, no. 3, 2016, doi: 10.21037/CCO.2016.04.05.
- [36] N. S. Winkler, “Ultrasound Guided Core Breast Biopsies,” *Tech. Vasc. Interv. Radiol.*, vol. 24, no. 3, Sep. 2021, doi: 10.1016/J.TVIR.2021.100776.
- [37] A. J. Lilly *et al.*, “MRI-guided core needle biopsy of the breast: Radiology-pathology correlation and impact on clinical management,” *Ann. Diagn. Pathol.*, vol. 48, Oct. 2020, doi: 10.1016/J.ANNDIAGPATH.2020.151563.
- [38] J. E. Kalinyak *et al.*, “PET-guided breast biopsy,” *Breast J.*, vol. 17, no. 2, pp. 143–151, Mar. 2011, doi: 10.1111/J.1524-4741.2010.01044.X.
- [39] D. Ha, V. Dialani, T. S. Menta, W. Keefe, E. Luanow, and P. J. Slanetz, “Mucocele-like lesions in the breast diagnosed with percutaneous biopsy: is surgical excision necessary?,” *AJR. Am. J. Roentgenol.*, vol. 204, no. 1, pp. 204–210, Jan. 2015, doi: 10.2214/AJR.13.11988.
- [40] M. Wang, X. He, Y. Chang, G. Sun, and L. Thabane, “A sensitivity and specificity comparison of fine needle aspiration cytology and core needle biopsy in evaluation of suspicious breast lesions: A systematic review and meta-analysis,” *Breast*, vol. 31, pp. 157–166, Feb. 2017, doi: 10.1016/J.BREAST.2016.11.009.
- [41] A. G. Waks and E. P. Winer, “Breast Cancer Treatment: A Review,” *JAMA - J. Am. Med. Assoc.*, vol. 321, no. 3, pp. 288–300, Jan. 2019, doi: 10.1001/jama.2018.19323.
- [42] S. Kalli, A. Semine, S. Cohen, S. P. Naber, S. S. Makim, and M. Bahl, “American joint committee on cancer’s staging system for breast cancer, eighth edition: What the radiologist needs to know,” *Radiographics*, vol. 38, no. 7, pp. 1921–1933, Nov. 2018, doi: 10.1148/RG.2018180056/ASSET/IMAGES/LARGE/RG.2018180056.FIG14G.JP EG.
- [43] A. Miller, B. Hoogstraten, M. Staquet, A. W.- cancer, and undefined 1981, “Reporting results of cancer treatment,” *Wiley Online Libr.*, Accessed: Mar. 14,

2022. [Online]. Available: [https://acsjournals.onlinelibrary.wiley.com/doi/abs/10.1002/1097-0142\(19810101\)47:1%3C207::AID-CNCR2820470134%3E3.0.CO;2-6](https://acsjournals.onlinelibrary.wiley.com/doi/abs/10.1002/1097-0142(19810101)47:1%3C207::AID-CNCR2820470134%3E3.0.CO;2-6).
- [44] E. A. Eisenhauer *et al.*, “New response evaluation criteria in solid tumours: Revised RECIST guideline (version 1.1),” doi: 10.1016/j.ejca.2008.10.026.
 - [45] K. N. Ogston *et al.*, “A new histological grading system to assess response of breast cancers to primary chemotherapy: prognostic significance and survival,” *Breast*, vol. 12, no. 5, pp. 320–327, 2003, doi: 10.1016/S0960-9776(03)00106-1.
 - [46] E. Hanafy, A. Al Jabri, G. Gadelkarim, A. Dasaq, F. Nazim, and M. Al Pakrah, “Tumor histopathological response to neoadjuvant chemotherapy in childhood solid malignancies: is it still impressive?,” *J. Investig. Med.*, vol. 66, no. 2, pp. 289–297, Feb. 2018, doi: 10.1136/JIM-2017-000531.
 - [47] H. Moghadas-Dastjerdi, H. R. Sha-E-Tallat, L. Sannachi, A. Sadeghi-Naini, and G. J. Czarnota, “A priori prediction of tumour response to neoadjuvant chemotherapy in breast cancer patients using quantitative CT and machine learning,” *Sci. Reports* 2020 101, vol. 10, no. 1, pp. 1–11, Jul. 2020, doi: 10.1038/s41598-020-67823-8.
 - [48] H. Tadayyon *et al.*, “A priori prediction of breast tumour response to chemotherapy using quantitative ultrasound imaging and artificial neural networks,” *Oncotarget*, vol. 10, no. 39, pp. 3910–3923, 2019, doi: 10.18632/ONCOTARGET.26996.
 - [49] B. Fisher *et al.*, “Effect of preoperative chemotherapy on the outcome of women with operable breast cancer,” *J. Clin. Oncol.*, vol. 16, no. 8, pp. 2672–2685, 1998, doi: 10.1200/JCO.1998.16.8.2672.
 - [50] S. J. Cleator, A. Makris, S. E. Ashley, R. Lal, and T. J. Powles, “Good clinical response of breast cancers to neoadjuvant chemoendocrine therapy is associated with improved overall survival,” *Ann. Oncol. Off. J. Eur. Soc. Med. Oncol.*, vol. 16, no. 2, pp. 267–272, 2005, doi: 10.1093/ANNONC/MDI049.
 - [51] A. Romero *et al.*, “Correlation between response to neoadjuvant chemotherapy and survival in locally advanced breast cancer patients,” *Ann. Oncol.*, vol. 24, no. 3, pp. 655–661, 2013, doi: 10.1093/annonc/mds493.
 - [52] L. M. Spring *et al.*, “Pathologic Complete Response after Neoadjuvant Chemotherapy and Impact on Breast Cancer Recurrence and Survival: A Comprehensive Meta-analysis,” *Clin. Cancer Res.*, vol. 26, no. 12, pp. 2838–2848, Jun. 2020, doi: 10.1158/1078-0432.CCR-19-3492.
 - [53] D. Sethi, R. Sen, S. Parshad, S. Khetarpal, M. Garg, and J. Sen, “Histopathologic changes following neoadjuvant chemotherapy in locally advanced breast cancer,” *Indian J. Cancer*, vol. 50, no. 1, pp. 58–64, 2013, doi: 10.4103/0019-509X.112301.
 - [54] S. Chuthapisith, J. M. Eremin, M. El-Sheemy, and O. Eremin, “Neoadjuvant

- chemotherapy in women with large and locally advanced breast cancer: chemoresistance and prediction of response to drug therapy,” *Surgeon*, vol. 4, no. 4, pp. 211–219, 2006, doi: 10.1016/S1479-666X(06)80062-4.
- [55] G. N. Hortobagyi, “Multidisciplinary management of advanced primary and metastatic breast cancer,” *Cancer*, vol. 74, no. 1 S, pp. 416–423, 1994, doi: 10.1002/cncr.2820741329.
 - [56] S. H. Giordano, “Update on locally advanced breast cancer,” *Oncologist*, vol. 8, no. 6, pp. 521–530, Dec. 2003, doi: 10.1634/THEONCOLOGIST.8-6-521.
 - [57] W. Haque, V. Verma, S. Hatch, V. Suzanne Klimberg, E. Brian Butler, and B. S. Teh, “Response rates and pathologic complete response by breast cancer molecular subtype following neoadjuvant chemotherapy,” *Breast Cancer Res. Treat.*, vol. 170, no. 3, pp. 559–567, Aug. 2018, doi: 10.1007/S10549-018-4801-3.
 - [58] T. Byrski *et al.*, “Pathologic complete response rates in young women with BRCA1-positive breast cancers after neoadjuvant chemotherapy,” *J. Clin. Oncol.*, vol. 28, no. 3, pp. 375–379, Jan. 2010, doi: 10.1200/JCO.2008.20.7019.
 - [59] J. L. Gennisson, T. Deffieux, M. Fink, and M. Tanter, “Ultrasound elastography: principles and techniques,” *Diagn. Interv. Imaging*, vol. 94, no. 5, pp. 487–495, 2013, doi: 10.1016/J.DIII.2013.01.022.
 - [60] L. D. Landau and E. M. Lifshitz, *Theory of elasticity, Volume 7 (Theoretical Physics)*. Butterworth-Heinemann, 1986.
 - [61] J. F. Greenleaf, M. Fatemi, and M. Insana, “Selected Methods for Imaging Elastic Properties of Biological Tissues,” *Annu. Rev. Biomed. Eng.*, vol. 5, no. 1, pp. 57–78, Aug. 2003, doi: 10.1146/annurev.bioeng.5.040202.121623.
 - [62] Fung, *Biomechanics: Mechanical Properties of Living Tissues, Second Edition*: 1993.
 - [63] J. Ophir *et al.*, “Elastography: Ultrasonic estimation and imaging of the elastic properties of tissues,” *Proc. Inst. Mech. Eng. Part H J. Eng. Med.*, vol. 213, no. 3, pp. 203–233, Mar. 1999, doi: 10.1243/0954411991534933.
 - [64] T. Shiina *et al.*, “WFUMB guidelines and recommendations for clinical use of ultrasound elastography: Part 1: basic principles and terminology,” *Ultrasound Med. Biol.*, vol. 41, no. 5, pp. 1126–1147, May 2015, doi: 10.1016/J.ULTRASMEDBIO.2015.03.009.
 - [65] A. P. Sarvazyan, O. V. Rudenko, S. D. Swanson, J. B. Fowlkes, and S. Y. Emelianov, “Shear wave elasticity imaging: a new ultrasonic technology of medical diagnostics,” *Ultrasound Med. Biol.*, vol. 24, no. 9, pp. 1419–1435, Dec. 1998, doi: 10.1016/S0301-5629(98)00110-0.

- [66] G. S. Gherlan, "Liver ultrasound elastography: More than staging the disease," *World Journal of Hepatology*, vol. 7, no. 12. Baishideng Publishing Group Co, pp. 1595–1600, 2015, doi: 10.4254/wjh.v7.i12.1595.
- [67] M. A. Lubinski, S. Y. Emelianov, and M. O'Donnell, "Speckle tracking methods for ultrasonic elasticity imaging using short-time correlation," *IEEE Trans. Ultrason. Ferroelectr. Freq. Control*, vol. 46, no. 1, pp. 82–96, Jan. 1999, doi: 10.1109/58.741427.
- [68] A. R. Skovoroda, S. Y. Emelianov, M. A. Lubinski, A. P. Sarvazyan, and M. O'Donnell, "Theoretical analysis and verification of ultrasound displacement and strain imaging," *IEEE Trans. Ultrason. Ferroelectr. Freq. Control*, vol. 41, no. 3, pp. 302–313, May 1994, doi: 10.1109/58.285463.
- [69] T. Varghese, "Quasi-Static Ultrasound Elastography," *Ultrasound Clinics*, vol. 4, no. 3. NIH Public Access, pp. 323–338, Jul. 2009, doi: 10.1016/j.cult.2009.10.009.
- [70] J. A. Jensen and P. Munk, "A new method for estimation of velocity vectors," *IEEE Trans. Ultrason. Ferroelectr. Freq. Control*, vol. 45, no. 3, pp. 837–851, 1998, doi: 10.1109/58.677749.
- [71] M. E. Anderson, "Multi-dimensional velocity estimation with ultrasound using spatial quadrature," *IEEE Trans. Ultrason. Ferroelectr. Freq. Control*, vol. 45, no. 3, pp. 852–861, 1998, doi: 10.1109/58.677757.
- [72] U. Techavipoo, Q. Chen, T. Varghese, and J. A. Zagzebski, "Estimation of displacement vectors and strain tensors in elastography using angular insonifications," *IEEE Trans. Med. Imaging*, vol. 23, no. 12, pp. 1479–1489, Dec. 2004, doi: 10.1109/TMI.2004.835604.
- [73] H. Rivaz, E. M. Boctor, M. A. Choti, and G. D. Hager, "Real-time regularized ultrasound elastography," *IEEE Trans. Med. Imaging*, vol. 30, no. 4, pp. 928–945, 2011, doi: 10.1109/TMI.2010.2091966.
- [74] H. S. Hashemi and H. Rivaz, "Global Time-Delay Estimation in Ultrasound Elastography," *IEEE Trans. Ultrason. Ferroelectr. Freq. Control*, vol. 64, no. 10, pp. 1625–1636, 2017, doi: 10.1109/TUFFC.2017.2717933.
- [75] M. Mirzaei, A. Asif, and H. Rivaz, "Combining Total Variation Regularization with Window-Based Time Delay Estimation in Ultrasound Elastography," *IEEE Trans. Med. Imaging*, vol. 38, no. 12, pp. 2744–2754, Dec. 2019, doi: 10.1109/TMI.2019.2913194.
- [76] M. Ashikuzzaman, C. J. Gauthier, and H. Rivaz, "Global ultrasound elastography in spatial and temporal domains," *IEEE Trans. Ultrason. Ferroelectr. Freq. Control*, vol. 66, no. 5, pp. 876–887, May 2019, doi: 10.1109/TUFFC.2019.2903311.
- [77] M. G. Kibria and H. Rivaz, "GLUENet: Ultrasound elastography using

- convolutional neural network,” *Lect. Notes Comput. Sci. (including Subser. Lect. Notes Artif. Intell. Lect. Notes Bioinformatics)*, vol. 11042 LNCS, pp. 21–28, 2018, doi: 10.1007/978-3-030-01045-4_3.
- [78] I. Céspedes, J. Ophir, and M. Insana, “Theoretical Bounds on Strain Estimation in Elastography,” *IEEE Trans. Ultrason. Ferroelectr. Freq. Control*, vol. 42, no. 5, pp. 969–971, 1995, doi: 10.1109/58.464850.
 - [79] W. F. Walker and G. E. Trahey, “A Fundamental Limit on Delay Estimation Using Partially Correlated Speckle Signals,” *IEEE Trans. Ultrason. Ferroelectr. Freq. Control*, vol. 42, no. 2, pp. 301–308, 1995, doi: 10.1109/58.365243.
 - [80] Y. Zhu and T. J. Hall, “A modified block matching method for real-time freehand strain imaging,” *Ultrason. Imaging*, vol. 24, no. 3, pp. 161–176, 2002, doi: 10.1177/016173460202400303.
 - [81] A. M, S.-N. A, S. A, and R. H, “Combining First- and Second-Order Continuity Constraints in Ultrasound Elastography,” *IEEE Trans. Ultrason. Ferroelectr. Freq. Control*, vol. 68, no. 7, pp. 2407–2418, Jul. 2021, doi: 10.1109/TUFFC.2021.3065884.
 - [82] A. Sarvazyan, T. J. Hall, M. W. Urban, M. Fatemi, S. R. Aglyamov, and B. S. Garra, “An Overview of Elastography-An Emerging Branch of Medical Imaging,” *Curr. Med. Imaging Rev.*, vol. 7, no. 4, pp. 255–282, Nov. 2011, doi: 10.2174/157340511798038684.
 - [83] H. Karimi, A. Fenster, and A. Samani, “A novel fast full inversion based breast ultrasound elastography technique,” *Phys. Med. Biol.*, vol. 58, no. 7, pp. 2219–2233, Apr. 2013, doi: 10.1088/0031-9155/58/7/2219.
 - [84] D. T. Seidl, A. A. Oberai, and P. E. Barbone, “The Coupled Adjoint-State Equation in forward and inverse linear elasticity: Incompressible plane stress,” *Comput. Methods Appl. Mech. Eng.*, vol. 357, Dec. 2019, doi: 10.1016/j.cma.2019.112588.
 - [85] H. Mehrabian and A. Samani, “An iterative hyperelastic parameters reconstruction for breast cancer assessment,” *Med. Imaging 2008 Physiol. Funct. Struct. from Med. Images*, vol. 6916, no. March 2008, p. 69161C, 2008, doi: 10.1117/12.770971.
 - [86] S. R. Mousavi, H. Rivaz, A. Sadeghi-Naini, G. J. Czarnota, and A. Samani, “Breast Ultrasound Elastography Using Full Inversion-Based Elastic Modulus Reconstruction,” *IEEE Trans. Comput. Imaging*, vol. 3, no. 4, pp. 774–782, 2017, doi: 10.1109/tci.2017.2741422.
 - [87] P. S. Wellman, E. P. Dalton, D. Krag, K. A. Kern, and R. D. Howe, “Tactile Imaging of Breast Masses: First Clinical Report,” *Arch. Surg.*, vol. 136, no. 2, pp. 204–208, Feb. 2001, doi: 10.1001/ARCHSURG.136.2.204.
 - [88] H. T. Liu, L. Z. Sun, G. Wang, and M. W. Vannier, “Analytic modeling of breast

- elastography,” *Med. Phys.*, vol. 30, no. 9, pp. 2340–2349, Sep. 2003, doi: 10.1118/1.1599953.
- [89] T. Hu and J. P. Desai, “Characterization of Soft-Tissue Material Properties: Large Deformation Analysis,” *Lect. Notes Comput. Sci. (including Subser. Lect. Notes Artif. Intell. Lect. Notes Bioinformatics)*, vol. 3078, pp. 28–37, 2004, doi: 10.1007/978-3-540-25968-8_4.
- [90] J. (1842-1929). A. du texte Boussinesq, “Application des potentiels à l’étude de l’équilibre et du mouvement des solides élastiques, principalement au calcul des déformations et des pressions que produisent, dans les solides, des efforts quelconques exercés sur une petite partie de leur surface ou de leur intérieur : mémoire suivi de notes étendues sur divers points de physique mathématique et d’analyse / par J. Boussinesq,...,” 1885, Accessed: Mar. 08, 2021. [Online]. Available: <https://gallica.bnf.fr/ark:/12148/bpt6k9651115r>.
- [91] Y. Gordon *et al.*, “Dynamic contrast-enhanced magnetic resonance imaging: fundamentals and application to the evaluation of the peripheral perfusion,” *Cardiovasc. Diagn. Ther.*, vol. 4, no. 2, p. 147, 2014, doi: 10.3978/J.ISSN.2223-3652.2014.03.01.
- [92] J. Xiao *et al.*, “Dynamic contrast-enhanced breast MRI features correlate with invasive breast cancer angiogenesis,” *npj Breast Cancer* 2021 71, vol. 7, no. 1, pp. 1–9, Apr. 2021, doi: 10.1038/s41523-021-00247-3.
- [93] R. Johansen *et al.*, “Predicting survival and early clinical response to primary chemotherapy for patients with locally advanced breast cancer using DCE-MRI,” *J. Magn. Reson. Imaging*, vol. 29, no. 6, pp. 1300–1307, Jun. 2009, doi: 10.1002/jmri.21778.
- [94] R. G. Abramson *et al.*, “Early assessment of breast cancer response to neoadjuvant chemotherapy by semi-quantitative analysis of high-temporal resolution DCE-MRI: Preliminary results,” *Magn. Reson. Imaging*, vol. 31, no. 9, pp. 1457–1464, Nov. 2013, doi: 10.1016/j.mri.2013.07.002.
- [95] N. S. Gezer, O. Orbay, P. Balci, M. G. Durak, B. Demirkhan, and S. Saydam, “Evaluation of Neoadjuvant Chemotherapy Response with Dynamic Contrast Enhanced Breast Magnetic Resonance Imaging in Locally Advanced Invasive Breast Cancer,” *J. Breast Heal.*, vol. 10, no. 2, pp. 111–118, May 2014, doi: 10.5152/TJBH.2014.2035.
- [96] E. A. Eisenhauer *et al.*, “New response evaluation criteria in solid tumours: revised RECIST guideline (version 1.1),” *Eur. J. Cancer*, vol. 45, no. 2, pp. 228–247, Jan. 2009, doi: 10.1016/J.EJCA.2008.10.026.
- [97] J. R. Teruel *et al.*, “Dynamic contrast-enhanced MRI texture analysis for pretreatment prediction of clinical and pathological response to neoadjuvant chemotherapy in patients with locally advanced breast cancer,” *NMR Biomed.*, vol.

- 27, no. 8, pp. 887–896, 2014, doi: 10.1002/NBM.3132.
- [98] J. Wu, G. Gong, Y. Cui, and R. Li, “Intratumor partitioning and texture analysis of dynamic contrast-enhanced (DCE)-MRI identifies relevant tumor subregions to predict pathological response of breast cancer to neoadjuvant chemotherapy,” *J. Magn. Reson. Imaging*, vol. 44, no. 5, pp. 1107–1115, Nov. 2016, doi: 10.1002/jmri.25279.
- [99] A. Sharma, S. Sharma, S. Sood, R. K. Seam, M. Sharma, and V. Fotedar, “DCE-MRI and parametric imaging in monitoring response to neoadjuvant chemotherapy in breast carcinoma: a preliminary report,” *Polish J. Radiol.*, vol. 83, p. e220, 2018, doi: 10.5114/PJR.2018.76271.
- [100] W. P. Andrade *et al.*, “Can FDG-PET/CT predict early response to neoadjuvant chemotherapy in breast cancer?,” *Eur. J. Surg. Oncol.*, vol. 39, no. 12, pp. 1358–1363, Dec. 2013, doi: 10.1016/j.ejso.2013.08.025.
- [101] W. F. Symmans *et al.*, “Measurement of residual breast cancer burden to predict survival after neoadjuvant chemotherapy,” *J. Clin. Oncol.*, vol. 25, no. 28, pp. 4414–4422, Oct. 2007, doi: 10.1200/JCO.2007.10.6823.
- [102] B. S. Pio *et al.*, “Usefulness of 3’-[F-18]fluoro-3’-deoxythymidine with positron emission tomography in predicting breast cancer response to therapy,” *Mol. imaging Biol.*, vol. 8, no. 1, pp. 36–42, Jan. 2006, doi: 10.1007/S11307-005-0029-9.
- [103] R. Barkmann, “Quantitative ultrasound,” *Grampp S. Radiol. Osteoporosis. Med. Radiol. (Diagnostic Imaging)*, pp. 412–474, Apr. 2016, doi: 10.1007/978-3-540-68604-0_11.
- [104] H. Tadayyon *et al.*, “Quantitative ultrasound assessment of breast tumor response to chemotherapy using a multi-parameter approach,” *Oncotarget*, vol. 7, no. 29, pp. 45094–45111, 2016, doi: 10.18632/ONCOTARGET.8862.
- [105] H. Tadayyon, A. Sadeghi-Naini, L. Wirtzfeld, F. C. Wright, and G. Czarnota, “Quantitative ultrasound characterization of locally advanced breast cancer by estimation of its scatterer properties,” *Med. Phys.*, vol. 41, no. 1, p. 012903, Jan. 2014, doi: 10.1118/1.4852875.
- [106] Z. Klimonda, P. Karwat, K. Dobruch-Sobczak, H. Piotrzkowska-Wróblewska, and J. Litniewski, “Breast-lesions characterization using Quantitative Ultrasound features of peritumoral tissue,” *Sci. Rep.*, vol. 9, no. 1, pp. 1–9, Dec. 2019, doi: 10.1038/s41598-019-44376-z.
- [107] A. Sadeghi-Naini *et al.*, “Chemotherapy-Response Monitoring of Breast Cancer Patients Using Quantitative Ultrasound-Based Intra-Tumour Heterogeneities,” *Sci. Rep.*, vol. 7, no. 1, Dec. 2017, doi: 10.1038/S41598-017-09678-0.
- [108] L. Sannachi *et al.*, “Breast Cancer Treatment Response Monitoring Using

- Quantitative Ultrasound and Texture Analysis: Comparative Analysis of Analytical Models,” *Transl. Oncol.*, vol. 12, no. 10, pp. 1271–1281, Oct. 2019, doi: 10.1016/j.tranon.2019.06.004.
- [109] K. Quiaoit *et al.*, “Quantitative ultrasound radiomics for therapy response monitoring in patients with locally advanced breast cancer: Multi-institutional study results,” *PLoS One*, vol. 15, no. 7, p. e0236182, Jul. 2020, doi: 10.1371/journal.pone.0236182.
 - [110] F. L. Lizzi, M. Ostromogilsky, E. J. Feleppa, M. C. Rorke, and M. M. Yaremko, “Relationship of ultrasonic spectral parameters to features of tissue microstructure,” *IEEE Trans. Ultrason. Ferroelectr. Freq. Control*, vol. 34, no. 3, pp. 319–329, 1987, doi: 10.1109/TUFFC.1987.26950.
 - [111] A. Sadeghi-Naini *et al.*, “Conventional frequency ultrasonic biomarkers of cancer treatment response *in vivo*,” *Transl. Oncol.*, vol. 6, no. 3, pp. 234–243, 2013, doi: 10.1593/TLO.12385.
 - [112] G. J. Czarnota *et al.*, “Tumor radiation response enhancement by acoustical stimulation of the vasculature,” *Proc. Natl. Acad. Sci. U. S. A.*, vol. 109, no. 30, Jul. 2012, doi: 10.1073/PNAS.1200053109.
 - [113] R. M. Vlad, S. Brand, A. Giles, M. C. Kolios, and G. J. Czarnota, “Quantitative ultrasound characterization of responses to radiotherapy in cancer mouse models,” *Clin. Cancer Res.*, vol. 15, no. 6, pp. 2067–2075, Mar. 2009, doi: 10.1158/1078-0432.CCR-08-1970.
 - [114] B. Banihashemi, R. Vlad, B. Debeljevic, A. Giles, M. C. Kolios, and G. J. Czarnota, “Ultrasound imaging of apoptosis in tumor response: novel preclinical monitoring of photodynamic therapy effects,” *Cancer Res.*, vol. 68, no. 20, pp. 8590–8596, Oct. 2008, doi: 10.1158/0008-5472.CAN-08-0006.
 - [115] O. Falou *et al.*, “Evaluation of neoadjuvant chemotherapy response in women with locally advanced breast cancer using ultrasound elastography,” *Transl. Oncol.*, vol. 6, no. 1, pp. 17–24, 2013, doi: 10.1593/tlo.12412.
 - [116] J. Gu *et al.*, “Early assessment of shear wave elastography parameters foresees the response to neoadjuvant chemotherapy in patients with invasive breast cancer,” *Breast Cancer Res.*, vol. 23, no. 1, pp. 1–13, Dec. 2021, doi: 10.1186/S13058-021-01429-4/TABLES/3.
 - [117] M. K. Jena and J. Janjanam, “Role of extracellular matrix in breast cancer development: a brief update,” *F1000Research*, vol. 7, 2018, doi: 10.12688/F1000RESEARCH.14133.2.
 - [118] C. Walker, E. Mojares, and A. Del Río Hernández, “Role of Extracellular Matrix in Development and Cancer Progression,” *Int. J. Mol. Sci.*, vol. 19, no. 10, 2018, doi: 10.3390/IJMS19103028.

- [119] S. Xu *et al.*, “The role of collagen in cancer: from bench to bedside,” *J. Transl. Med.* 2019 171, vol. 17, no. 1, pp. 1–22, Sep. 2019, doi: 10.1186/S12967-019-2058-1.
- [120] J. Winkler, A. Abisoye-Ogunniyan, K. J. Metcalf, and Z. Werb, “Concepts of extracellular matrix remodelling in tumour progression and metastasis,” *Nat. Commun.* 2020 111, vol. 11, no. 1, pp. 1–19, Oct. 2020, doi: 10.1038/s41467-020-18794-x.
- [121] T. Armstrong *et al.*, “Type I collagen promotes the malignant phenotype of pancreatic ductal adenocarcinoma,” *Clin. Cancer Res.*, vol. 10, no. 21, pp. 7427–7437, Nov. 2004, doi: 10.1158/1078-0432.CCR-03-0825.
- [122] J. W. Wang *et al.*, “Ultrasound elastography as an imaging biomarker for detection of early tumor response to chemotherapy in a murine breast cancer model: a feasibility study,” *Br. J. Radiol.*, vol. 91, no. 1085, 2018, doi: 10.1259/BJR.20170698.
- [123] J. Fernandes *et al.*, “Monitoring Breast Cancer Response to Neoadjuvant Chemotherapy Using Ultrasound Strain Elastography,” *Transl. Oncol.*, vol. 12, no. 9, p. 1177, Sep. 2019, doi: 10.1016/J.TRANON.2019.05.004.

Chapter 2

2 A Novel Tissue Mechanics-based Method for Improving Tissue Displacement and Strain Estimation in Breast Ultrasound Elastography

A version of this chapter has been submitted as a journal paper for publication in Medical Physics.

2.1 Introduction

Breast cancer is the second most diagnosed cancer in women, estimated to affect 1 in 8 Canadian women during their lifetime. It was estimated that in 2021, 27,700 women will die from breast cancer in the United States [1]. Vital to successful treatment of the patient, early detection achieved through regular breast cancer screening has shown to reduce mortality by 25% in the first 10 years where treating stage 1 cancer has the highest survival rate [2], [3]. The most common medical imaging technique used for breast cancer screening is X-ray mammography. However, due to ionizing radiation, the frequency of testing using this method is constrained, potentially delaying critically needed early diagnosis. Another concern of this screening method is that it is influenced by breast density and hormone replacement therapy, hence impacting its sensitivity for breast cancer detection, especially with young women with dense breasts where reported sensitivities are as low as ~60% [4], [5].

When X-ray mammograms are inconclusive, B-mode ultrasound (US) imaging and magnetic resonance imaging (MRI) are used. While the B-mode US is widely available and inexpensive, image quality is a limiting factor that impacts its sensitivity and specificity. Being highly sensitive, MRI is very effective for abnormality detection. However, its high cost and limited availability have ruled out its routine utility for early detection. As such, different investigations have been actively conducted to develop affordable imaging techniques with high sensitivity and specificity. One promising option towards this goal is elastography [6]–[8] where maps of tissue stiffness are generated and visualized. In the context of breast cancer, this is motivated by the fact that many types of cancer, including ductal carcinoma which is the most common type of breast cancer, are

associated with biological changes that lead to tissue stiffening [9]–[12]. As such, breast tissue stiffening may be evaluated for breast cancer detection. Among elastography techniques, quasi-static ultrasound elastography (USE) has been shown to be effective in stiffness imaging for a wide range of oncology applications, including breast, prostate and liver cancers [13]–[18]. Benefits of USE include involvement of the non-invasive low-cost ultrasound (US) imaging, being free of harmful radiation, fast data acquisition and image reconstruction.

In quasi-static elastography, a low-frequency external loading is applied for tissue mechanical stimulation by pressing the US probe against the breast. US radiofrequency (RF) data is then acquired during tissue compression whereby an RF data frame is collected at each time instant of compression. Using two RF data frames corresponding to two compression states, the tissue displacement data can be estimated [6], [19]–[21]. The tissue strain image calculated by differentiating the displacement field is considered the simplest form of elastography which is often integrated into US systems for real-time imaging [6]. Assuming tissue stress uniformity, strain images generated through this method can be regarded as an approximation to tissue stiffness maps (e.g., hard lesions appear as low strain areas).

While strain imaging has been shown to be useful for some clinical applications [22], due to the weakness of the stress uniformity assumption, its accuracy is limited. As such, more advanced techniques have been developed to image more reliable measures of tissue stiffness (e.g. Young's modulus) using the measured displacement field [22].

In both strain imaging and Young's modulus imaging, the primary determining factor of accuracy is the accuracy of the tissue displacement data consisting of axial and lateral displacement fields. Young's modulus image reconstruction involves an ill-posed inverse problem. This ill-posedness issue can be mitigated if reliable estimates of both axial and lateral displacement components are available. Several methods exist to estimate axial and lateral displacements using US RF data; however, the low signal-to-noise (SNR) ratio and the 2D nature of conventional US imaging have limited the accuracy of estimated displacements, especially the lateral displacement component. This has encouraged efforts

toward the development of more robust methods for displacement estimation. Estimation of tissue displacement and strain distribution in USE can be considered as an optical flow (OF) problem which involves minimization of an energy equation imposing both echo amplitude conservation and displacement smoothness constraints [23]–[27]. More recently, deep learning methods were proposed for displacement and strain estimation which proved promising while further improvement is necessary [28]–[30]. Other algorithms mostly focus on time delay estimation (TDE) methods [19], [30]–[37] where the TDE can be obtained for small windows of RF data. TDE involves a search which can be performed in either 1D or 2D corresponding to search in the axial direction only or in both lateral and axial directions, respectively [36], [37]. While they generally provide accurate estimate in the axial direction, these approaches are too sensitive to signal decorrelation which often occurs in clinical breast imaging. Another effective approach followed to develop a robust method against signal decorrelation involves optimization constrained by regularization which imposes smoothness of tissue deformation [31], [32]. In this approach, the displacement is estimated along a single RF-line, leading to displacement discontinuity between adjacent RF-lines and low accuracy of the lateral displacement field [31]. To avoid this, the displacement estimation can be performed simultaneously for all RF lines [32]. This method leads to excessively smooth displacement field, hence blurry strain images. To address this issue, a window-based term in conjunction with first or second order derivative-based regularization were employed in other relevant works considered the state-of-the-art methods in this field [33], [38]. A number of other studies have investigated utilizing more than two RF frames to estimate the displacement fields [34], [39]–[42]. A downside of these methods is lack of systematic way to determine the weighting coefficients. In another category of displacement estimation methods, known as quality-guided motion tracking [43]–[47], the displacement is first estimated for the points in high correlation local region. Subsequently, a displacement continuity constraint is used to estimate the displacements of the points in low correlation local regions based on the previously estimated displacements of points in high correlation regions. In addition to being computationally more efficient, this quality-guided motion tracking method has shown to operate well in regions with poorly correlated RF data and also geometrically irregular regions [45].

While existing tissue motion tracking methods can produce reasonably accurate axial displacement maps, the accuracy of their lateral displacements are generally low. At their core, these techniques rely on regularization through imposing tissue continuity and various field smoothness criteria. Utilizing tissue mechanics constraints such as incompressibility, compatibility and tissue 3D deformation models have not been as rigorously investigated for formulating more effective regularization to find more accurate 2D displacement fields. As an attempt to incorporate such constraints towards improved displacement estimation, approximate tissue mechanics-based relations founded on the stress uniformity assumption were derived and incorporated in an algorithm that uses three US RF frames [39]. Efforts have been also made to utilize the partial differential equations governing the linear elastic deformation in soft tissue. This includes a method proposed to estimate tissue lateral displacement field using measured axial displacement field based on tissue incompressibility condition [48]. The method assumes plane strain conditions and it was shown that the estimated lateral displacement field was more accurate and had higher SNR compared with a field estimated using traditional speckle tracking. The method was then extended to account for large deformation conditions under plane strain assumption [49]. Also, through assuming plane strain conditions, a nearly incompressible constraint was used as a regularization term in a pixel-wise model-based algorithm to estimate all components of vascular strain (axial, lateral and shear) with a high spatial resolution [50]. Incompressibility constraint has also been used in other methods by incorporating confidence weights for different tissue regions, momentum conservation equation in conjunction with a robust H_{∞} filter [51], [52]. More recently, a mathematical framework was developed to improve an estimate of tissue axial and lateral displacement fields while the shear modulus was also reconstructed simultaneously [53]. The framework assumes plane stress conditions and tissue incompressibility while it does not require traction or displacement boundary conditions.

In this chapter, we introduce a novel algorithm that uses an estimation of out-of-plane strain to improve the in-plane tissue displacement and strain fields, especially their lateral component. Unlike previous studies, the proposed method neither assumes plane strain nor plane stress conditions and instead is founded on tissue mechanics principles of incompressibility and compatibility. To enforce tissue incompressibility, in contrast to

using the plane strain or plane stress assumptions, we use Boussinesq's equation to analytically estimate the out-of-plane strain.

2.2 Materials and Methods

2.2.1 Overview of Strain Refinement Algorithm (STREAL)

The proposed algorithm requires an initial estimate of the displacements to be processed before an improved estimate is generated. To obtain an initial estimate of the tissue axial and lateral displacement fields, we process a suitable pair of acquired RF data frames using publicly available computer programs developed based on the Global Ultrasound Elastography (GLUE) method [31], [32]. These fields are then refined step-by-step by first smoothing and then enforcing the fundamental tissue mechanics conditions of incompressibility and compatibility. Smoothing and incompressibility condition enforcement leads to improved displacement fields estimate while the compatibility condition enforcement applies further improvement, leading to the final strain fields. A flowchart of STREAL is illustrated in Figure 2-1.

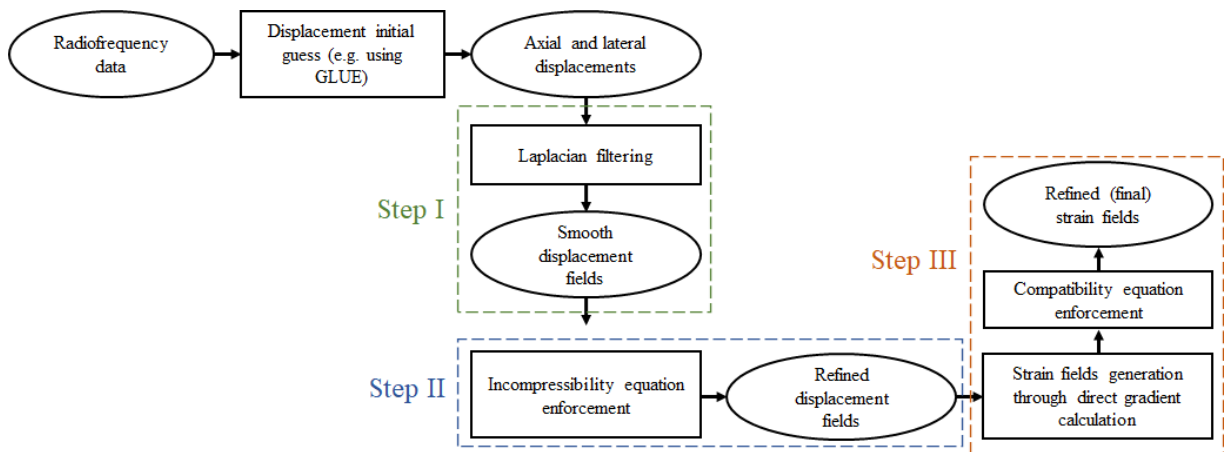


Figure 2-1. Strain Refinement Algorithm (STREAL) flowchart

1) Step 1: Second Order Derivative Based Regularization

To further regularize the initial displacement data where first order derivative-based regularization is already applied, we use regularization which seeks a new estimate of the

displacement field where the 2D Laplacian of the displacement components throughout the field of view (FOV) is minimized. The 2D-Laplacian of the displacement field U is expressed mathematically by:

$$\nabla U(x, y) = \partial^2 U(x, y)/\partial x^2 + \partial^2 U(x, y)/\partial y^2 \quad (2-1)$$

This operator can be expressed in a matrix form by applying the finite difference approximation of this operator to each point in the FOV, leading to the following matrix form:

$$\nabla U(x, y) = LU \quad (2-2)$$

where L is a matrix with entries of the finite difference coefficients and U is a 1D vector containing both axial and lateral displacement fields. The entries of L are arranged such that each row of Equation (2-2) yields the finite difference approximation of the Laplacian operator at each point. The solution sought in this step is one that minimizes the Laplacian while it matches the input displacements obtained from the previous step (U_m) as much as possible. This leads to the following minimization equation of Tikhonov regularization:

$$\text{Min. } (\|U - U_m\|^2 + \lambda^2 \|LU\|^2) \quad (2-3)$$

where $\|\cdot\|$ represents the Eulerian norm and λ^2 represents a positive weight coefficient. This minimization leads to the following least squares solution:

$$U_{new} = (I + \lambda^2 L^T L)^{-1} U_m \quad (2-4)$$

The regularization weight coefficient, λ , determines the level of smoothness. This coefficient is found automatically using the L-curve technique [54] where a solution U is found for various λ values before $\|LU\|$ is plotted against $\|U - U_m\|$. Typically, this plot resembles an L-curve, and the knee point of this curve corresponds to a λ value that is considered optimal as it corresponds to the best trade-off between smoothness and original data matching (Figure 2-2).

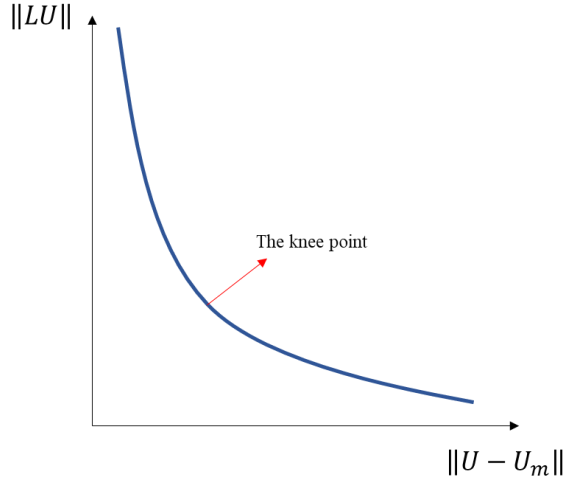


Figure 2-2. The L-curve plot and its knee point which corresponds to an optimal λ value.

2) Step 2: Tissue Incompressibility Enforcement

Tissue incompressibility is expressed mathematically by setting the divergence of the displacement field in 3D to zero as follows:

$$\nabla \cdot U(x, y, z) = \partial u_x / \partial x + \partial u_y / \partial y + \partial u_z / \partial z = 0 \quad (2-5)$$

where in the context of US image coordinate system, x , y , and z correspond to lateral, axial, and out-of-plane directions, respectively as shown in Figure 2-2. Since conventional US data does not provide information on out-of-plane displacements, assumptions such as plane-strain and plane-stress have been used as discussed in the introduction. Assuming plane-strain conditions, in which the out-of-plane strain is zero, the incompressibility condition leads to the following equation:

$$\partial u_x / \partial x + \partial u_y / \partial y = 0 \quad (2-6)$$

The plane strain assumption considered in previous works, however, is not valid in breast USE as it requires constant section geometry and loading of tissue along the z direction [53]. As an alternative, other works assumed plane stress condition which requires very thin tissue geometry undergoing in-plane loading only [48]. Neither of these requirements are met in the context of breast USE. To assess the deviation of the plane strain and plane stress assumptions from actual 3D situations, we conducted an *in silico* experiment of

breast USE using ABAQUS FE solver (ABAQUS 2019, Dassault Systèmes Simulia Corp., Johnston, RI, USA). In this experiment a typical breast geometry derived from a breast MR image was converted into a homogeneous hyperelastic breast FE model with hyperelastic parameters assigned based on values reported in the literature [55]. This model was virtually compressed by an US probe to simulate a typical USE procedure. The simulation was conducted using 3D geometry and loading as the ground truth model while 2D plane strain and plane stress conditions were also simulated to evaluate their deviation from the “true” 3D model. For this evaluation, the ratio of the mean difference between the “true” and 2D displacement fields to the mean value of the “true” field was calculated for both axial and lateral displacement components. For the plane strain case, this led to values of 0.84 and 4.73 for the axial and lateral components, respectively. For the plane stress case, the ratio values were 0.79 and 2.87, respectively. While this experiment, which involves a single breast, is not rigorous, the obtained large values, especially the ones pertaining to the plane strain assumption are sufficient to motivate developing a modified incompressibility equation that can be used more reliably in breast USE.

In this study, we estimate the out-of-plane strain considering the breast undergoing a US probe loading as a semi-infinite medium. A semi-infinite solid is an idealized body with a single planar surface that extends in all directions to infinity. In 1885, Boussinesq developed equations for determining stresses at any point (T) in an elastic, semi-infinite, homogeneous, and isotropic solid medium as a result of a surface concentrated point load (P) [56]. Considering the dimensions of ultrasound probe with respect to the dimensions of breast in supine position, breast can be considered as a semi-infinite medium, thus, axial and out-of-plane stresses can be calculated using Equations (2-7), (2-8), and (2-9) which represent Boussinesq stress equations. As shown in Figure 2-3, in these equations, (x_0, y_0, z_0) and (x, y, z) are the coordinates of points T and P , respectively, while r is the Euclidean distance between them. It is noteworthy that while the calculated stresses using Boussinesq stress equations are local due to the assumption of concentrated point load, in our case, the stresses are calculated based on an integration over the surface of ultrasound probe, hence they do not remain local.

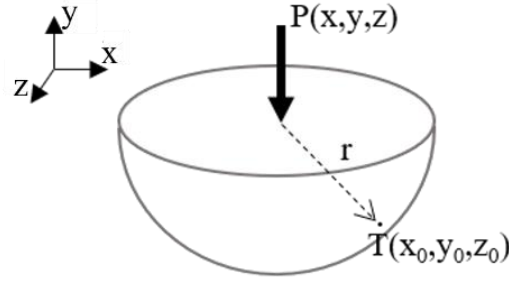


Figure 2-3: Boussinesq's model - a schematic of a semi-infinite medium under a point load

$$\sigma_{xx} = \frac{P}{2\pi} \left\{ \frac{3(y_0-y)(x_0-x)^2}{r^5} - (1-2\nu) \left[\frac{(x_0-x)^2-(z_0-z)^2}{r(r^2-(y_0-y)^2)(r+(y_0-y))} - \frac{(z_0-z)^2(y_0-y)}{r^3(r^2-(y_0-y)^2)} \right] \right\} \quad (2-7)$$

$$\sigma_{yy} = \frac{3P}{2\pi} \frac{(y_0-y)^3}{r^5} \quad (2-8)$$

$$\sigma_{zz} = \frac{P}{2\pi} \left\{ \frac{3(y_0-y)(z_0-z)^2}{r^5} - (1-2\nu) \left[\frac{(z_0-z)^2-(x_0-x)^2}{r(r^2-(y_0-y)^2)(r+(y_0-y))} - \frac{(x_0-x)^2(y_0-y)}{r^3(r^2-(y_0-y)^2)} \right] \right\} \quad (2-9)$$

Assuming a uniformly distributed loading applied by the US probe on the surface of the breast, axial and out-of-plane stresses at every point in the US FOV (Figure 2-4a) can be calculated by integration of Equations (2-7), (2-8), and (2-9) on the surface of the applied load. Thus, using Hooke's law, the axial and out-of-plane strains can be calculated as given in Equation (2-10).

$$\begin{bmatrix} \varepsilon_{yy} \\ \varepsilon_{zz} \end{bmatrix} = \begin{bmatrix} \frac{\lambda}{2\mu(3\lambda+2\mu)} & \frac{\lambda+\mu}{\mu(3\lambda+2\mu)} & \frac{-\lambda}{2\mu(3\lambda+2\mu)} \\ \frac{\lambda}{2\mu(3\lambda+2\mu)} & \frac{\lambda}{2\mu(3\lambda+2\mu)} & \frac{\lambda+\mu}{\mu(3\lambda+2\mu)} \end{bmatrix} \begin{bmatrix} \sigma_{xx} \\ \sigma_{yy} \\ \sigma_{zz} \end{bmatrix} \quad (2-10)$$

Where μ and λ are Lame' parameters.

In this work, we assume that the breast is linear elastic with a Young's modulus, E , value of 3kPa [57] and Poisson's ratio of 0.495. The Poisson's ratio value is consistent with the high-water content composition of most soft tissue, including breast tissue. While some intra- and inter-patient variability is expected, our simulation indicates that modest variability does not impact estimated displacement fields significantly. The Lame' parameters can be calculated using the following equation.

$$\lambda = \frac{Ev}{(1+\nu)(1-2\nu)}, \mu = \frac{E}{2(1+\nu)} \quad (2-11)$$

Thereafter, the ratio ($k = \frac{\partial u_z}{\partial z} / \frac{\partial u_y}{\partial y} = \frac{\varepsilon_{zz}}{\varepsilon_{yy}}$) of the out-of-plane to axial strain can be calculated, leading to the following modified incompressibility equation.

$$\partial u_x / \partial x + (k + 1) \partial u_y / \partial y = 0 \quad (2-12)$$

The finite difference form of Boussinesq's equations can be rewritten in a matrix form as follows:

$$CU = 0 \quad (2-13)$$

Here, U contains the lateral and axial displacements only, and C is a matrix containing coefficients of the finite difference approximation of Equation (2-12) which depends on k values calculated for each point within the FOV. C is dependent on the dimensions of the FOV only and can be calculated once and stored for use in efficient estimation of improved displacements. Having this equation in addition to the displacement fields obtained from the previous step (U_m), i.e., $IU = U_m$, we can form the following linear system of equations and solve it to obtain an improved estimate of U .

$$\begin{bmatrix} C \\ I \end{bmatrix} U = \begin{bmatrix} 0 \\ U_m \end{bmatrix} \rightarrow AU = b \quad (2-14)$$

In this work, we seek $U \in \mathbb{R}$ which minimizes $\frac{1}{2} U^T A^T A U - (A^T b)^T U$. As such, Equation (2-14) can be solved efficiently using the Polak-Ribiere conjugate gradient method [57]. Since the initial estimate of axial displacements are known to be more accurate than their lateral counterparts, we also employed weighted least-squares optimization [58] when solving Equation (2-14). For this purpose, W was considered as the weight diagonal matrix where $w_{i,i}$ represents the importance of i^{th} row in Equation (2-14). This equation is an augmented system consisting of three different sets of equations. With $m \times n$ data grid, the first part has $N_1 = (m - 1) \times (n - 1)$ rows which is related to incompressibility, the second and third parts each have $N_2 = m \times n$ rows pertaining to the measured axial and lateral displacements, respectively. For each part, we assign a single weight denoted by

w_{inc} , w_{lat} and w_{ax} corresponding to the incompressibility, axial displacements, and lateral displacements, respectively, leading to the weight matrix given in Equation (2-15). With this alternative, we form $WAU = Wb$ and use the Polak-Ribiere conjugate gradient method to solve it, leading to a further refined displacement field.

$$W = \begin{bmatrix} w_{inc} & & & & \\ & \ddots & & & \\ & & w_{inc} & & 0 \\ & & & w_{lat} & \\ & & & & \ddots \\ & & 0 & & w_{lat} \\ & & & & \\ & & & & w_{ax} \\ & & & & \ddots \\ & & & & w_{ax} \end{bmatrix} \quad (2-15)$$

In this work, we used the three different weight sets presented in Table 2-1. The rationale for choosing these weight factors is based on the reliability of each set of data. In these sets, the ratio of w_{ax} to w_{lat} was set to 10 based on a typical SNR ratio of 10 between axial and lateral displacement data [59]. The w_{inc} was assigned three different values of 1, 5 and 10. These weight sets were evaluated using an *in silico* phantom study as discussed in section 2.2.2.1.

Table 2-1: Different weight sets used for enforcing tissue incompressibility

Data\Weight Sets	WS1	WS2	WS3
Incompressibility Equation	1	5	10
Lateral Displacement	1	1	1
Axial Displacement	10	10	10

3) Step 3: Strain Compatibility Enforcement

The final step in the proposed method is enforcing the tissue strain compatibility [60]. The equation governing strain compatibility is given below in terms of the strain tensor components:

$$\frac{\partial^2 \varepsilon_{xx}}{\partial y^2} + \frac{\partial^2 \varepsilon_{yy}}{\partial x^2} - 2 \frac{\partial^2 \varepsilon_{xy}}{\partial x \partial y} = 0 \quad (2-16)$$

A numerical approximation was derived for this equation using the finite difference method, which was then applied to all grid points in the FOV, leading to the following matrix equation:

$$P\varepsilon = 0 \quad (2-17)$$

Here, ε is a vector containing lateral, axial and shear strains, and P is a coefficient matrix containing parameters of the finite difference approximation of the compatibility equation. Combined with the strains calculated based on the refined displacements obtained in the previous step, the following system of equations can be obtained.

$$\begin{bmatrix} P \\ I \end{bmatrix} \varepsilon = \begin{bmatrix} 0 \\ \varepsilon_m \end{bmatrix} \rightarrow B\varepsilon = e \quad (2-18)$$

This equation can be solved using the Polak-Ribiere method to obtain a further refined estimate of the strain.

2.2.2 Method Validation

2.2.2.1 In-silico Breast Phantom Study

The proposed method was first validated using an *in silico* breast biomechanical model. To generate the breast *in silico* model, a typical breast geometry was segmented from a 3D US image which captured the entire breast volume, using 3D Slicer (www.slicer.org). To generate the breast FE mesh, the segmented geometry was processed using IA-FEMESH (MIMX, Iowa city, IA, USA). A spherical inclusion was defined within the breast mesh to mimic the breast tumor. For better realism, the breast tissue, including the background and tumor regions was modeled as hyperelastic material using the polynomial model. The

hyperelastic parameters of the normal and tumor tissues in the breast were assigned based on values reported in the literature [55], [61].

For simulating breast compression using an US probe mimicking a typical USE procedure, ABAQUS FE solver (ABAQUS 2019, Dassault Systèmes Simulia Corp., Johnston, RI, USA) was used. The probe's loading was applied using a contact mechanics model following the master-slave approach. To improve the simulation realism, the contact problem was carried out in two steps. In the first step, the probe was lowered onto the breast model until it was in full contact with the surface of the breast. The second step involved further quasi-static compression to achieve the breast's desired deformation. After deforming the breast model, we obtained the displacement field within the mid-plane beneath the probe. As shown in Figure 2-4b, this mid-plane represents the US FOV. Consistent with USE, only the displacements pertaining to the second compression step was considered to mimic the displacement data. To add more realism to the displacement data obtained from this simulation, white Gaussian noise was added such that the ratio of noise amplitude of the lateral to the axial directions was 10. The SNR of the noisy axial and lateral displacement fields were 40 and 13.5, respectively. For validation, we input this simulated noisy displacement field to the developed algorithm and compared the output displacement field with the noise free version using the normalized mutual information (NMI) as similarity criterion. Equation (2-19) shows the formula for calculating this measurement for two fields of A and B. In this equation, $H(A)$ and $H(B)$ show the entropy of field and $H(A, B)$ shows the joint entropy of A and B. Utilizing the displacement field generated in this part, we evaluated and compared the validity of the incompressibility Equation (2-12) developed based on Boussinesq's model against the plane strain model-based incompressibility Equation (2-6).

$$NMI(A, B) = \frac{2 \times (H(A) + H(B))}{H(A, B)} \quad (2-19)$$

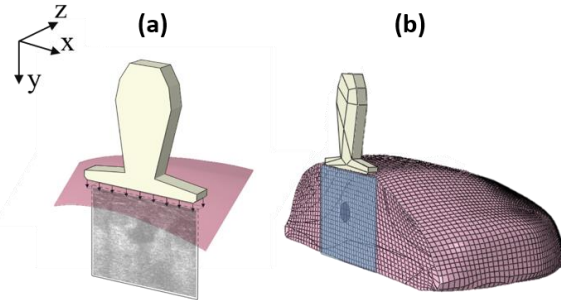


Figure 2-4: (a) Part of the breast surface under a rectangular contact pressure of the US probe and image’s rectangular FOV where at each point of this FOV, the stress values are calculated by integration of Equations (2-7), (2-8) and (2-9) over the probe’s contact surface. (b) Part of the breast FE model cut at the spherical tumor region with a rigid US probe pushing against the breast. The rectangular surface mimics the US FOV. As shown in the figure, x, y, and z directions are corresponding to lateral, out-of-plane, and axial, respectively.

To determine a proper weight set of equations among the three candidates given in Table 2-1, we used an ad hoc method whereby the NMI value between the “true” and refined displacement fields and the number of elements that satisfy the compatibility equation accurately were evaluated. The best selected weight set candidate was the one that led to the highest NMI value and largest number of compatible elements.

2.2.2.2 Tissue Mimicking Breast Phantom Study

To evaluate the displacement enhancement, the proposed method was applied to three separate tissue-mimicking breast phantoms consisting of soft background and stiff tumor tissues. The first phantom is Breast Elastography Phantom Model 059 (Computerized Imaging Reference Systems (CIRS, Norfolk, VA, USA)). The size, shape, and ultrasonic characteristics of this phantom mimic that of an average human breast in supine position accurately while it contains several lesions ranging in size from 3 to 10 mm in diameter. Two different regions of the phantom, henceforth called Phantom A and B, were tested. The second phantom, referred to as Phantom C, is a block-shaped phantom with a single inclusion (CIRS, Norfolk, VA, USA). For data acquisition of the first and second phantoms, the US probe was controlled with a mechanical device to compress the phantom

with 0.1 inches steps and the US RF data was acquired using an Antares Siemens system (Issaquah, WA, USA) and a VF10-5 linear array transducer at center frequency of 6.67 MHz and a sampling frequency of 40 MHz. The last phantom, D, was a breast-shaped phantom constructed in our laboratory using gelatin and agar dissolved in water [62]. The RF data for this phantom was acquired using an Ultrasonix RP system (Ultrasonix Medical Corporation, Richmond, BC, Canada) and a L14-5/38 linear array transducer with a nominal frequency of 10 MHz at a sampling frequency of 20 MHz. The displacement and strain fields were initially estimated using GLUE method [31], [32]. We then refined the displacement and strain fields using the proposed technique, STREAL. To quantify improvements in the strain images, the following unitless metrics of signal to noise ratio (SNR) and contrast to noise ratio (CNR) were used:

$$SNR = \frac{\bar{s}}{\sigma} \quad (2-20)$$

$$CNR = \sqrt{\frac{2(\bar{s}_b - \bar{s}_t)^2}{\sigma_b^2 + \sigma_t^2}} \quad (2-21)$$

Here, \bar{s} and σ are the spatial average and variance of a window in the strain image, respectively. Similarly, \bar{s}_b , \bar{s}_t , σ_b , and σ_t are the spatial average and variance of strains of a window in the target and background areas, respectively. To further evaluate the performance of the STREAL method, three breast tissue mimicking phantoms were simulated using ABAQUS FE solver (ABAQUS 2019, Dassault Systèmes Simulia Corp., Johnston, RI, USA). The geometries of these phantoms were chosen to be hemisphere followed by a cylinder, rectangular cuboid, and sole hemisphere with appropriate sizes to mimic phantoms A/B, C, and D, respectively. Spherical inclusions were placed inside the generated *in silico* phantoms consistent with the actual phantoms' inclusions. The models were all linear elastic with the same Young's moduli as the actual phantoms. Quasi-static stimulations were then applied to the surfaces of the phantoms before the displacement fields of the mid-plane of the phantoms were computed. Normalized cross correlation (NCC) was used to compare these fields to the estimated ones using other popular tissue motion tracking methods of Global Ultrasound Elastography (GLUE) [74] and Second-order Ultrasound Elastography (SOUL) [81].

2.2.2.3 Clinical Breast Ultrasound Elastography Case

Further evaluation of the proposed method was carried out using USE data acquired from two breast cancer patients in accordance with institutional research ethics board (REB) approval from Sunnybrook Health Sciences Centre, Toronto, Canada (REB PIN: 1994). A Sonix RP System (Ultrasonix, Vancouver, Canada) and a L14-5/60 transducer with a nominal frequency of 10 MHz was used to acquire ultrasound B-mode images and RF data at a rate of 12 frames per second. The RF data were collected at pre- and post- compression states of a quasi-static stimulation of the breast using the US probe by a trained sonographer. Similar to the phantom study, initial displacements and strain fields were estimated using the GLUE method before they were refined using the STREAL algorithm. SNR and CNR of the strain images before and after using the STREAL algorithm were calculated for quantitative comparison.

2.3 Results

2.3.1 *In silico* Breast Phantom Study

The simulated axial and lateral displacement fields in the FOV plane of the *in silico* breast phantom, including their noisy counterparts, are shown in Figure 2-5. This figure also illustrates the refined displacement fields using steps 1 and 2 of the proposed STREAL method. To show the progressive improvement achieved through each step of the algorithm, NMI values of images obtained with the noisy images and each of their refined counterpart is reported in Table 2-2.

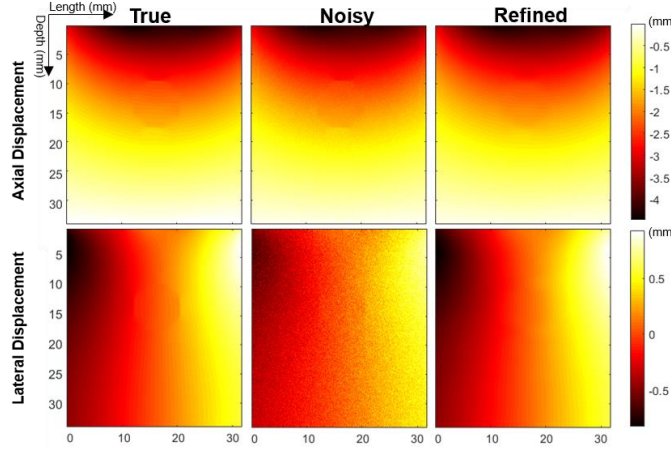


Figure 2-5: Original displacement fields generated from the *in silico* breast model, their noisy counterparts, and refined displacement fields after steps 1 and 2 of STREAL

Incompressibility equation was calculated at each point within the FOV using the displacement data acquired from simulation and based on plane-strain assumption and the Boussinesq's derived model. This led to the images shown in Figure 2-6 where visual inspection shows that the resultant of Figure 2-6 is closer to the ideal uniformly black region compared to the image in Figure 2-6 which shows large values of incompressibility equation at the top. Compared to theoretical value of 0 for this equation, the norms of these images are 32.83 and 14.75 for the plane-strain and Boussinesq's derived models, respectively. This indicates that the tissue incompressibility distribution obtained based on the proposed Boussinesq's derived model is superior to its plane-strain derived counterpart. Figure 2-7 also shows the plot of NMI between the “true” and refined axial and lateral displacement fields against the weight set candidates given in Table 2-1 and the plot of percentage of compatible FE elements based on a threshold value of 0.02. The plots indicate that the weight set WS1 leads to the best outcome. Figure 2-7 also shows that the WS1 set leads to ~20% compatible elements which may seem low; however, it should be noted that this percentage increases significantly by relaxing the threshold value such that near compatible elements are included. For example, choosing a threshold value of 0.05 leads to ~60% compatible elements for WS1. However, this choice makes comparing the different weight sets more difficult as the percentage of compatible elements in different

weight sets are closer in this case. Finally, Figure 2-8 illustrates the true (generated from Abaqus), noisy, and refined strain fields using steps 1, 2 and 3 of the proposed method.

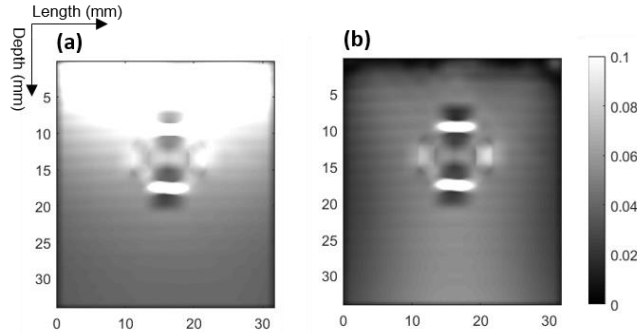


Figure 2-6: Incompressibility equation calculated using the simulated displacement data based on (a) plane strain assumption and (b) semi-infinite medium model. The latter is closer to uniformly black image (zero field) that represents an ideal incompressible tissue.

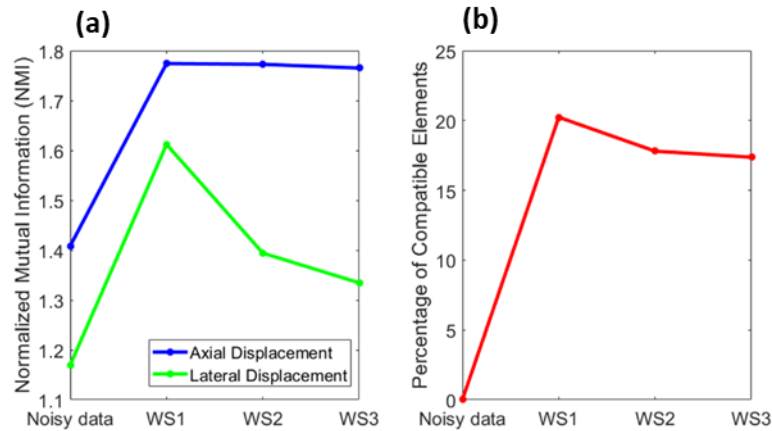


Figure 2-7: Evaluation of the weight sets used for enforcing tissue incompressibility in the *in silico* phantom study; c) the NMI similarity measure between true and refined displacements, d) percentage of compatible FE elements.

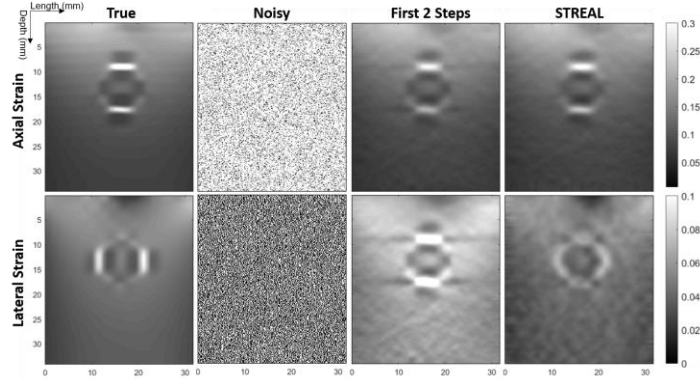


Figure 2-8: True and refined strain fields at different stages of applying STREAL

Table 2-2: NMI values of displacement and strain fields generated using the algorithm steps with corresponding “true” fields in the *in silico* phantom study

NMI with ground truth (<i>in silico</i>)		
Axial Displacement	Noisy	1.5173
	Refined by STREAL	1.7795
Lateral Displacement	Noisy	1.2026
	Refined by STREAL	1.7615
Axial Strain	Noisy	1.0023
	Refined by STREAL	1.3600
Lateral Strain	Noisy	1.0025
	Refined by STREAL	1.2121

2.3.2 Tissue Mimicking Breast Phantom Study

Figure 2-9 illustrates the results generated for four tissue mimicking phantom cases, A, B, C and D. It includes the axial and lateral displacement results generated by the GLUE,

SOUL, and the proposed STREAL technique. Generally, Figure 2-9 indicates that in contrast to the axial displacement fields that show some improvement, the lateral displacement fields are improved substantially as these fields show clear evidence of the inclusions. Figure 2-10 illustrates the phantom strain images obtained using the GLUE, SOUL, and proposed STREAL techniques. This figure shows that the proposed method is capable of generating substantially better-quality axial strain and superior quality lateral strain compared to both the GLUE and SOUL methods. The calculated SNR and CNRs as well as the local mean strain values for both background and inclusion areas are presented in Table 2-3. Overall, the STREAL technique is successful in improving the SNR and CNR of axial strain images of the phantoms by 59% and 51% compared to the GLUE technique, respectively. Moreover, compared to the GLUE method, the STREAL technique is even more effective with lateral strain images of the phantoms with about 127% and 554% improvement in the SNR and CNR, respectively. Table 2-4 shows the similarity between displacement and strain fields generated through the *in silico* simulation of the phantoms and their counterparts computed using the GLUE, SOUL, and STREAL methods. Once again, these results indicate that while compared to the GLUE and SOUL methods, the STREAL method leads to some improvement in the accuracy of axial displacements, it leads to superior quality lateral displacements. An exception is with Phantom D which is anticipated as the thickness of the breast phantom was very limited, hence the semi-infinite medium model was not effective.

Table 2-3: Similarity between displacement and strain fields generated by the *in silico* simulation and counterpart fields computed by the GLUE, SOUL, and STREAL methods

		NCC with the generated counterpart using <i>in silico</i> simulation		
		GLUE	SOUL	STREAL
Phantom A	Axial Displacement	0.9917	0.9919	0.9925
	Lateral Displacement	0.5907	0.3695	0.8881
Phantom B	Axial Displacement	0.9210	0.9200	0.9213
	Lateral Displacement	0.4302	0.5183	0.7909
Phantom C	Axial Displacement	0.8887	0.8384	0.8894
	Lateral Displacement	0.4944	0.3795	0.6601
Phantom D	Axial Displacement	0.9531	0.8919	0.9643
	Lateral Displacement	0.4909	0.4138	0.5234

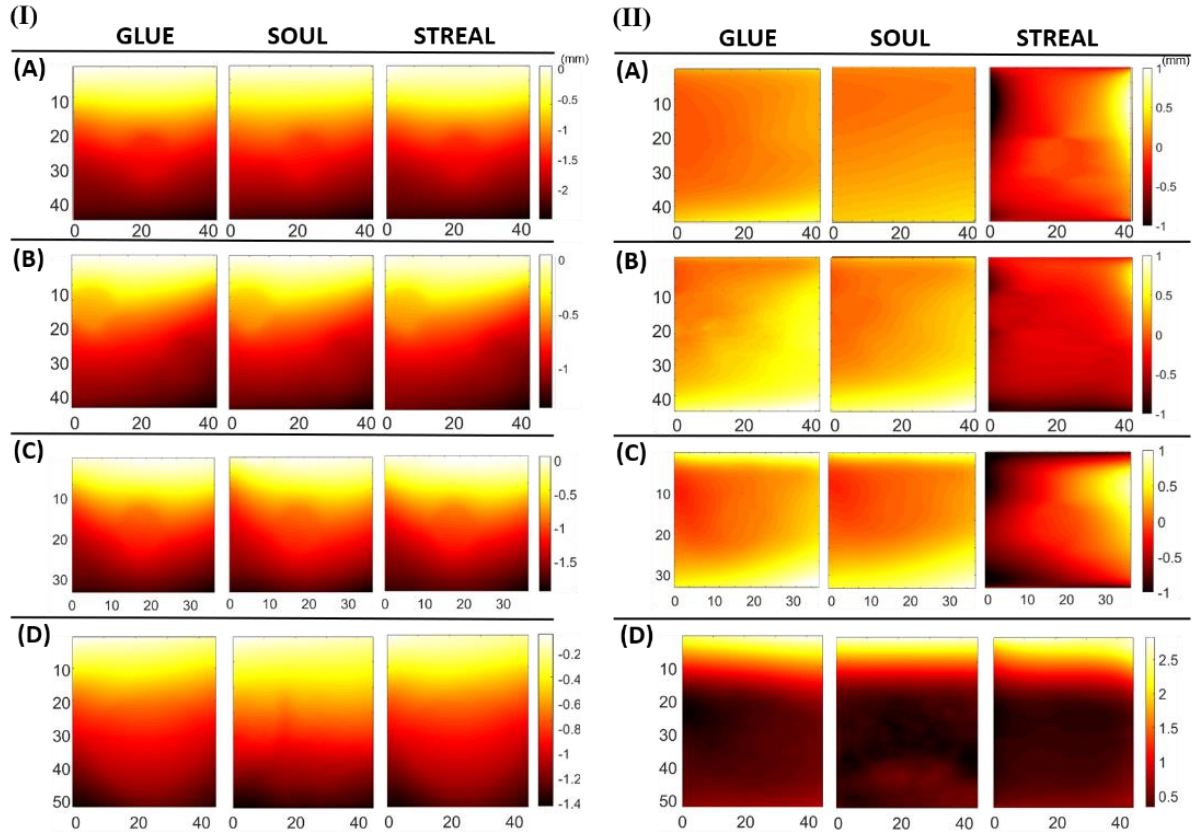


Figure 2-9: Axial (I) and lateral (II) displacement fields obtained from GLUE, SOUL, and the proposed STREAL methods for phantom cases A-D. Note that these results were obtained after performing the first two steps of the STREAL algorithm since the third step only applies to strain fields.

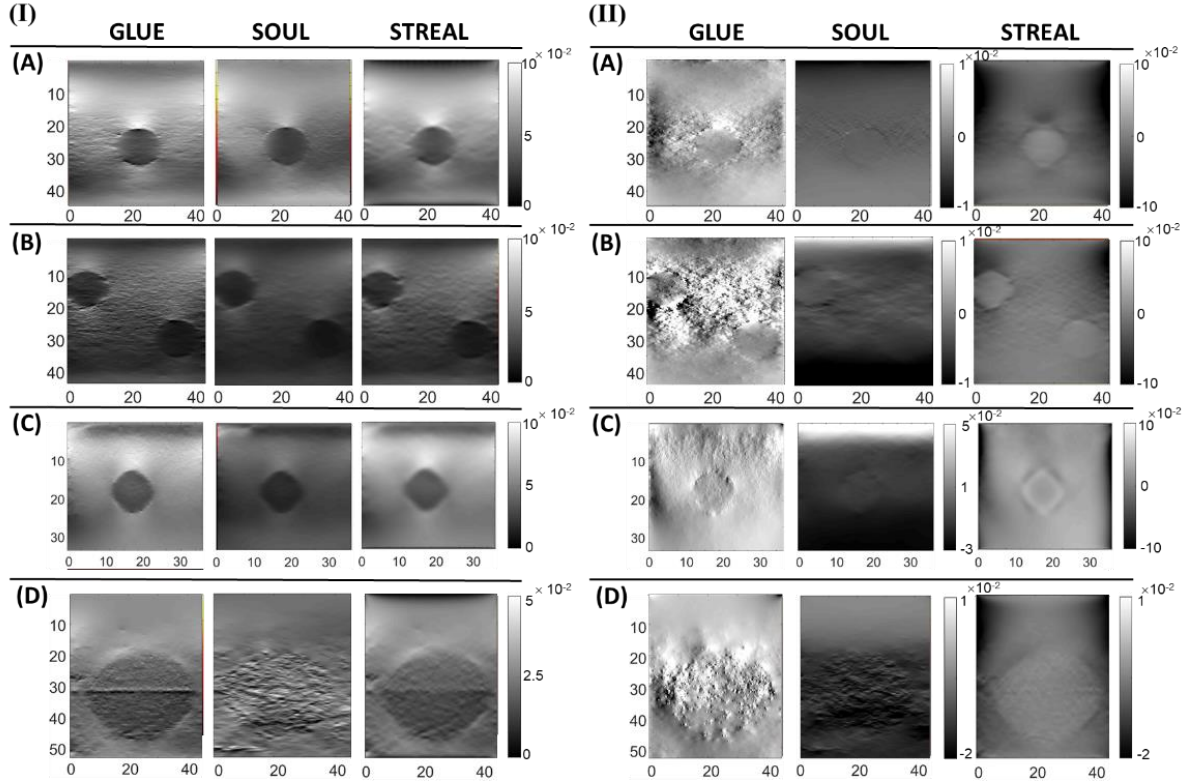


Figure 2-10: Axial (I) and lateral (II) strain images obtained from GLUE, SOUL, and the proposed STREAL method for phantom cases A-D. Note that the figures show the real values of axial and lateral strains, and the positive values represent compression. Due to inconsistency between the lateral strain values of different methods, different color bars are adjusted for each method to have the best visualization.

2.3.3 Clinical Breast Ultrasound Elastography Case

Figure 2-11 shows a breast B-mode image of the clinical case. The lateral and axial strain images generated by the GLUE method and the STREAL technique for this clinical case are shown in Figure 2-12. This figure also includes the results generated by the SOUL method. As the figure illustrates, improvement of both axial and lateral strains was achieved by applying the proposed STREAL technique.

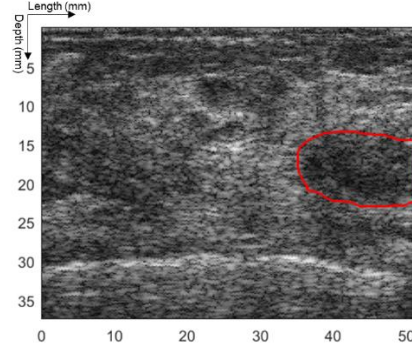


Figure 2-11: B-mode images of clinical case where the red outline shows the tumor area

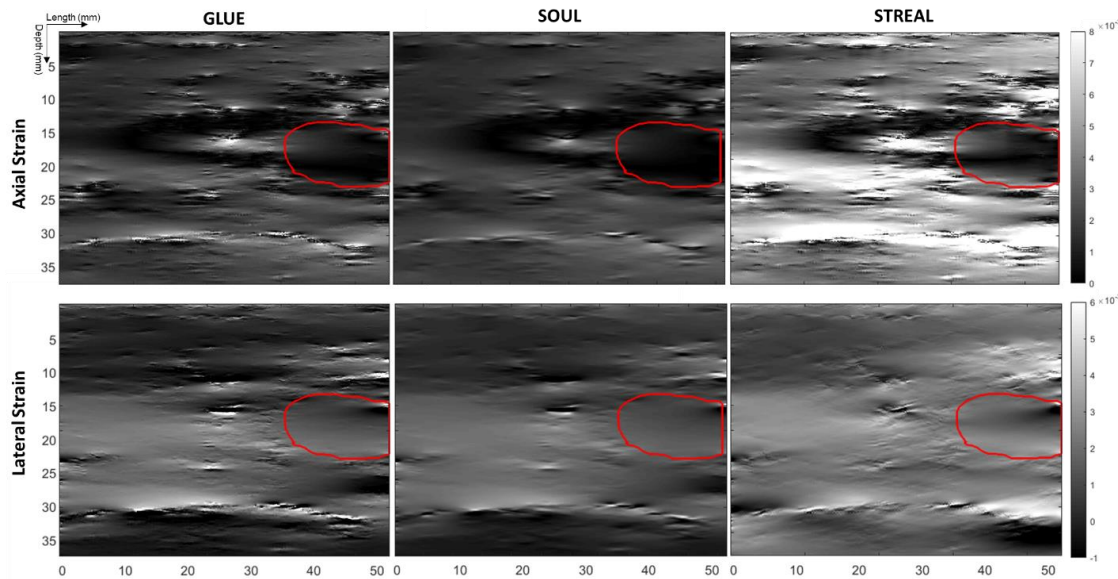


Figure 2-12: Axial and lateral strain images of the clinical case generated using GLUE, SOUL, and STREAL techniques. The red outline shows the tumor area based on the B-mode image.

Quantitative assessment based on the bottom rows of Table 2-4 shows that the method significantly improves the SNR and CNR values of both axial and lateral strain images compared to GLUE and SOUL methods.

Table 2-4: Calculated SNR and CNR metrics for axial and lateral strain images of the 4 phantoms

Strain Image	SNR			CNR			
	GLUE	SOUL	STREAL	GLUE	SOUL	STREAL	
Phantom A	Axial Strain	8.7	15.9	18.8	5.0	5.2	10.4
	Lateral Strain	2.7	2.5	13.2	0.8	0.8	12.3
Phantom B	Axial Strain	3.9	4.2	7.1	1.1	1.0	2.1
	Lateral Strain	1.7	2.1	3.2	1.4	1.2	1.9
Phantom C	Axial Strain	9.1	8.9	9.1	4.5	3.2	4.6
	Lateral Strain	2.2	1.6	2.6	1.0	0.8	3.3
Phantom D	Axial Strain	8.5	9.3	11.6	3.6	2.4	3.6
	Lateral Strain	3.3	4.2	3.7	0.8	1.2	0.8
Clinical Case	Axial Strain	1.98	2.05	2.76	2.35	1.61	3.26
	Lateral Strain	1.41	2.18	2.21	0.12	0.09	0.19

2.4 Discussion

In this work, we presented a novel method for computing tissue displacement and strain fields generated in typical ultrasound imaging. The method was designed for applications in quasi-static USE, including breast, prostate, and liver elastography. In addition to enhancement of axial displacement images where the field has already made significant progress, a major feature of the proposed method is its ability to obtain accurate lateral displacement and strain images. The proposed method attempts to take full advantage of available constraints governing the tissue mechanics. In addition to enforcing displacement field continuity conditions, this technique utilizes tissue biomechanics principles for further improvement of strain image accuracy. The principles include tissue incompressibility and displacement compatibility which are incorporated in the model to generate accurate estimation of both axial and lateral displacement and strain images.

To enforce tissue incompressibility, we developed a method which utilizes the Boussinesq semi-infinite analytical model to estimate the out-of-plane strain component before its incorporation in the general tissue incompressibility equation. To our knowledge, we are the first group to consider an estimate of the out-of-plane strain in tissue 2D motion tracking pertaining to USE. The method developed using the Boussinesq model assumes Young's modulus and Poisson ratio values of 3kPa and 0.495, respectively. The 3kPa is a widely accepted average value [63], while the 0.495 is also a broadly accepted value which is consistent with the very high water or lipid content of the breast tissue. Moreover, sensitivity analysis indicated low sensitivity of generated displacement and strain fields w.r.t these values. The proposed technique enforces the fundamental displacement compatibility equation to further enhance the strain field. While other investigators have utilized this equation to assess the quality of estimated displacement fields [52], to our knowledge, the STREAL algorithm is the first to incorporate the compatibility equation for strain field refinement. Unlike other methods where continuity based regularization is imposed at the RF data processing stage [33], [34], [40], [41], [44], the proposed technique is formulated to improve previously estimated displacement and strain images irrespective of their source and imaging modality.

In breast USE, the breast can be idealized as a semi-infinite medium and out-of-plane strain can be analytically calculated using the Boussinesq model. We first used this idealization with synthetic displacement data obtained from a simulated breast after it was contaminated with realistic noise. The results showed that the method is successful in almost entirely eliminating the noise. The *in silico* breast model represents a good breast model in terms of geometry and material behavior. Hence, the semi-infinite model used to develop the incompressibility equation in this work is anticipated to be effective with clinical data as supported by the reported clinical case. The presented formulation involves weight factors pertaining to axial and lateral data in addition to tissue incompressibility. In this investigation we attempted to find the optimal set of these factors, however, further investigation and more rigorous method is required to find a robust set that can be reliably used in the clinic.

The proposed method was further validated using tissue-mimicking phantoms, including breast-shaped and block-shaped with one or several inclusions. Figure 2-9 and Figure 2-10 and Table 2-4 indicate that, in all phantom cases, the proposed method produces substantially better and superior strain images compared to the GLUE technique for the axial and lateral directions, respectively. Results of the clinical case show that the STREAL technique can improve axial and lateral strains qualitatively as, compared to the images produced using the GLUE technique, the tumor area is more distinguishable. The results also indicate that the proposed method is superior compared to the GLUE technique as it shows 127% and 554% improvement in the SNR and CNR of the lateral strain images. It is noteworthy that although the lateral strain images generated using the STREAL technique are significantly dissimilar to the ones generated using the GLUE and SOUL methods, the *in silico* results show that the STREAL technique is more successful in generating realistic and accurate lateral strain images. By excluding Phantom D that led to only 14% improvement in the lateral displacement estimation, this conclusion is supported by the obtained higher accuracy of the displacement images, including average lateral displacement accuracy improvement over competitor methods of 34% to 46% measured by image similarity with corresponding ground truth images. Therefore, while the GLUE and SOUL methods are capable of producing reasonably accurate axial strain images that can be used for clinical applications, the quality of their lateral strain images are generally

low. In contrast, the proposed method is very promising in producing accurate lateral strain images. This can have a significant impact in improving Young's modulus images generated using inversion techniques as the image reconstruction is generally known to involve an ill-posed inverse problem, hence it can benefit substantially from availability of additional high quality data [86]. Such measured data enrichment can potentially facilitate the development of more complex elastography techniques targeting reconstruction of more realistic model (e.g., anisotropic tissue model) parameters.

It is notable that while the results demonstrated very significant improvement in displacement and strain estimation, higher level of accuracy may be achieved by considering more realistic breast geometry and improved models to estimate the out-of-plane strain distribution before incorporating in the fundamental incompressibility constraint. A notable limitation of the proposed method is its foundation on linear elasticity which assumes small tissue deformation. This implies that it cannot be used for elastography techniques aimed at reconstructing tissue hyperelastic parameters.

References

- [1] "U.S. Breast Cancer Statistics | Breastcancer.org." https://www.breastcancer.org/symptoms/understand_bc/statistics (accessed May 26, 2021).
- [2] M. Ghoncheh, Z. Pournamdar, and H. Salehiniya, "Incidence and mortality and epidemiology of breast cancer in the world," *Asian Pacific J. Cancer Prev.*, vol. 17, no. S3, pp. 43–46, 2016, doi: 10.7314/APJCP.2016.17.S3.43.
- [3] T. J. Hoerger et al., "Estimated effects of the national breast and cervical cancer early detection program on breast cancer mortality," *Am. J. Prev. Med.*, vol. 40, no. 4, pp. 397–404, Apr. 2011, doi: 10.1016/j.amepre.2010.12.017.
- [4] N. K. Stout et al., "Benefits, harms, and costs for breast cancer screening after US implementation of digital mammography," *J. Natl. Cancer Inst.*, vol. 106, no. 6, Jun. 2014, doi: 10.1093/jnci/dju092.
- [5] M. Von Euler-Chelpin, M. Lilholm, I. Vejborg, M. Nielsen, and E. Lynge, "Sensitivity of screening mammography by density and texture: A cohort study from a population-based screening program in Denmark," *Breast Cancer Res.*, vol. 21, no. 1, p. 111, Oct. 2019, doi: 10.1186/s13058-019-1203-3.

- [6] J. Ophir, "Elastography: A quantitative method for imaging the elasticity of biological tissues," *Ultrason. Imaging*, vol. 13, no. 2, pp. 111–134, Apr. 1991, doi: 10.1016/0161-7346(91)90079-w.
- [7] J. Ophir et al., "Elastography: Ultrasonic estimation and imaging of the elastic properties of tissues," *Proc. Inst. Mech. Eng. Part H J. Eng. Med.*, vol. 213, no. 3, pp. 203–233, Mar. 1999, doi: 10.1243/0954411991534933.
- [8] A. Sarvazyan, T. J. Hall, M. W. Urban, M. Fatemi, S. R. Aglyamov, and B. S. Garra, "An Overview of Elastography-An Emerging Branch of Medical Imaging," *Curr. Med. Imaging Rev.*, vol. 7, no. 4, pp. 255–282, Nov. 2011, doi: 10.2174/157340511798038684.
- [9] M. G. Ondeck et al., "Dynamically stiffened matrix promotes malignant transformation of mammary epithelial cells via collective mechanical signaling," *Proc. Natl. Acad. Sci. U. S. A.*, vol. 116, no. 9, pp. 3502–3507, Feb. 2019, doi: 10.1073/pnas.1814204116.
- [10] I. Acerbi et al., "Human breast cancer invasion and aggression correlates with ECM stiffening and immune cell infiltration," *Integr. Biol. (United Kingdom)*, vol. 7, no. 10, pp. 1120–1134, Oct. 2015, doi: 10.1039/c5ib00040h.
- [11] S. C. Wei et al., "Matrix stiffness drives epithelial-mesenchymal transition and tumour metastasis through a TWIST1-G3BP2 mechanotransduction pathway," *Nat. Cell Biol.*, vol. 17, no. 5, pp. 678–688, May 2015, doi: 10.1038/ncb3157.
- [12] N. F. Boyd et al., "Evidence That Breast Tissue Stiffness Is Associated with Risk of Breast Cancer," *PLoS One*, vol. 9, no. 7, p. e100937, Jul. 2014, doi: 10.1371/journal.pone.0100937.
- [13] H. Karimi, A. Fenster, and A. Samani, "A novel fast full inversion based breast ultrasound elastography technique," *Phys. Med. Biol.*, vol. 58, no. 7, pp. 2219–2233, Apr. 2013, doi: 10.1088/0031-9155/58/7/2219.
- [14] W. P. Andrade et al., "Can FDG-PET/CT predict early response to neoadjuvant chemotherapy in breast cancer?," *Eur. J. Surg. Oncol.*, vol. 39, no. 12, pp. 1358–1363, Dec. 2013, doi: 10.1016/j.ejso.2013.08.025.
- [15] J. M. Correas, A. M. Tissier, A. Khairoune, G. Khoury, D. Eiss, and O. Hélenon, "Ultrasound elastography of the prostate: State of the art," *Diagnostic and Interventional Imaging*, vol. 94, no. 5. Elsevier Masson SAS, pp. 551–560, May 01, 2013, doi: 10.1016/j.diii.2013.01.017.
- [16] G. S. Gherlan, "Liver ultrasound elastography: More than staging the disease," *World Journal of Hepatology*, vol. 7, no. 12. Baishideng Publishing Group Co, pp. 1595–1600, 2015, doi: 10.4254/wjh.v7.i12.1595.

- [17] S. N. Gitau and I. K. Menge, “Elastography in Chronic Liver Diseases,” in *Ultrasound Elastography*, IntechOpen, 2020.
- [18] S. Bharat, U. Techavipoo, M. Z. Kiss, W. Liu, and T. Varghese, “Monitoring stiffness changes in lesions after radiofrequency ablation at different temperatures and durations of ablation,” *Ultrasound Med. Biol.*, vol. 31, no. 3, pp. 415–422, Mar. 2005, doi: 10.1016/j.ultrasmedbio.2004.12.020.
- [19] M. A. Lubinski, S. Y. Emelianov, and M. O’Donnell, “Speckle tracking methods for ultrasonic elasticity imaging using short-time correlation,” *IEEE Trans. Ultrason. Ferroelectr. Freq. Control*, vol. 46, no. 1, pp. 82–96, Jan. 1999, doi: 10.1109/58.741427.
- [20] A. R. Skovoroda, S. Y. Emelianov, M. A. Lubinski, A. P. Sarvazyan, and M. O’Donnell, “Theoretical analysis and verification of ultrasound displacement and strain imaging,” *IEEE Trans. Ultrason. Ferroelectr. Freq. Control*, vol. 41, no. 3, pp. 302–313, May 1994, doi: 10.1109/58.285463.
- [21] T. Varghese, “Quasi-Static Ultrasound Elastography,” *Ultrasound Clinics*, vol. 4, no. 3. NIH Public Access, pp. 323–338, Jul. 2009, doi: 10.1016/j.cult.2009.10.009.
- [22] O. Falou et al., “Evaluation of neoadjuvant chemotherapy response in women with locally advanced breast cancer using ultrasound elastography,” *Transl. Oncol.*, vol. 6, no. 1, pp. 17–24, 2013, doi: 10.1593/tlo.12412.
- [23] X. Pan, J. Gao, S. Tao, K. Liu, J. Bai, and J. Luo, “A two-step optical flow method for strain estimation in elastography: Simulation and phantom study,” *Ultrasonics*, vol. 54, no. 4, pp. 990–996, Apr. 2014, doi: 10.1016/j.ultras.2013.11.010.
- [24] C. Pellet-Barakat, F. Frouin, M. F. Insana, and A. Herment, “Ultrasound Elastography Based on Multiscale Estimations of Regularized Displacement Fields,” *IEEE Trans. Med. Imaging*, vol. 23, no. 2, pp. 153–163, Feb. 2004, doi: 10.1109/TMI.2003.822825.
- [25] V. Behar, D. Adam, P. Lysyansky, and Z. Friedman, “Improving motion estimation by accounting for local image distortion,” *Ultrasonics*, vol. 43, no. 1, pp. 57–65, Oct. 2004, doi: 10.1016/j.ultras.2004.02.022.
- [26] T. Zakaria, Z. Qin, and R. L. Maurice, “Optical-flow-based b-mode elastography: Application in the hypertensive rat carotid,” *IEEE Trans. Med. Imaging*, vol. 29, no. 2, pp. 570–578, Feb. 2010, doi: 10.1109/TMI.2009.2038694.
- [27] Y. Zhou and Y. P. Zheng, “A motion estimation refinement framework for real-time tissue axial strain estimation with freehand ultrasound,” *IEEE Trans. Ultrason. Ferroelectr. Freq. Control*, vol. 57, no. 9, pp. 1943–1951, Sep. 2010, doi: 10.1109/TUFFC.2010.1642.
- [28] A. K. Z. Tehrani and H. Rivaz, “Displacement Estimation in Ultrasound Elastography Using Pyramidal Convolutional Neural Network,” *IEEE Trans. Ultrason.*

Ferroelectr. Freq. Control, vol. 67, no. 12, pp. 2629–2639, Dec. 2020, doi: 10.1109/TUFFC.2020.2973047.

[29] Z. Gao et al., “Learning the implicit strain reconstruction in ultrasound elastography using privileged information,” Med. Image Anal., vol. 58, p. 101534, Dec. 2019, doi: 10.1016/j.media.2019.101534.

[30] M. G. Kibria and H. Rivaz, “GLUENet: Ultrasound elastography using convolutional neural network,” Lect. Notes Comput. Sci. (including Subser. Lect. Notes Artif. Intell. Lect. Notes Bioinformatics), vol. 11042 LNCS, pp. 21–28, 2018, doi: 10.1007/978-3-030-01045-4_3.

[31] H. Rivaz, E. M. Boctor, M. A. Choti, and G. D. Hager, “Real-time regularized ultrasound elastography,” IEEE Trans. Med. Imaging, vol. 30, no. 4, pp. 928–945, 2011, doi: 10.1109/TMI.2010.2091966.

[32] H. S. Hashemi and H. Rivaz, “Global Time-Delay Estimation in Ultrasound Elastography,” IEEE Trans. Ultrason. Ferroelectr. Freq. Control, vol. 64, no. 10, pp. 1625–1636, 2017, doi: 10.1109/TUFFC.2017.2717933.

[33] M. Mirzaei, A. Asif, and H. Rivaz, “Combining Total Variation Regularization with Window-Based Time Delay Estimation in Ultrasound Elastography,” IEEE Trans. Med. Imaging, vol. 38, no. 12, pp. 2744–2754, Dec. 2019, doi: 10.1109/TMI.2019.2913194.

[34] M. Ashikuzzaman, C. J. Gauthier, and H. Rivaz, “Global ultrasound elastography in spatial and temporal domains,” IEEE Trans. Ultrason. Ferroelectr. Freq. Control, vol. 66, no. 5, pp. 876–887, May 2019, doi: 10.1109/TUFFC.2019.2903311.

[35] I. Céspedes, J. Ophir, and M. Insana, “Theoretical Bounds on Strain Estimation in Elastography,” IEEE Trans. Ultrason. Ferroelectr. Freq. Control, vol. 42, no. 5, pp. 969–971, 1995, doi: 10.1109/58.464850.

[36] W. F. Walker and G. E. Trahey, “A Fundamental Limit on Delay Estimation Using Partially Correlated Speckle Signals,” IEEE Trans. Ultrason. Ferroelectr. Freq. Control, vol. 42, no. 2, pp. 301–308, 1995, doi: 10.1109/58.365243.

[37] Y. Zhu and T. J. Hall, “A modified block matching method for real-time freehand strain imaging,” Ultrason. Imaging, vol. 24, no. 3, pp. 161–176, 2002, doi: 10.1177/016173460202400303.

[38] A. M, S.-N. A, S. A, and R. H, “Combining First- and Second-Order Continuity Constraints in Ultrasound Elastography,” IEEE Trans. Ultrason. Ferroelectr. Freq. Control, vol. 68, no. 7, pp. 2407–2418, Jul. 2021, doi: 10.1109/TUFFC.2021.3065884.

[39] H. Rivaz, E. M. Boctor, M. A. Choti, and G. D. Hager, “Ultrasound elastography using multiple images,” Med. Image Anal., vol. 18, no. 2, pp. 314–329, 2014, doi: 10.1016/j.media.2013.11.002.

- [40] A. Kuzmin, A. M. Zakrzewski, B. W. Anthony, and V. Lempitsky, “Multi-frame elastography using a handheld force-controlled ultrasound probe,” *IEEE Trans. Ultrason. Ferroelectr. Freq. Control*, vol. 62, no. 8, pp. 1486–1500, Aug. 2015, doi: 10.1109/TUFFC.2015.007133.
- [41] A. Basarab, A. Lyshchik, and P. Delachartre, “Multi-frame motion estimation for freehand elastography and its application to thyroid tumor imaging,” in *2008 5th IEEE International Symposium on Biomedical Imaging: From Nano to Macro, Proceedings, ISBI, 2008*, pp. 532–535, doi: 10.1109/ISBI.2008.4541050.
- [42] M. Mirzaei, A. Asif, M. Fortin, and H. Rivaz, “3D normalized cross-correlation for estimation of the displacement field in ultrasound elastography,” *Ultrasonics*, vol. 102, p. 106053, Mar. 2020, doi: 10.1016/j.ultras.2019.106053.
- [43] Y. Wang, M. Bayer, J. Jiang, and T. J. Hall, “An Improved Region-Growing Motion Tracking Method Using More Prior Information for 3-D Ultrasound Elastography,” *IEEE Trans. Ultrason. Ferroelectr. Freq. Control*, vol. 67, no. 3, pp. 580–597, Mar. 2020, doi: 10.1109/TUFFC.2019.2948984.
- [44] Y. Wang, J. Jiang, and T. J. Hall, “A 3-D Region-Growing Motion-Tracking Method for Ultrasound Elasticity Imaging,” *Ultrasound Med. Biol.*, vol. 44, no. 8, pp. 1638–1653, Aug. 2018, doi: 10.1016/j.ultrasmedbio.2018.04.011.
- [45] L. Chen, G. M. Treece, J. E. Lindop, A. H. Gee, and R. W. Prager, “A quality-guided displacement tracking algorithm for ultrasonic elasticity imaging,” *Med. Image Anal.*, vol. 13, no. 2, pp. 286–296, Apr. 2009, doi: 10.1016/j.media.2008.10.007.
- [46] J. Jiang and T. J. Hall, “A fast hybrid algorithm combining regularized motion tracking and predictive search for reducing the occurrence of large displacement errors,” *IEEE Trans. Ultrason. Ferroelectr. Freq. Control*, vol. 58, no. 4, pp. 730–736, Apr. 2011, doi: 10.1109/TUFFC.2011.1865.
- [47] L. Chen, R. J. Housden, G. M. Treece, A. H. Gee, and R. W. Prager, “A hybrid displacement estimation method for ultrasonic elasticity imaging,” *IEEE Trans. Ultrason. Ferroelectr. Freq. Control*, vol. 57, no. 4, pp. 866–882, Apr. 2010, doi: 10.1109/TUFFC.2010.1491.
- [48] M. A. Lubinski, “Lateral displacement estimation using tissue incompressibility,” *IEEE Trans. Ultrason. Ferroelectr. Freq. Control*, vol. 43, no. 2, pp. 247–256, 1996, doi: 10.1109/58.485950.
- [49] A. R. Skovoroda, M. A. Lubinski, S. Y. Emelianov, and M. O’Donnell, “Nonlinear estimation of the lateral displacement using tissue incompressibility,” *IEEE Trans. Ultrason. Ferroelectr. Freq. Control*, vol. 45, no. 2, pp. 491–503, 1998, doi: 10.1109/58.660158.
- [50] H. Li, J. Porée, B. Chayer, M. H. R. Cardinal, and G. Cloutier, “Parameterized Strain Estimation for Vascular Ultrasound Elastography with Sparse Representation,”

IEEE Trans. Med. Imaging, vol. 39, no. 12, pp. 3788–3800, Dec. 2020, doi: 10.1109/TMI.2020.3005017.

- [51] M. O'Donnell, X. Chen, K. Kaluzynski, S. Y. Emelianov, and A. R. Skovoroda, “Strain magnitude estimation based on adaptive incompressibility processing,” Proc. IEEE Ultrason. Symp., vol. 2, pp. 1643–1646, 2001, doi: 10.1109/ULTSYM.2001.992037.
- [52] O. A. Babaniyi, A. A. Oberai, and P. E. Barbone, “Recovering vector displacement estimates in quasistatic elastography using sparse relaxation of the momentum equation,” Inverse Probl. Sci. Eng., vol. 25, no. 3, pp. 326–362, Mar. 2017, doi: 10.1080/17415977.2016.1161034.
- [53] D. T. Seidl, A. A. Oberai, and P. E. Barbone, “The Coupled Adjoint-State Equation in forward and inverse linear elasticity: Incompressible plane stress,” Comput. Methods Appl. Mech. Eng., vol. 357, Dec. 2019, doi: 10.1016/j.cma.2019.112588.
- [54] A. Tikhonov, “Solution of Incorrectly Formulated Problems and the Regularization Method,” undefined, 1963.
- [55] A. Samani and D. Plewes, “A method to measure the hyperelastic parameters of ex vivo breast tissue samples,” Phys. Med. Biol., vol. 49, no. 18, pp. 4395–4405, 2004, doi: 10.1088/0031-9155/49/18/014.
- [56] J. (1842-1929). A. du texte Boussinesq, “Application des potentiels à l'étude de l'équilibre et du mouvement des solides élastiques, principalement au calcul des déformations et des pressions que produisent, dans les solides, des efforts quelconques exercés sur une petite partie de leur surface ou de leur intérieur : mémoire suivi de notes étendues sur divers points de physique mathématique et d'analyse / par J. Boussinesq,...,” 1885, Accessed: Mar. 08, 2021. [Online]. Available: <https://gallica.bnf.fr/ark:/12148/bpt6k965115r>.
- [57] E. Polak and G. Ribiere, “Note sur la convergence de méthodes de directions conjuguées,” Rev. française d'informatique Rech. opérationnelle. Série rouge, vol. 3, no. 16, pp. 35–43, 1969, doi: 10.1051/m2an/196903r100351.
- [58] T. Strutz, Data Fitting and Uncertainty (A practical introduction to weighted least squares and beyond). Springer Vieweg, 2016.
- [59] T. L. Szabo, Diagnostic Ultrasound Imaging: Inside Out: Second Edition. Elsevier Inc., 2004.
- [60] S. P. Timoshenko, J. N. Goodier, and H. N. Abramson, “Theory of Elasticity (3rd ed.),” J. Appl. Mech., vol. 37, no. 3, pp. 888–888, Sep. 1970, doi: 10.1115/1.3408648.
- [61] H. Mehrabian and A. Samani, “An iterative hyperelastic parameters reconstruction for breast cancer assessment,” Med. Imaging 2008 Physiol. Funct. Struct. from Med. Images, vol. 6916, no. March 2008, p. 69161C, 2008, doi: 10.1117/12.770971.

- [62] S. R. Mousavi, H. Rivaz, A. Sadeghi-Naini, G. J. Czarnota, and A. Samani, "Breast Ultrasound Elastography Using Full Inversion-Based Elastic Modulus Reconstruction," *IEEE Trans. Comput. Imaging*, vol. 3, no. 4, pp. 774–782, 2017, doi: 10.1109/tci.2017.2741422.
- [63] Samani A, Zubovits J, Plewes D. Elastic moduli of normal and pathological human breast tissues: an inversion-technique-based investigation of 169 samples. *Physics in medicine & biology*. 2017;52:1565-1576. doi: 10.1088/0031-9155/52/6/002

Chapter 3

3 Enhanced Full-Inversion-Based Ultrasound Elastography for Evaluating Tumor Response to Neoadjuvant Chemotherapy in Patients with Locally Advanced Breast Cancer

*A version of this chapter has been submitted as a journal paper for publication in *Physica Medica*.*

3.1 Introduction

Breast cancer is the second most diagnosed cancer in women, estimated to affect 1 in 8 women during their lifetime [1]. About 10% to 20% of new breast cancer cases are present with locally advanced breast cancer (LABC) [4]. LABC tumors are usually larger than 5 cm and may include varying extent of skin and/or chest wall involvement [2]. The current standard treatment for LABC includes neoadjuvant chemotherapy (NAC) to shrink the tumor and make it operable before removing it surgically using procedures such as mastectomy [3]. Several studies have reported a significant correlation between patient response to NAC and improved treatment outcomes including survival metrics [4]–[7]. However, about 30% to 40% of patients do not even partially respond to standard chemotherapy, while complete response is limited to less than 30% of patients [8]–[13]. Predicting patient's response early after NAC initiation may enable physicians to offer treatment adjustments (e.g., modifying regimen, dose and/or sequence of treatment options) or even switch to salvage therapy for non-responding patients, before it is too late [14]. Such patient-specific treatment modifications can spare breast cancer patients from unnecessary side effects and improve their overall treatment outcomes and quality of life.

Current approaches for evaluation of response to NAC aim at detecting changes in tumor size in response to treatment [15]. They include physical examination or standard anatomical imaging such as computed tomography (CT), conventional ultrasound imaging, and magnetic resonance imaging (MRI). Tumor size changes, however, may take several months to become detectable, and sometimes may not be evident on imaging despite a

favorable histopathological response to therapy [16]–[18]. As such, none of these anatomical imaging modalities are routinely used in clinical settings to monitor response to NAC within the first few weeks after treatment initiation.

To develop more effective monitoring techniques, a number of studies have investigated different functional imaging modalities for evaluating cancer response to treatment [18], [19]. Such modalities evaluate physiological, metabolic, and/or molecular changes in the tumor, potentially enabling assessment of therapy response before a change in tumor size is detectable on anatomical images. In this context, dynamic contrast enhanced (DCE) MRI has been investigated to detect early changes in tumor physiology as associated with angiogenesis and microcirculation in response to chemotherapy [20]–[25]. While it showed promise for evaluation of breast cancer response to NAC, DCE-MRI is relatively expensive and requires injection of exogenous contrast agents for each assessment during the course of treatment. A number of studies have demonstrated the potential of nuclear medicine imaging including positron emission tomography (PET) for evaluating tumor response to chemotherapy by detecting early changes in tumor metabolism [26], [27]. It has been demonstrated that early mean reduction of 2-deoxy-2-[F-18] fluoro-D-glucose (FDG) uptake measured using FDG-PET/CT is significantly higher in responding tumors compared to non-responding lesions [26], [27]. PET has also shown potential for early response assessment in breast cancer patients through tumor cell proliferation assessment via quantifying 3’-[F-18] fluoro-3’-deoxythymidine (FLT) uptake [28]. These imaging modalities are, however, not always accessible, often limited in resolution while they need injection of radionuclide contrast agents, limiting the frequency of scanning patients for response evaluation during the course of treatment. Quantitative ultrasound (QUS) is another functional imaging modality that can examine response-related tumor micro-structure characteristics [29]–[36]. QUS parameters have shown high sensitivity in characterizing tumor cell death in response to cancer therapy in preclinical studies [37], [38]. Clinical studies on LABC patients undergoing NAC also demonstrated that early changes in QUS parameters after treatment initiation can differentiate patients in terms of clinical and pathological response and long-term survival [39], [40]. Diffuse optical spectroscopic imaging (DOSI) is another possible alternative to other breast imaging modalities. This modality has shown good potential in clinical applications pertinent to

breast cancer assessment and diagnosis [41]–[43]. This method has been used for monitoring NAC response in patients with breast cancer by probing changes in tumor composition, perfusion, and oxygenation [44]–[49]. However, the diagnostic performance of DOSI was found to be inferior to that of early metabolic response as monitored by FDG PET/CT in [46]. While DOSI does not require any exogenous contrast agents for imaging, it is associated with long scan time for reconstructing images with acceptable resolution, hence it has not been adapted in the clinic as a standard modality.

Several studies have demonstrated considerable correlation between tumor formation and alteration in tissue biomechanical properties [50]–[52]. Generally, the dynamic nature of the tissue extracellular matrix (ECM) plays a crucial role in cancer progression [53]. It has been demonstrated that increasing ECM stiffness as a result of excessive collagen generation during tumor formation can directly activates biological processes that result in tumor invasion and metastasis [54]. Moreover, increased collagen content in ECM can promote tumor progression and invasiveness [55]–[59]. Given that chemotherapy leads to apoptosis and other forms of cell death in tumor, it is anticipated that ECM composition is impacted significantly during effective therapy. A manifestation of such alterations is potentially tissue stiffness reduction. In other words, there is a potential correlation between chemotherapy response and tumor softening. In a study conducted by Falou et al., a commercial ultrasound machine was used for clinical strain imaging of breast tumors in 15 LABC patients before and after the start of NAC [60]. Their results demonstrated that changes in relative tumor stiffness can differentiate patients in terms of clinical and pathologic response to treatment as early as 4 weeks after the start of chemotherapy. However, ultrasound strain elastography lacks accuracy in quantifying tissue stiffness as it relies on a poor tissue stress uniformity assumption. Recently developed techniques for ultrasound elastography that are capable of quantifying tissue biomechanical properties with precise measures such as Young's modulus can potentially be adapted to monitor the biomechanical alterations in tumor in response to treatment [61], [62]. Such methods are anticipated to be capable of more reliable and earlier differentiation between responding and non-respondent patients after therapy initiation.

The present study proposes an enhanced full-inversion-based ultrasound elastography technique to quantify changes in the Young's modulus of LABC tumors as a measure of the response to NAC. This technique applies ultrasound radiofrequency (RF) data acquired via a quasi-static stimulation of breast tissue induced by ultrasound probe to generates enhanced strain images by enforcing fundamental principles of continuum mechanics. The enhanced strain images are then input to an iterative inverse finite element (FE) algorithm to reconstruct the relative Young's modulus image of the breast tissue. The method was applied to ultrasound RF data acquired from 25 LABC patients undergoing full course of NAC before (baseline) and at weeks 1, 2, and 4 after the treatment initiation. The Young's modulus ratio of tumor to the surrounding tissue was calculated at different scans and compared to the baseline for each patient. Patient responses to NAC were determined many months later using standard clinical and histopathological criteria and applied to evaluate the efficacy of the enhanced elastography method for early evaluation of therapy response. The results show a very good potential of the proposed technique in predicting the tumor response to NAC at week 1 after the start of treatment.

3.2 Materials and Methods

3.2.1 Study Protocol and Data Acquisition

This study was conducted in accordance with the institutional research ethics board approval from Sunnybrook Health Sciences Centre, Toronto, Canada (REB PIN: 1994). The study was open to all woman aged 18-85 years, diagnosed with LABC, and scheduled for NAC followed by surgery. Twenty-five eligible patients were included in the study after obtaining written informed consent. A core needle biopsy was performed for each patient to confirm cancer diagnosis. Information pertaining to tumor grade, histology, and receptor status was also acquired from respective biopsy specimens. For NAC, 14 patients (56%) received doxorubicin, cyclophosphamide followed by paclitaxel or docetaxel (AC-T/D), 2 patients (8%) received paclitaxel and cyclophosphamide (TC), and 9 patients (36%) received 5-fluorouracil, epirubicin, cyclophosphamide followed by docetaxel (FEC-D). Furthermore, all patients with HER2+ tumors received tratuzumab. The duration of chemotherapy for each patient was between three to five months. Pre- and post-treatment MRI were acquired for each patient before the start of NAC and prior to surgery, which is

typically done within a month after the completion of NAC, to determine the initial and residual tumor size.

Using a Sonix RP System (Ultrasonix, Vancouver, Canada), ultrasound B-mode images and radiofrequency (RF) data were acquired from the patients' affected breast before treatment as well as at week 1, week 2, and week 4 after the NAC initiation. A 6-cm-wide L14-5/60 transducer operating at a nominal frequency of 10 MHz and a frame rate of 12 frame/s was used in this study. Following standardized protocols for data acquisition, all the ultrasound data were acquired by a trained sonographer while the patients were lying supine with their arms above their head. The transducer focus for each patient was determined based on tumor center depth before treatment and it was kept consistent through the rest of the study. On average, 4 scan planes of the tumor were acquired for each patient in ~1-cm increments under the guidance of a physician. Raw RF data were acquired at each scan plane before and after a quasi-static stimulation of the breast by the probe and saved digitally with 16-bit resolution for use in the enhanced elastography method described later.

The patients underwent surgery after completing the course of NAC and the surgical specimens were stained with hematoxylin and eosin (H&E) for histopathology. The histopathology samples were assessed by a board-certified pathologist who kept blinded to the study results. Patients were categorized into two cohorts of responders and non-responders using the modified response (MR) grading system described in [63], [64] that is based on response evaluation criteria in solid tumors (RECIST) [15] and histopathological criteria [17], [35]. Patients with a MR score of 1-2 (less than 30% reduction in tumor size) and 3-5 (more than 30% reduction in tumor size or with very low residual tumor cellularity) were determined as non-responders and responders, respectively. In keeping with this, 17 and 8 patients in this study were identified as responders and non-responders, respectively. Table 3-1 summarizes the clinical characteristics of the patients participated in this study.

Table 3-1: Participating patients' characteristics

Characteristics	Mean ± SD / Percentage
Age	51 ± 12 years
<i>Tumor Size (Maximum Diameter)</i>	
Initial Tumor Size	5.42 ± 2.25 cm
Residual Tumor Size	2.25 ± 2.87 cm
<i>Histology</i>	
Invasive Ductal Carcinoma	88%
Invasive Lobular Carcinoma	4%
Invasive Metaplastic Carcinoma	8%
<i>Molecular Features</i>	
ER+	48%
PR+	32%
HER2+	28%
Triple Negative	40%
ER/PR+ & HER2+	16%
ER/PR+ & HER2-	32%
ER&PR- & HER2+	12%
<i>Response</i>	
Responders	68%
Non-Responders	32%

3.2.2 Enhanced Strain Imaging

Axial and lateral displacement fields for each scan plane were estimated using two frames of ultrasound RF data acquired at two states of tissue pre- and post-mechanical stimulation with the ultrasound probe. In the first step, an initial estimation of the axial and lateral displacement fields was obtained using the method proposed in [65] followed by the Global Ultrasound Elastography (GLUE) method [66]. The resulting fields were then input to the STrain REfinement ALgorithm (STREAL) [67]–[69]. This algorithm improves the accuracy of the displacement fields and strain images by imposing continuum mechanics principles of tissue incompressibility and compatibility through the following steps:

1. Applying Laplacian filtering to smooth the initial displacement fields estimated by GLUE method.
2. Estimating the ratio of out-of-plane strain to axial strain at each point within the tissue computational field of view. This estimate is derived from modeling the breast as semi-infinite medium following the Boussinesq model [68].
3. Enforcing tissue incompressibility equation in 3D using the estimates obtained in step 2 to refine the axial and lateral displacement fields.
4. Applying finite difference spatial derivative on the refined displacement fields to generate enhanced images of the tissue axial and lateral strain.
5. Enforcing strain compatibility equation to further enhance the axial and lateral strain images.

3.2.3 Full Inversion-Based Elastic Modulus Reconstruction

A full-inversion-based quasi-static elastography technique was adapted to reconstruct relative Young's modulus image of the breast tissue, using the enhanced strain images obtained through the methods presented in the previous section as input [61]. The technique applies iterative algorithm of FE analysis for computing tissue stress distribution resulting from the quasi-static mechanical stimulation followed by Young's modulus (E) calculation using 2D Hooke's law (Equation (3-1)).

$$\frac{1}{E} = \frac{\varepsilon_{yy}}{\sigma_{yy} - \nu\sigma_{xx}} \quad (3-1)$$

In this equation, ν is the tissue Poisson's ratio which is set to 0.495 according to breast tissue incompressibility, and ϵ and σ represent the strain and stress where the subscripts yy and xx correspond to the axial and lateral directions, respectively. The iterative process of E reconstruction is stopped when E values of the finite elements stop changing appreciably.

For the stress calculation part of the reconstruction technique, FE analysis was used through ABAQUS FE solver (ABAQUS/Standard, Dassault Systèmes Simulia Corp., Providence, RI, USA). For this analysis, the rectangular field of view of the ultrasound scan plane was meshed using linear quadrilateral elements developed for plane stress cases. This assumption was based on the experiment conducted and described in 2.2.1. In the FE analysis, unlike other techniques that assume ideal unconstrained boundary conditions along the outline of the field of view, we used experimentally measured prescribed displacement boundary conditions along the outline. These displacement boundary conditions were obtained from a subset of the refined displacement data obtained as described earlier, while the high-quality strain data was used in Equation (3-1) for updating E in each iteration. Two different methods were used for updating E in each iteration:

1. In the first method, similar to [61], we used Equation (3-1) throughout the iterations. The Young's modulus images obtained from this approach are labelled “axial-strain-based E image”.
2. To take advantage of the enhanced lateral strain, we also used Hooke's law in conjunction with the lateral displacements as given in Equation (3-2). In this method, we used both Equations (3-1) and (3-2) with weight factors of 10 and 1, respectively, to update E . The Youngs' modulus images obtained following this method are labelled “axial/lateral-strain-based E image”. The weight factors were selected based on previous reports that estimate the signal-to-noise ratio of ultrasound axial strain images to be typically 10 times higher compared to lateral strain images [70].

$$\frac{1}{E} = \frac{\epsilon_{xx}}{\sigma_{xx} - \nu\sigma_{yy}} \quad (3-2)$$

3.2.4 Data Analysis

Using the B-mode images, the region of each tumor was outlined in each scan plane with a physician's guidance. A representative surrounding area of normal tissue was then selected in each scan for calculating the strain or E ratio of the tumor to surrounding normal tissue. At each patient's assessment time, the strain or E ratio was first calculated for each scan plane and then averaged across all scan planes of the tumor to obtain the average ratio for the entire tumor volume. For obtaining the average E value within the tumor area in each scan plane, a Gaussian distribution was fitted to the E values within the tumor region, and the values associated with the lower 30% of the distribution were removed. This pre-processing step was performed to discard small E values pertaining to tumor heterogeneity and to obtain a better estimate of the stiff areas within the tumor region. For calculating the average E value of the surrounding normal tissue in each scan plane, any E value smaller than 50% or larger than 150% of the average E value of the normal tissue region was also discarded following the same argument and the findings of [71] on the mechanical properties of breast tissue samples. The final E ratio of tumor to normal tissue in each scan plane was then calculated by taking the ratio of the average of the remaining values in each region. A similar method was used to calculate average strain ratios.

Relative changes in the strain and E ratios from the baseline (pre-treatment scan) were calculated for each patient at weeks 1, 2, and 4 after the initiation of NAC. Statistical analysis was conducted using mixed analysis of variance (ANOVA) to assess significance of the difference in strain or E ratio change after NAC between responding and non-responding patients. Normality violations in each group of the combination of the two factors (response, scan time) were checked using the Shapiro-Wilk test. A t-test (two-sided, 95% confidence) was performed to assess if the two cohorts of patients show any significant difference in the strain or E ratio changes at each scan time (weeks 1, 2, and 4) compared to the baseline. Receiver operating characteristics (ROC) analyses were performed to assess the ability of these parameters at different scan times to differentiate between the response of the two cohorts in terms of the area under the curve (AUC). Similar analyses were performed on tumor size changes from the baseline measured at each scan time using the ultrasound images acquired for each patient. The tumor size was

determined based on the maximum tumor diameter among all the available scan planes to be consistent with the RECIST criteria.

3.3 Results

Figure 3-1 and Figure 3-2 show representative B-mode, strain and E images acquired before and at weeks 1, 2 and 4 after the NAC initiation for a responding and a non-responding patient, respectively. In the responding patient, a continuous reduction in tumor stiffness compared to the baseline is detectable starting from week 1. The reduction is more evident at weeks 2 and 4 after the NAC initiation. For the non-responding patient, minimal changes are observed in tumor stiffness in response to NAC, even at weeks 2 and 4 after the NAC onset. While possible changes in tumor stiffness after NAC can be detected on the strain images, such changes are more evident on the E images. Generally, the axial-strain-based and axial/lateral-strain-based E images have similar quality. However, for some cases the latter show better contrast in identifying tumor and healthy regions. Figure 3-3 demonstrate hematoxylin and eosin (H&E) stained histopathology images of the surgical specimens acquired for the representative patients. A large residual tumor is observed in the mastectomy specimen of the non-responding patient. The histopathology image of the responding patient demonstrates the tumor bed area with chemotherapy effect and no residual carcinoma. Both images indicate notable heterogeneity within the tumor region.

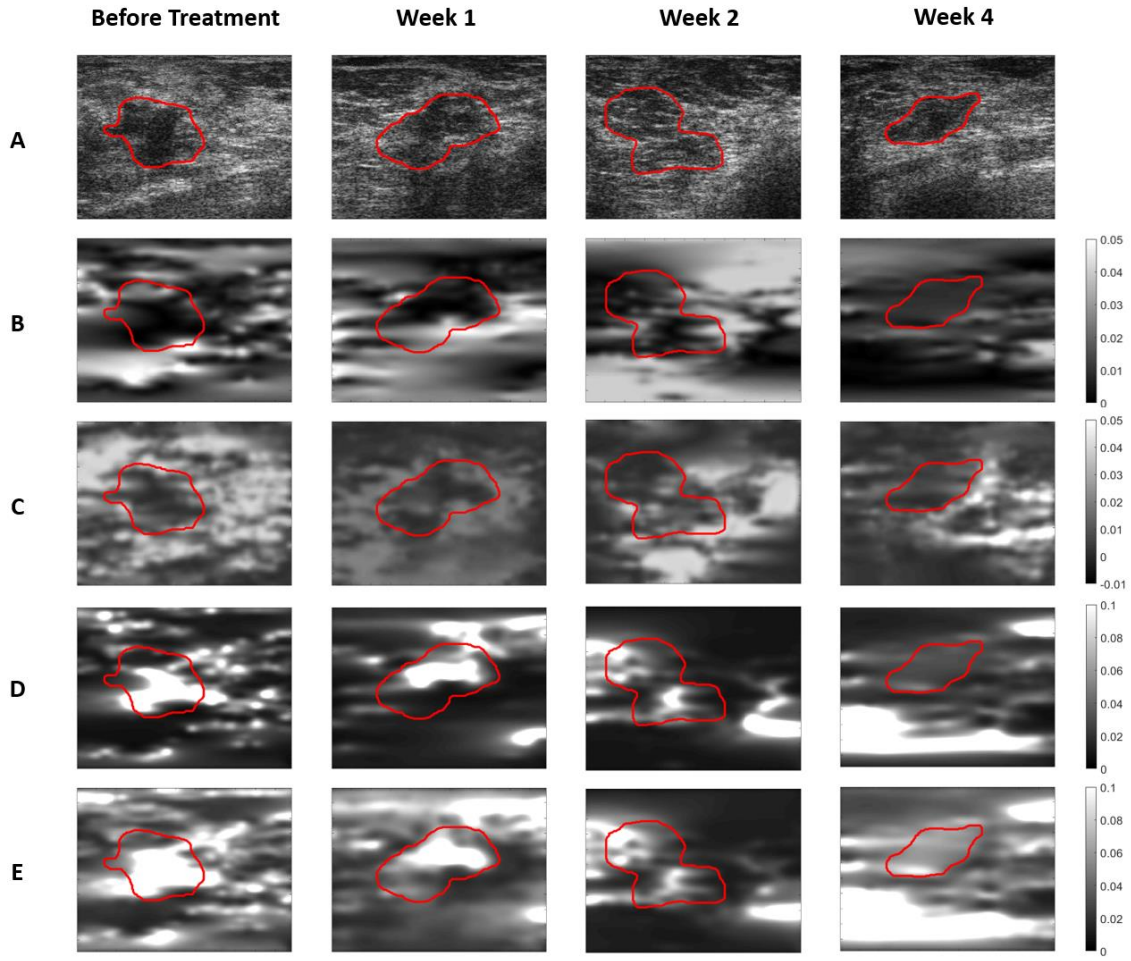


Figure 3-1: B-mode (A), axial strain (B), lateral strain (C) and relative Young's modulus images obtained based on the axial strain (D) and based on axial and lateral strains (E) obtained for a representative responder before and at different times after the NAC initiation. The axial and lateral strain images were generated using the STREAL technique.

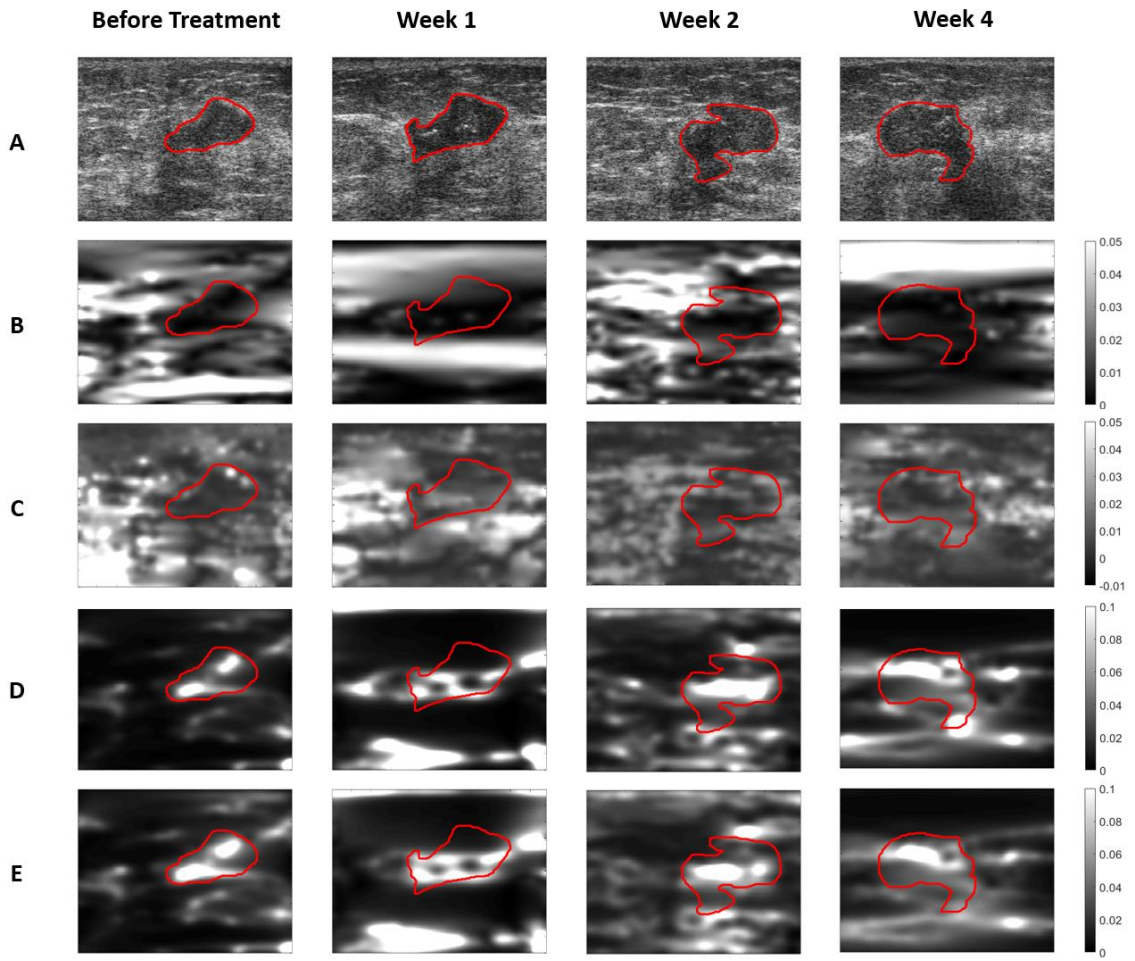


Figure 3-2: B-mode (A), axial strain (B), lateral strain (C) and relative Young's modulus images obtained based on the axial strain (D) and based on axial and lateral strains (E) obtained for a representative non-responder before and at different times after the start of NAC. The axial and lateral strain images were generated using the STREAL technique.

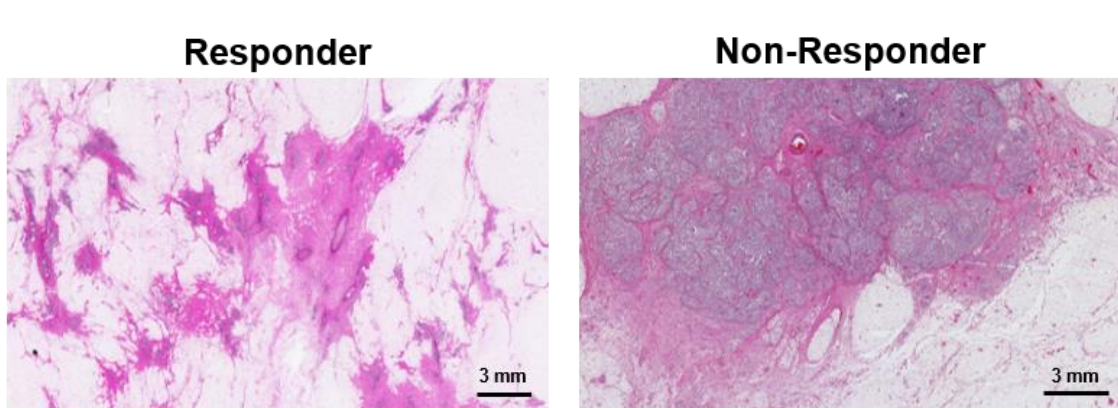


Figure 3-3: Histopathology images of surgical specimens obtained from representative responding and non-responding patients.

Figure 3-4 demonstrates average changes in the strain and E ratios compared to the baseline at different times after NAC initiation for the two patient cohorts. According to these plots, the axial strain ratio decreases over time after week 1 for the responder cohort while it shows an increase for the non-responder cohort at week 1 with little average changes afterwards. However, the lateral strain ratio demonstrates minimal changes throughout the chemotherapy for the responder cohort while showing elevations for the non-responder cohort. In the plots associated with both versions of the E image, the responder cohort demonstrates a consistent reduction in the average E ratio, starting with 15-20% decrease on average at week 1, followed by 25-30% at week 2 and 40-45% at week 4 following the treatment onset. In contrast, the non-responder cohort shows minimal change in the average E ratio after the start of the chemotherapy with less than 10% change on average even at week 4 following the treatment initiation. In summary, the change in E ratio for both versions of the E images can completely differentiate responders from non-responders as early as one week after the start of treatment, whereas a clear differentiation cannot be done based on changes in strain ratio until 4 weeks after the NAC initiation. Figure 3-5 shows average changes in tumor size from the baseline at weeks 1, 2 and 4 after the treatment onset. No substantial changes are visible in tumor size to separate the patient cohorts, with ~10% and ~5% average decrease for the responding and non-responding patients at week 4, respectively.

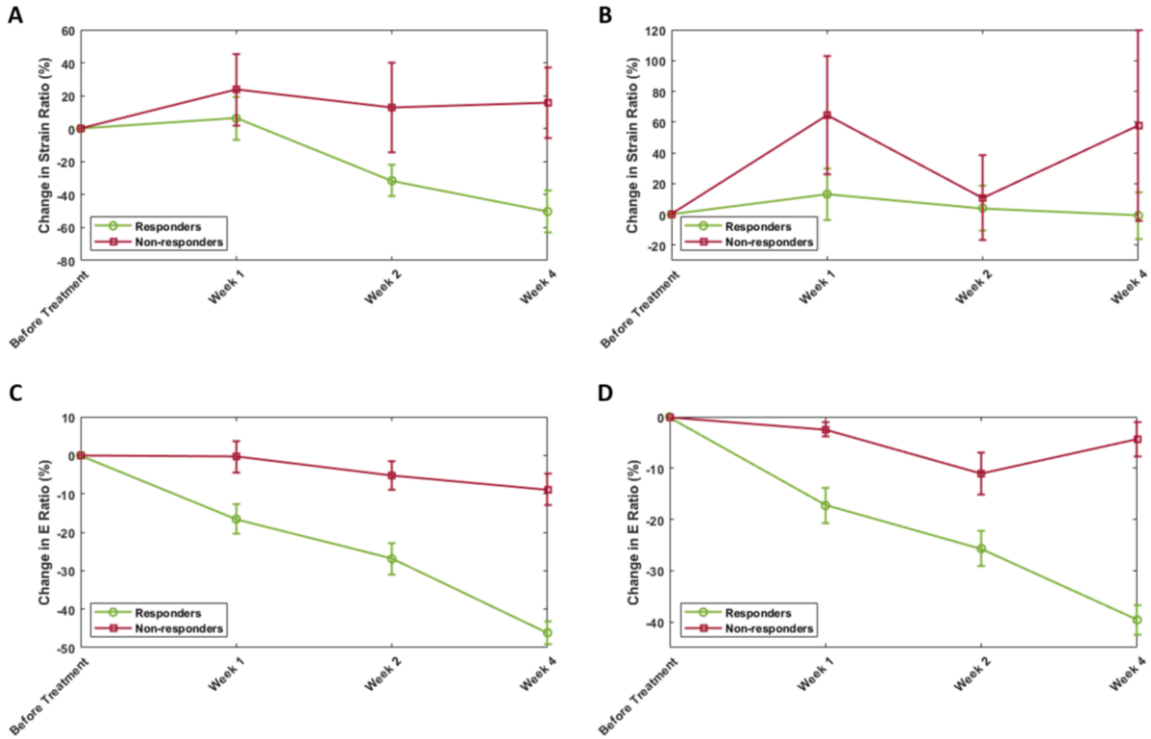


Figure 3-4: Relative changes in tumor stiffness compared to baseline after the start of NAC for responding and non-responding patient cohorts, estimated based on axial strain ratio (A), lateral strain ratio (B), E ratio obtained from the axial-strain-based relative Young's modulus image (C), E ratio obtained from the axial/lateral-strain-based relative Young's modulus image (D).

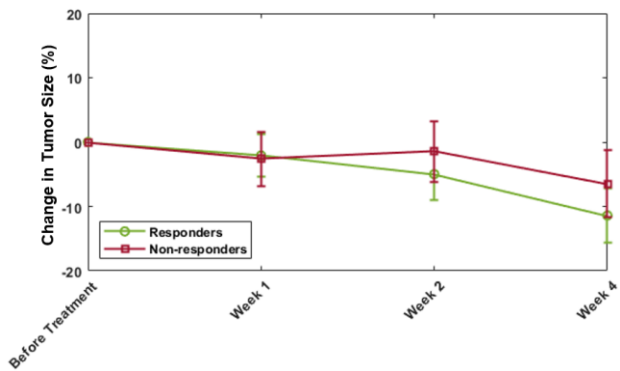


Figure 3-5: Relative changes in tumor size compared to baseline after the NAC initiation for responding and non-responding patient cohorts.

Table 3-2 shows the results of statistical analysis among the responding and non-responding patients at different scan times. The results obtained from the mixed ANOVA test demonstrate a statistically significant difference in changes in the E ratio between the responding and non-responding patients after the onset of NAC. Such difference is statistically extremely significant in the E ratio changes estimated using both approaches ($p\text{-value} < 0.001$). A similar test conducted for the changes in strain ratios and tumor size demonstrate no significant difference for the lateral strain and tumor size, but an approaching significant difference ($p\text{-value} = 0.08$) for the axial strain. Conducted t-test demonstrates a statistically significant difference in the E ratio changes from the baseline as early as one week after the treatment onset that is maintained at weeks 2 and 4, with high statistical power. In contrast, no significant difference is observed for changes in the tumor size or lateral strain ratio at weeks 1 to 4. For the axial strain ratio, a significant difference is only seen at week 4 after the treatment initiation. Moreover, results of the ROC analysis demonstrate promising AUCs obtained for changes in the E ratios at weeks 1 to 4 after the start of chemotherapy, and for the axial strain at week 4.

Table 3-2: Results of statistical analysis obtained for different elastography parameters acquired from the responding and non-responding patient cohorts at different times after the NAC initiation. *, †, and ‡ demonstrate statistically significant (p-value < 0.05), highly significant, (p-value < 0.01), and extremely significant (p-value < 0.001), respectively.

Parameter	Week	Mixed ANOVA (p-value)	T-Test (p-value)	AUC
%ΔTumor-Size	1		0.93	0.47
	2	0.90	0.63	0.61
	4		0.52	0.60
%ΔAxial-Strain-Ratio	1		0.49	0.64
	2	0.08	0.17	0.74
	4		0.01*	0.85
%ΔLateral-Strain-Ratio	1		0.16	0.67
	2	0.31	0.82	0.51
	4		0.21	0.61
%ΔE-Ratio (axial-strain-based E image)	1		0.02*	0.79
	2	<0.001‡	<0.001‡	0.85
	4		<0.001‡	0.99
%ΔE-Ratio (axial/lateral-strain-based E image)	1		<0.001‡	0.82
	2	<0.001‡	0.02*	0.77
	4		<0.001‡	1.0

3.4 Discussion and Conclusion

This study investigated, for the first time, the application of a novel full inversion-based ultrasound elastography technique for monitoring tumor response to NAC in LABC patients. The technique adapted the STREAL method [67]–[69] for enhanced strain imaging coupled with a novel methodology for reconstruction of elasticity images that permits accurate quantification of breast tissue relative Young's modulus. The method was applied on ultrasound data acquired from 25 LABC patients before and at weeks 1, 2 and 4 after the NAC initiation. Changes in tumor stiffness in response to NAC was quantified using average E and strain ratios of tumor to surrounding normal tissue obtained at 1, 2 and 4 weeks after the start of NAC initiation. Response of patients to NAC was determined after completing the course of NAC and surgery using the standard clinical and histopathological criteria. The criteria were used for evaluating the performance of the elastography parameters in assessing patients' response to NAC early after the therapy initiation. Trend of changes in tumor Young's modulus among the responding and non-responding patients indicated a very good correlation with the NAC response. In particular, while the tumor E ratio demonstrated a considerable and continuous decrease for responding patients starting at week 1, minimal changes were observed for non-responding patients even at week 4 after the NAC onset.

Statistical analysis confirmed that the method is successful in differentiating responding and non-responding patients as early as one week after the NAC initiation. Specifically, statistically significant differences were observed in E ratio changes between the responding and non-responding patients at all scans after the therapy onset (Table 3-2). The results of this statistical analysis are indicative of a substantial improvement compared to the previous study in which a significant difference (p -value = 0.002) in tumor stiffness changes was only observed after 4 weeks following the start of treatment when such changes were estimated using clinical ultrasound strain imaging [60]. The results obtained in this study with strain images supports the findings of the previous study. Here, a significant difference (p -value = 0.01) in changes of the axial strain ratios was observed only at week 4 after the chemotherapy onset. The inferior performance of the strain compared to the E images in early differentiation of the patients' response to NAC can be

attributed to the poor stiffness measure of the strain compared to the tissue Young's modulus. Strain image is a true representative of the tissue stiffness only if the stress is uniformly distributed within the breast tissue while being stimulated mechanically with the ultrasound probe for strain-based elastography. Due to the breast tissue inhomogeneity and irregular geometry, and local loading, it is well established that considerable stress non-uniformity exists within the field of view, hindering the sensitivity of strain images in estimating tumor stiffness. The full-inversion-based E reconstruction algorithm applied in this study takes tissue stress non-uniformity into account via iterative finite element analysis, leading to higher signal-to-noise ratio (SNR) in generated E images, hence higher sensitivity in quantifying small changes in tumor stiffness compared to strain images. The statistical analysis on tumor size changes measured using the ultrasound images demonstrated no significant difference between the responding and non-responding patients at weeks 1 to 4 following the treatment initiation. This observation is in agreement with findings of the previous studies in which no statistically significant difference was evident in tumor size changes measured using MRI [72] or ultrasound [73] 3-4 weeks after the start of chemotherapy.

The enhanced axial and lateral strain images obtained using STREAL were utilized to generate two versions of E images. The first version of E images was reconstructed using the enhanced axial images only, while the second version also took advantage of the enhanced lateral strain images for generating E images with higher quantitative accuracy. The quality of these images was generally comparable, but in some cases the E images reconstructed based on both the axial and lateral strain images led to better visualization of the tumor region compared to those generated based on the axial strain only. Similarly, the trends of changes in the tumor E ratio measured based on these elasticity images were similar over the course of treatment in each response cohort. However, the E ratios associated with the E images generated based on both the axial and lateral strain images provided a relatively better separation between the two cohorts at weeks 1 and 4 after the NAC initiation. In particular, a statistically extremely significant ($p\text{-value} < 0.001$; statistical power = 98%) versus significant ($p\text{-value} = 0.02$; statistical power = 83%) difference was observed in the E ratio changes measured at week 1 using the E images reconstructed based on the axial and lateral strain images, and axial strain images,

respectively. The results of ROC analysis for both these methods demonstrated a relatively high AUC for NAC response prediction at week 1 after the treatment onset. These observations support the findings of a very recent study in which ultrasound shear wave elastography was applied to measure changes in tumor Young's modulus in breast cancer patients undergoing NAC [73]. In that study, changes in tumor Young's modulus were quantified at weeks 3 and 6 after the NAC initiation, where statistically (highly) significant differences (p -value = 0.02 and 0.001) were observed between the patient cohorts with pathological complete versus non-complete response. The findings of this study encourage future studies to investigate the efficacy of the ultrasound shear wave elastography in differentiating the response cohorts at weeks 1 and 2 after the NAC initiation, based on the measured changes in tumor stiffness.

In conclusion, this study demonstrated a very good potential for the proposed full inversion-based ultrasound elastography technique in assessing and predicting tumor response to NAC in LABC patients as early as one week after the NAC initiation. Early prediction of neoadjuvant therapy response for these patients potentially facilitates treatment adjustments by clinicians on an individual patient basis. A personalized paradigm for breast cancer therapeutics is anticipated to improve the overall therapy outcome, survival, and quality of life for the patients. This study, therefore, is a step forward towards precision oncology and tailoring chemotherapies for breast cancer patients. Studies involving larger patient populations are, however, required to further evaluate the efficacy and robustness of the technique.

References

- [1] “Breast cancer statistics | Canadian Cancer Society.” <https://cancer.ca/en/cancer-information/cancer-types/breast/statistics> (accessed Nov. 24, 2021).
- [2] F. J. Esteva and G. N. Hortobagyi, “Locally advanced breast cancer,” *Hematol. Oncol. Clin. North Am.*, vol. 13, no. 2, pp. 457–472, Apr. 1999, doi: 10.1016/S0889-8588(05)70065-4.
- [3] C. D. Haagensen and A. P. Stout, “CARCINOMA OF THE BREAST*,” *Ann. Surg.*, vol. 118, no. 5, pp. 859–870, Nov. 1943, doi: 10.1097/00000658-194311850-00008.
- [4] B. Fisher *et al.*, “Effect of preoperative chemotherapy on the outcome of women with operable breast cancer,” *J. Clin. Oncol.*, vol. 16, no. 8, pp. 2672–2685, 1998,

- doi: 10.1200/JCO.1998.16.8.2672.
- [5] S. J. Cleator, A. Makris, S. E. Ashley, R. Lal, and T. J. Powles, “Good clinical response of breast cancers to neoadjuvant chemoendocrine therapy is associated with improved overall survival,” *Ann. Oncol. Off. J. Eur. Soc. Med. Oncol.*, vol. 16, no. 2, pp. 267–272, 2005, doi: 10.1093/ANNONC/MDI049.
 - [6] A. Romero *et al.*, “Correlation between response to neoadjuvant chemotherapy and survival in locally advanced breast cancer patients,” *Ann. Oncol.*, vol. 24, no. 3, pp. 655–661, 2013, doi: 10.1093/annonc/mds493.
 - [7] L. M. Spring *et al.*, “Pathologic Complete Response after Neoadjuvant Chemotherapy and Impact on Breast Cancer Recurrence and Survival: A Comprehensive Meta-analysis,” *Clin. Cancer Res.*, vol. 26, no. 12, pp. 2838–2848, Jun. 2020, doi: 10.1158/1078-0432.CCR-19-3492.
 - [8] D. Sethi, R. Sen, S. Parshad, S. Khetarpal, M. Garg, and J. Sen, “Histopathologic changes following neoadjuvant chemotherapy in locally advanced breast cancer,” *Indian J. Cancer*, vol. 50, no. 1, pp. 58–64, 2013, doi: 10.4103/0019-509X.112301.
 - [9] S. Chuthapisith, J. M. Eremin, M. El-Sheemy, and O. Eremin, “Neoadjuvant chemotherapy in women with large and locally advanced breast cancer: chemoresistance and prediction of response to drug therapy,” *Surgeon*, vol. 4, no. 4, pp. 211–219, 2006, doi: 10.1016/S1479-666X(06)80062-4.
 - [10] G. N. Hortobagyi, “Multidisciplinary management of advanced primary and metastatic breast cancer,” *Cancer*, vol. 74, no. 1 S, pp. 416–423, 1994, doi: 10.1002/cncr.2820741329.
 - [11] S. H. Giordano, “Update on locally advanced breast cancer,” *Oncologist*, vol. 8, no. 6, pp. 521–530, Dec. 2003, doi: 10.1634/THEONCOLOGIST.8-6-521.
 - [12] W. Haque, V. Verma, S. Hatch, V. Suzanne Klimberg, E. Brian Butler, and B. S. Teh, “Response rates and pathologic complete response by breast cancer molecular subtype following neoadjuvant chemotherapy,” *Breast Cancer Res. Treat.*, vol. 170, no. 3, pp. 559–567, Aug. 2018, doi: 10.1007/S10549-018-4801-3.
 - [13] T. Byrski *et al.*, “Pathologic complete response rates in young women with BRCA1-positive breast cancers after neoadjuvant chemotherapy,” *J. Clin. Oncol.*, vol. 28, no. 3, pp. 375–379, Jan. 2010, doi: 10.1200/JCO.2008.20.7019.
 - [14] E. Huang *et al.*, “Locoregional treatment outcomes for inoperable anthracycline-resistant breast cancer,” *Int. J. Radiat. Oncol. Biol. Phys.*, vol. 53, no. 5, pp. 1225–33, Aug. 2002, doi: 10.1016/S0360-3016(02)02878-X.
 - [15] E. A. Eisenhauer *et al.*, “New response evaluation criteria in solid tumours: revised RECIST guideline (version 1.1),” *Eur. J. Cancer*, vol. 45, no. 2, pp. 228–247, Jan. 2009, doi: 10.1016/J.EJCA.2008.10.026.

- [16] L. C. Michaelis and M. J. Ratain, “Measuring response in a post-RECIST world: from black and white to shades of grey,” *Nat. Rev. Cancer*, vol. 6, no. 5, pp. 409–14, 2006, doi: 10.1038/nrc1883.
- [17] K. N. Ogston *et al.*, “A new histological grading system to assess response of breast cancers to primary chemotherapy: prognostic significance and survival,” *Breast*, vol. 12, no. 5, pp. 320–327, 2003, doi: 10.1016/S0960-9776(03)00106-1.
- [18] K. Brindle, “New approaches for imaging tumour responses to treatment,” *Nat. Rev. Cancer* 2008 82, vol. 8, no. 2, pp. 94–107, Feb. 2008, doi: 10.1038/nrc2289.
- [19] “Imaging innovations for cancer therapy response monitoring,” 2012, doi: 10.2217/IIM.12.23.
- [20] R. Johansen *et al.*, “Predicting survival and early clinical response to primary chemotherapy for patients with locally advanced breast cancer using DCE-MRI,” *J. Magn. Reson. Imaging*, vol. 29, no. 6, pp. 1300–1307, Jun. 2009, doi: 10.1002/jmri.21778.
- [21] R. G. Abramson *et al.*, “Early assessment of breast cancer response to neoadjuvant chemotherapy by semi-quantitative analysis of high-temporal resolution DCE-MRI: Preliminary results,” *Magn. Reson. Imaging*, vol. 31, no. 9, pp. 1457–1464, Nov. 2013, doi: 10.1016/j.mri.2013.07.002.
- [22] N. S. Gezer, O. Orbay, P. Balci, M. G. Durak, B. Demirkan, and S. Saydam, “Evaluation of Neoadjuvant Chemotherapy Response with Dynamic Contrast Enhanced Breast Magnetic Resonance Imaging in Locally Advanced Invasive Breast Cancer,” *J. Breast Heal.*, vol. 10, no. 2, pp. 111–118, May 2014, doi: 10.5152/TJBH.2014.2035.
- [23] J. R. Teruel *et al.*, “Dynamic contrast-enhanced MRI texture analysis for pretreatment prediction of clinical and pathological response to neoadjuvant chemotherapy in patients with locally advanced breast cancer,” *NMR Biomed.*, vol. 27, no. 8, pp. 887–896, 2014, doi: 10.1002/NBM.3132.
- [24] J. Wu, G. Gong, Y. Cui, and R. Li, “Intratumor partitioning and texture analysis of dynamic contrast-enhanced (DCE)-MRI identifies relevant tumor subregions to predict pathological response of breast cancer to neoadjuvant chemotherapy,” *J. Magn. Reson. Imaging*, vol. 44, no. 5, pp. 1107–1115, Nov. 2016, doi: 10.1002/jmri.25279.
- [25] A. Sharma, S. Sharma, S. Sood, R. K. Seam, M. Sharma, and V. Fotedar, “DCE-MRI and parametric imaging in monitoring response to neoadjuvant chemotherapy in breast carcinoma: a preliminary report,” *Polish J. Radiol.*, vol. 83, p. e220, 2018, doi: 10.5114/PJR.2018.76271.
- [26] W. P. Andrade *et al.*, “Can FDG-PET/CT predict early response to neoadjuvant chemotherapy in breast cancer?,” *Eur. J. Surg. Oncol.*, vol. 39, no. 12, pp. 1358–

- 1363, Dec. 2013, doi: 10.1016/j.ejso.2013.08.025.
- [27] S. Chuthapisith, J. M. Eremin, and O. Eremin, “Predicting response to neoadjuvant chemotherapy in breast cancer: Molecular imaging, systemic biomarkers and the cancer metabolome (review),” *Oncol. Rep.*, vol. 20, no. 4, pp. 699–703, Oct. 2008, doi: 10.3892/or_00000062.
 - [28] B. S. Pio *et al.*, “Usefulness of 3’-[F-18]fluoro-3’-deoxythymidine with positron emission tomography in predicting breast cancer response to therapy,” *Mol. imaging Biol.*, vol. 8, no. 1, pp. 36–42, Jan. 2006, doi: 10.1007/S11307-005-0029-9.
 - [29] H. Tadayyon, A. Sadeghi-Naini, L. Wirtzfeld, F. C. Wright, and G. Czarnota, “Quantitative ultrasound characterization of locally advanced breast cancer by estimation of its scatterer properties,” *Med. Phys.*, vol. 41, no. 1, p. 012903, Jan. 2014, doi: 10.1118/1.4852875.
 - [30] Z. Klimonda, P. Karwat, K. Dobruch-Sobczak, H. Piotrzkowska-Wróblewska, and J. Litniewski, “Breast-lesions characterization using Quantitative Ultrasound features of peritumoral tissue,” *Sci. Rep.*, vol. 9, no. 1, pp. 1–9, Dec. 2019, doi: 10.1038/s41598-019-44376-z.
 - [31] L. Sannachi *et al.*, “Breast Cancer Treatment Response Monitoring Using Quantitative Ultrasound and Texture Analysis: Comparative Analysis of Analytical Models,” *Transl. Oncol.*, vol. 12, no. 10, pp. 1271–1281, Oct. 2019, doi: 10.1016/j.tranon.2019.06.004.
 - [32] K. Quiaoit *et al.*, “Quantitative ultrasound radiomics for therapy response monitoring in patients with locally advanced breast cancer: Multi-institutional study results,” *PLoS One*, vol. 15, no. 7, p. e0236182, Jul. 2020, doi: 10.1371/journal.pone.0236182.
 - [33] M. L. Oelze, W. D. O’Brien, and J. F. Zachary, “Quantitative ultrasound assessment of breast cancer using a multiparameter approach,” in *Proceedings - IEEE Ultrasonics Symposium*, 2007, pp. 981–984, doi: 10.1109/ULTSYM.2007.250.
 - [34] K. Dobruch-Sobczak *et al.*, “Monitoring the response to neoadjuvant chemotherapy in patients with breast cancer using ultrasound scattering coefficient: A preliminary report,” *J. Ultrason.*, vol. 19, no. 77, pp. 89–97, Jul. 2019, doi: 10.15557/JoU.2019.0013.
 - [35] H. Tadayyon *et al.*, “A priori Prediction of Neoadjuvant Chemotherapy Response and Survival in Breast Cancer Patients using Quantitative Ultrasound,” *Sci. Reports* 2017 71, vol. 7, no. 1, pp. 1–11, Apr. 2017, doi: 10.1038/srep45733.
 - [36] H. G. Nasief, I. M. Rosado-Mendez, J. A. Zagzebski, and T. J. Hall, “A Quantitative Ultrasound-Based Multi-Parameter Classifier for Breast Masses,” *Ultrasound Med. Biol.*, vol. 45, no. 7, pp. 1603–1616, Jul. 2019, doi: 10.1016/j.ultrasmedbio.2019.02.025.

- [37] A. Sadeghi-Naini *et al.*, “Low-frequency quantitative ultrasound imaging of cell death in vivo,” *Med. Phys.*, vol. 40, no. 8, 2013, doi: 10.1111/1.4812683.
- [38] A. Sadeghi-Naini *et al.*, “Conventional Frequency Ultrasonic Biomarkers of Cancer Treatment Response In Vivo,” *Transl. Oncol.*, vol. 6, no. 3, pp. 234-IN2, Jun. 2013, doi: 10.1593/TLO.12385.
- [39] A. Sadeghi-Naini *et al.*, “Quantitative ultrasound evaluation of tumor cell death response in locally advanced breast cancer patients receiving chemotherapy,” *Clin. Cancer Res.*, vol. 19, no. 8, pp. 2163–2173, Apr. 2013, doi: 10.1158/1078-0432.CCR-12-2965.
- [40] A. Sadeghi-Naini *et al.*, “Chemotherapy-Response Monitoring of Breast Cancer Patients Using Quantitative Ultrasound-Based Intra-Tumour Heterogeneities,” *Sci. Reports 2017 71*, vol. 7, no. 1, pp. 1–12, Sep. 2017, doi: 10.1038/s41598-017-09678-0.
- [41] K. Lee, “Optical mammography: Diffuse optical imaging of breast cancer,” *World J. Clin. Oncol.*, vol. 2, no. 1, p. 64, 2011, doi: 10.5306/wjco.v2.i1.64.
- [42] M. Herranz and A. Ruibal, “Optical imaging in breast cancer diagnosis: The next evolution,” *Journal of Oncology*. 2012, doi: 10.1155/2012/863747.
- [43] M. B. Applegate, R. E. Istfan, S. Spink, A. Tank, and D. Roblyer, “Recent advances in high speed diffuse optical imaging in biomedicine,” *APL Photonics*, vol. 5, no. 4, p. 40802, Apr. 2020, doi: 10.1063/1.5139647.
- [44] J. E. Gunther *et al.*, “Dynamic Diffuse Optical Tomography for Monitoring Neoadjuvant Chemotherapy in Patients with Breast Cancer,” *Radiology*, vol. 287, no. 3, pp. 778–786, Jun. 2018, doi: 10.1148/radiol.2018161041.
- [45] B. E. Schaafsma *et al.*, “Optical mammography using diffuse optical spectroscopy for monitoring tumor response to neoadjuvant chemotherapy in women with locally advanced breast cancer,” *Clin. Cancer Res.*, vol. 21, no. 3, pp. 577–584, Feb. 2015, doi: 10.1158/1078-0432.CCR-14-0736.
- [46] S. Ueda *et al.*, “Near-infrared diffuse optical imaging for early prediction of breast cancer response to neoadjuvant chemotherapy: A comparative study using 18F-FDG PET/CT,” *J. Nucl. Med.*, vol. 57, no. 8, pp. 1189–1195, Aug. 2016, doi: 10.2967/jnumed.115.167320.
- [47] O. Falou *et al.*, “Diffuse optical spectroscopy evaluation of treatment response in women with locally advanced breast cancer receiving neoadjuvant chemotherapy,” *Transl. Oncol.*, vol. 5, no. 4, pp. 238–246, 2012, doi: 10.1593/tlo.11346.
- [48] Y. H. Liu *et al.*, “Diffuse optical spectroscopy for monitoring the responses of patients with breast cancer to neoadjuvant chemotherapy,” *Medicine (Baltimore)*, vol. 97, no. 41, p. e12683, Oct. 2018, doi: 10.1097/MD.00000000000012683.

- [49] W. Zhi *et al.*, “Predicting Treatment Response of Breast Cancer to Neoadjuvant Chemotherapy Using Ultrasound-Guided Diffuse Optical Tomography,” *Transl. Oncol.*, vol. 11, no. 1, pp. 56–64, Feb. 2018, doi: 10.1016/j.tranon.2017.10.011.
- [50] G. Runel, N. Lopez-ramirez, J. Chlasta, and I. Masse, “Biomechanical Properties of Cancer Cells,” *Cells*, vol. 10, no. 4, 2021, doi: 10.3390/CELLS10040887.
- [51] S. S. Deville and N. Cordes, “The Extracellular, Cellular, and Nuclear Stiffness, a Trinity in the Cancer Resistome—A Review,” *Front. Oncol.*, vol. 9, p. 1376, Dec. 2019, doi: 10.3389/FONC.2019.01376/BIBTEX.
- [52] F. Broders-Bondon, T. H. N. Ho-Boulloires, M. E. Fernandez-Sanchez, and E. Farge, “Mechanotransduction in tumor progression: The dark side of the force,” *J. Cell Biol.*, vol. 217, no. 5, pp. 1571–1587, May 2018, doi: 10.1083/JCB.201701039.
- [53] T. R. Cox and J. T. Erler, “Remodeling and homeostasis of the extracellular matrix: Implications for fibrotic diseases and cancer,” *DMM Disease Models and Mechanisms*, vol. 4, no. 2. The Company of Biologists Ltd, pp. 165–178, Mar. 01, 2011, doi: 10.1242/dmm.004077.
- [54] S. C. Wei *et al.*, “Matrix stiffness drives epithelial-mesenchymal transition and tumour metastasis through a TWIST1-G3BP2 mechanotransduction pathway,” *Nat. Cell Biol.*, vol. 17, no. 5, pp. 678–688, May 2015, doi: 10.1038/ncb3157.
- [55] M. K. Jena and J. Janjanam, “Role of extracellular matrix in breast cancer development: a brief update,” *F1000Research*, vol. 7, 2018, doi: 10.12688/F1000RESEARCH.14133.2.
- [56] C. Walker, E. Mojares, and A. Del Río Hernández, “Role of Extracellular Matrix in Development and Cancer Progression,” *Int. J. Mol. Sci.*, vol. 19, no. 10, 2018, doi: 10.3390/IJMS19103028.
- [57] S. Xu *et al.*, “The role of collagen in cancer: from bench to bedside,” *J. Transl. Med.* 2019 171, vol. 17, no. 1, pp. 1–22, Sep. 2019, doi: 10.1186/S12967-019-2058-1.
- [58] J. Winkler, A. Abisoye-Ogunniyan, K. J. Metcalf, and Z. Werb, “Concepts of extracellular matrix remodelling in tumour progression and metastasis,” *Nat. Commun.* 2020 111, vol. 11, no. 1, pp. 1–19, Oct. 2020, doi: 10.1038/s41467-020-18794-x.
- [59] T. Armstrong *et al.*, “Type I collagen promotes the malignant phenotype of pancreatic ductal adenocarcinoma,” *Clin. Cancer Res.*, vol. 10, no. 21, pp. 7427–7437, Nov. 2004, doi: 10.1158/1078-0432.CCR-03-0825.
- [60] O. Falou *et al.*, “Evaluation of neoadjuvant chemotherapy response in women with locally advanced breast cancer using ultrasound elastography,” *Transl. Oncol.*, vol. 6, no. 1, pp. 17–24, 2013, doi: 10.1593/tlo.12412.

- [61] S. R. Mousavi, H. Rivaz, A. Sadeghi-Naini, G. J. Czarnota, and A. Samani, “Breast Ultrasound Elastography Using Full Inversion-Based Elastic Modulus Reconstruction,” *IEEE Trans. Comput. Imaging*, vol. 3, no. 4, pp. 774–782, 2017, doi: 10.1109/tci.2017.2741422.
- [62] S. R. Mousavi, H. Rivaz, G. J. Czarnota, A. Samani, and A. Sadeghi-Naini, “Ultrasound Elastography of the Prostate Using an Unconstrained Modulus Reconstruction Technique: A Pilot Clinical Study,” *Transl. Oncol.*, vol. 10, no. 5, pp. 744–751, 2017, doi: 10.1016/j.tranon.2017.06.006.
- [63] H. Tadayyon *et al.*, “A priori prediction of breast tumour response to chemotherapy using quantitative ultrasound imaging and artificial neural networks,” *Oncotarget*, vol. 10, no. 39, pp. 3910–3923, 2019, doi: 10.18632/ONCOTARGET.26996.
- [64] H. Moghadas-Dastjerdi, H. R. Sha-E-Tallat, L. Sannachi, A. Sadeghi-Naini, and G. J. Czarnota, “A priori prediction of tumour response to neoadjuvant chemotherapy in breast cancer patients using quantitative CT and machine learning,” *Sci. Reports 2020 101*, vol. 10, no. 1, pp. 1–11, Jul. 2020, doi: 10.1038/s41598-020-67823-8.
- [65] H. Rivaz, E. M. Boctor, M. A. Choti, and G. D. Hager, “Real-time regularized ultrasound elastography,” *IEEE Trans. Med. Imaging*, vol. 30, no. 4, pp. 928–945, 2011, doi: 10.1109/TMI.2010.2091966.
- [66] H. S. Hashemi and H. Rivaz, “Global Time-Delay Estimation in Ultrasound Elastography,” *IEEE Trans. Ultrason. Ferroelectr. Freq. Control*, vol. 64, no. 10, pp. 1625–1636, 2017, doi: 10.1109/TUFFC.2017.2717933.
- [67] N. Kheirkhah, S. C. H. Dempsey, H. Rivaz, A. Samani, and A. Sadeghi-Naini, “A Tissue Mechanics Based Method to Improve Tissue Displacement Estimation in Ultrasound Elastography,” in *Proceedings of the Annual International Conference of the IEEE Engineering in Medicine and Biology Society, EMBS*, Jul. 2020, vol. 2020–July, pp. 2051–2054, doi: 10.1109/EMBC44109.2020.9175869.
- [68] N. Kheirkhah, A. Sadeghi-Naini, and A. Samani, “Analytical Estimation of Out-of-plane Strain in Ultrasound Elastography to Improve Axial and Lateral Displacement Fields,” in *Proceedings of the Annual International Conference of the IEEE Engineering in Medicine and Biology Society, EMBS*, Jul. 2020, vol. 2020–July, pp. 2055–2058, doi: 10.1109/EMBC44109.2020.9176086.
- [69] N. Kheirkhah, S. Dempsey, A. Sadeghi-Naini, and A. Samani, “A Novel Tissue Mechanics-based Method for Improved Ultrasound Motion Tracking in Ultrasound Elastography,” *Med. Phys.*, 2021.
- [70] T. L. Szabo, *Diagnostic Ultrasound Imaging: Inside Out: Second Edition*. Elsevier Inc., 2004.
- [71] S. C. H. Dempsey, J. J. O’Hagan, and A. Samani, “Measurement of the hyperelastic properties of 72 normal homogeneous and heterogeneous ex vivo breast tissue

- samples,” *J. Mech. Behav. Biomed. Mater.*, vol. 124, Dec. 2021, doi: 10.1016/J.JMBBM.2021.104794.
- [72] N. P. Pereira *et al.*, “Diffusion-Weighted Magnetic Resonance Imaging of Patients with Breast Cancer Following Neoadjuvant Chemotherapy Provides Early Prediction of Pathological Response – A Prospective Study,” *Sci. Rep.*, vol. 9, no. 1, pp. 1–8, Dec. 2019, doi: 10.1038/s41598-019-52785-3.
- [73] J.-H. Gu, C. He, Q.-Y. Zhao, and T.-A. Jiang, “Usefulness of new shear wave elastography in early predicting the efficacy of neoadjuvant chemotherapy for patients with breast cancer: where and when to measure is optimal?,” *Breast cancer*, 2022, doi: 10.1007/s12282-021-01327-9.

Chapter 4

4 Conclusions and Future Work

4.1 Conclusions

In this study, first, an enhanced ultrasound elastography technique was proposed and rigorously validated using *in silico* and tissue-mimicking phantom, and clinical studies. This technique utilizes two tissue mechanics-based principles of tissue incompressibility and strain compatibility. The more accurate displacement and strain fields can then be fed into any ultrasound elastography framework to estimate tissue mechanical properties. These techniques can be employed for early detection and identification of soft tissue cancer based on the notion that tissue mechanical properties change as a result of cancer. These tissue mechanical properties can provide useful information for cancer detection and assessing its progression while a more accurate estimate of these properties obtained through our enhanced technique can be used in conjunction with other clinical data and detection methods for example other medical imaging techniques, histopathology results, etc. to improve clinical outcome and results. Displacement fields obtained using the aforementioned displacement enhancement technique was used in an unconstrained inverse finite element framework to estimate tissue Young's modulus for LABC patients who were prescribed chemotherapy before a mastectomy. Using this method, the stiffness ratio of the patients' tumors was monitored throughout chemotherapy. The purpose of this study was to find a correlation between the change in the tumor's Young's modulus and patients' response to chemotherapy. These investigations were presented in two chapters of this dissertation. The primary research contributions and details of the results for each chapter are summarized below.

4.1.1 Chapter 2: A Novel Tissue Mechanics-based Method for Improving Tissue Displacement and Strain Estimation in Breast Ultrasound Elastography

In this chapter, a novel method for refining tissue displacement and strain fields generated in conventional quasi-static ultrasound imaging was presented. This method involves three

main steps of smoothing displacement field using second order derivative-based regularization, further refining them using tissue incompressibility equation, and finally, refining the acquired strain fields using strain compatibility equation. Additionally, a Boussinesq semi-infinite analytical model was used for estimating the out-of-plane strain which is needed for the tissue incompressibility equation. To our knowledge, this has never been done before in the literature. Validation of this method was done using a set of *in silico* and tissue-mimicking phantom, and clinical studies. All these studies showed that this method is capable of improving displacement and strain fields specially in the lateral direction. Based on these validations, the proposed method appears to be very effective in producing improved estimate of tissue displacement and strain images. Once again, compared to improvement of the axial displacement and strain components, the improvement is highly remarkable for the lateral component which had not yet been ameliorated in the literature.

4.1.2 Chapter 3: Enhanced Full-Inversion-Based Ultrasound Elastography for Evaluating Tumor Response to Neoadjuvant Chemotherapy in Patients with Locally Advanced Breast Cancer

In this chapter the application of a novel full inversion-based ultrasound elastography technique for monitoring tumor response to neoadjuvant chemotherapy (NAC) in locally advanced breast cancer (LABC) patients was investigated. The novelty of technique mostly relates to adapting the STREAL method, described in Chapter 2, for refining displacement and strain data before generating Young's modulus (E) images through an inverse finite element (FE) based reconstruction framework. These images were generated for 25 LABC patients who underwent full course of chemotherapy at weeks 1, 2, and 4 as well as before the start of treatment. The stiffness of tumor was then assessed and monitored based on these Young's modulus images and the boundaries of tumor which were determined by the B-mode images counterpart. Based on the response of each patient which had already been determined after completement of NAC and surgery using the standard clinical and histopathological criteria, a very good correlation between the change in tumor stiffness

and final response to NAC was observed. Specifically, statistical analysis confirmed that using the trend of change in tumor stiffness based on generated E images, the responder and non-responder patients could be differentiated as early as 1 week after the start of treatment. This is while such early differentiation could not be found through neither monitoring tumor diameter nor tumor stiffness based on strain images. In conclusion, this study demonstrated a very good potential for the proposed full inversion-based ultrasound elastography technique in assessing and predicting tumor response to NAC in LABC patients as early as one week after the NAC initiation. Early predication of NAC response for these patients potentially facilitates treatment adjustment by clinicians on an individual patient basis. A personalized paradigm for breast cancer therapeutics is anticipated to improve the overall therapy outcome, survival, and quality of life for the patients. This study, therefore, is a step forward towards precision oncology and tailoring chemotherapies for breast cancer patients.

4.2 Future Directions

While the proposed investigations demonstrated very promising results in assessing and validating the developed technique namely STREAL, further investigation with several clinical cases is necessary for more rigorous assessment of the method's performance in the clinic. Furthermore, there proposed methods involve some limitations which provide opportunities for further enhancement.

Using an analytical model based on Boussinesq semi-infinite equations for estimating out-of-plane strain is a novel and effective method for improving the accuracy of enforced incompressibility equation for refining axial and lateral displacement fields. However, this analytical model does not consider specific geometries of different breasts. An ongoing project in our research lab has been dedicated to address this issue with the aim of considering patient specific breast geometry.

STREAL method can be applied on any previously generated displacement field from quasi-static ultrasound elastography of soft tissues, including breast, prostate, and liver elastography. While we showed efficacy of this method in breast elastography application,

assessing its performance in elastography of other organs is encouraged. It is noteworthy that since this method is based on particular assumptions regarding the geometry and tissue mechanics, the applicability of these assumptions in the organ of interest should be examined first.

One other potential investigation on STREAL would be applying STREAL on less regularized displacement fields to assess the level of sensitivity of STREAL to its input. This investigation has already been started in our labs. The results have been promising so far, indicating that STREAL can improve even low-quality displacement fields.

In Chapter 2, two variants of E images based on different weights for two different equations derived from Hooke's law were generated and assessed for monitoring patients' response to NAC based on their tumors' stiffness. While the performance of both these variants were perceived to be similar, further investigation on the optimum weights for these variants is recommended. Moreover, studies involving larger patient populations are required to further evaluate the efficacy and robustness of the technique.

In quasi-static ultrasound elastography, the ultrasound RF data which are collected throughout the stimulation of tissue consist of several number of frames. The quality of displacement fields, strain images, and Young's modulus images depend highly on how the tissue is being deformed. An important aspect in generating an accurate elastogram is to find the best pair of RF frames that corresponds to a suitable tissue deformation. One major bottleneck of quasi-static ultrasound elastography is to find this optimum frame pair. In this work, this has been done through an ad-hoc procedure in which the fields were assessed visually by an expert researcher. As a future work, a systematic and automatic method potentially based on principles of tissue mechanics can be developed for efficiently finding the proper frame pairs for ultrasound elastography in any ultrasound RF data.

4.3 Closing Remarks

Ultrasound elastography has emerged to be a potential tool for tumor localization and classification, assessment of cancer progression, and diagnosis of cancer in soft tissues, including breast, prostate, and liver. While this technique is clinically acceptable,

inexpensive, and easily accessible throughout the world, it still can be considered to be nascent while it has a lot of potential for further improvement. Acquiring accurate displacement fields specially in lateral direction in quasi-static ultrasound elastography has always been a challenge. This challenge was exquisitely addressed in this research by incorporating tissue-mechanics based principles. As an application, developing such technique further has helped us to assess the potential of ultrasound elastography in evaluating breast cancer progression. Our developed technique and primary results show great potential in clinical settings. However, further clinical studies are required to assess the accuracy and reliability of the proposed technique.

Curriculum Vitae

Name: Niusha Kheirkhah

Post-secondary Western University

Education and London, Ontario, Canada

Degrees: 2018-2022 Ph.D., Biomedical Engineering

Sharif University of Technology

Tehran, Iran

2013-2018 B.Sc., Electrical Engineering

Related Work

Experience

Research Experiences

Graduate Research Assistant (GRA)

2018 - 2021

School of Biomedical Engineering, Western University,
London, Ontario, Canada

Teaching Experiences

Graduate Teaching Assistant (GTA)

Western University, London, Ontario, Canada

- Introduction to Electrical Engineering 2022,2020,2019
 - Human Biomechanics with Biomedical Applications 2021
 - Algorithms and Data Structures for Object-oriented Design 2020
 - Digital Logic Design 2018, 2019

Publications:

Journal Papers

- **N. Kheirkhah**, A. Sadeghi-Naini, and A. Samani, “A Novel Tissue Mechanics-based Method for Improved Ultrasound Motion Tracking in Ultrasound Elastography”, Journal of Medical Physics, *to be published*
- **N. Kheirkhah**, A. Kornecki, G. J. Czarnota, A. Samani, and A. Sadeghi-Naini, “Enhanced Full-Inversion-Based Ultrasound Elastography for Evaluating Tumor Response to Neoadjuvant Chemotherapy in Patients with Locally Advanced Breast Cancer”, *under review*

Conference Papers

- **N. Kheirkhah**, A. Sadeghi-Naini, and A. Samani, “Assessment of Locally Advanced Breast Cancer Response to Chemotherapy using Enhanced Ultrasound Elastography”, 19th Annual Imaging Network Ontario (IMNO) Symposium, Canada, Mar. 2021 (**Podium**)
- **N. Kheirkhah**, A. Sadeghi-Naini, and A. Samani, “Analytical Estimation of Out-of-plane Strain in Ultrasound Elastography to Improve Axial and Lateral Displacement Fields,” in Proceedings of the Annual International Conference of the IEEE Engineering in Medicine and Biology Society, EMBS, Jul. 2020 (**Podium**)
- **N. Kheirkhah**, S. C. H. Dempsey, H. Rivaz, A. Samani, and A. Sadeghi-Naini, “A Tissue Mechanics Based Method to Improve Tissue Displacement Estimation in Ultrasound Elastography,” in Proceedings of the Annual International Conference of the IEEE Engineering in Medicine and Biology Society, EMBS, Jul. 2020 (**Podium**)
- **N. Kheirkhah**, A. Sadeghi-Naini, and A. Samani, “A Novel Method to Improve Estimation of Tissue Displacement Field in Ultrasound Elastography”, The Canadian Society for Mechanical Engineering (CSME), London ON, Canada, Jun. 2019 (**Podium**)
- **N. Kheirkhah**, A. Sadeghi-Naini, and A. Samani, “A Novel Full-Inversion-Based Ultrasound Elastography Technique for Evaluating Breast Cancer Response to Chemotherapy”, London Health Research Day (LHRD), London ON, Canada, Apr. 2019 (**Poster**)